國 立 交 通 大 學

機械工程學系

碩 士 論 文

以微觀力學模式模擬複合材料
與應變率有關之非線性行為

Modeling Nonlinear Rate Dependent Behavior of Composites Using

Micromechanical Approach

研 究 生 ：陳奎翰

指導教授 ：蔡佳霖 博士

中 華 民 國 九 十 四 年 七 月

以微觀力學模式模擬複合材料與應變率有關之非線性行為

Modeling Nonlinear Rate Dependent Behavior of Composites Using

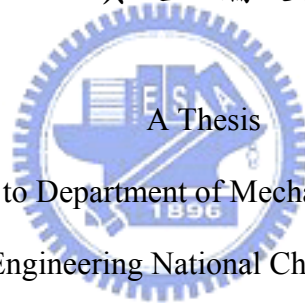Micromechanical Approach

研 究 生：陳奎翰　　　　　　　　　Student：Kuei-Han Chen

指導教授：蔡佳霖　　　　　　　　　Advisor：Jia-Lin Tsai

國 立 交 通 大 學

機 械 工 程 系

碩 士 論 文

A Thesis

Submitted to Department of Mechanical Engineering

College of Engineering National Chiao Tung University

in partial Fulfillment of the Requirements

for the Degree of

Master

in

Mechanical Engineering

July 2005

Hsinchu, Taiwan, Republic of China

中 華 民 國 九 十 四 年 七 月

以微觀力學模式模擬複合材料
與應變率有關之非線性行為

學生：陳奎翰　　　　　　　指導教授：蔡佳霖

國立交通大學機械工程學系碩士班

摘　要

本研究目的在於以微觀力學模式描繪碳纖/環氧樹脂複合材料與應變率有關之非線性行為。材料性質方面，將環氧樹脂假設為彈性黏塑性材料並以三參數黏塑性模式描述之，纖維則假設為橫向等向性材料。藉由環氧樹脂在 10^{-4}、10^{-2} 以及 $1/s$ 三種應變率之下的壓縮試驗，三參數模式所需的係數可藉由實驗獲得的應力應變曲線來定義。伴隨著已知的碳纖與環氧樹脂的材料性質，碳纖/環氧樹脂複合材料可藉由微觀力學模式進行模擬。在此研究中，有兩個微觀力學模式被採用，分別是 Square Fiber Model 以及 Generalized Method of Cells。此外，兩種纖維排列方式（Square Edge Packing 與 Square Diagonal Packing）與兩種纖維形狀（圓形與正方形）被一併考量並且與 ANSYS 所執行之有限元素法做一系列纖維排列與纖維形狀對材料性質影響性的比較與探討。數值結果指出纖維形狀對偏軸複合材料機械性質的影響並不明顯，然而，纖維的排列方式對此卻有顯著的影響性，而且 Square Edge Packing 相較於 Square Diagonal Packing 模擬出更硬的應力應變曲線。

為了驗證微觀力學模式的準確性，偏軸的碳纖/樹脂複材試片在 10^{-4} 到 550/s 的應變率之下做壓縮測試以獲得實驗值。由實驗值與模式預測的比較結果可知，數值預測結果雖然與實驗有一定程度的差異，但結合三參數黏塑性模式的微觀力學模式的確有能力描述與應變率有關的材料非線性行為。

Modeling Nonlinear Rate Dependent Behavior of Composites Using Micromechanical Approach

Student：Kuei-Han Chen   Advisor：Dr. Jia-Lin Tsai

Institute of Mechanical Engineering

National Chiao Tung University

Abstract

This research aims to characterize the nonlinear rate dependent behavior of graphite/epoxy composites using a micromechanical approach. For epoxy phase, it was assumed to be following the elastic/viscoplastic behavior described by a three parameterts viscoplasticity model; while the graphite fiber was assumed to be a transverse isotropic solid. By performing compression tests on the epoxy resin at three different strain rates of 10^{-4}, 10^{-2} and 1/s, the stress and strain relation of the epoxy resin was generated. Based on the experimental data, the three parameter viscoplasticity model was developed. With the ingredient properties, the mechanical behaviors of graphite/epoxy composites were characterized using the micromechanical approach.   There are two micromechanical models, i.e. Generalized Method of Cell (GMC) and Square Fiber Model (SFM), were employed in this study.   In addition, two different fiber arrangements, i.e., square edge packing and square

diagonal packing as well as the fiber shapes, i.e. square type and round type, were taken into account. The finite element analysis with commercial code ANSYS was also adopted to investigate the fiber arrangement effect and the fiber shape effect. It was indicated basically, the mechanical behaviors were not affected appreciably by the fiber shape. On the contrary, the fiber arrangements play an essential role on the mechanical behaviors. The square edge packing demonstrates stiffer behaviors than the square diagonal packing. In order to verify the model predictions, off-axis graphite/epoxy composite specimens were tested at strain rate ranges from 10^{-4}/s to 550/s. Comparison of model predictions obtained from GMC and SFM analysis with the experimental results revealed that the micromechanical approaches are capable of predicting the nonlinear rate sensitivity of off-axis specimens although there are still distinctions between the model and the experimental results.

誌謝

　　此文，謹獻給伴我走過碩士生涯的師長、同學、朋友們。

　　兩年前，我帶著無知與懵懂進入交通大學機械系碩士班追隨蔡佳霖博士從事複合材料研究，從一名專業知識停留在大學程度的毛頭小子，藉由研究所課程的訓練與洗禮，逐漸培養出正確積極的研究態度與充足的專業知識，進而蛻變為具獨當一面處理、解決問題能力的碩士生。這段改變歷程固然艱苦，但品嚐到豐收果實的霎時間，一切辛苦都是值得的，畢竟，要怎麼收穫，先那麼栽。

　　在此，我誠摯地向兩年來在各方面支持我的人們致上由衷的感謝。感謝指導教授蔡佳霖老師，俗話說「一日為師終身為父」，謝謝老師您兩年來的指導，無私地傳授我們研究的方法與專業知識，讓我對複合材料有深層且深刻的認識，生活上也蒙您照顧，使實驗室雖經風浪也能一路安穩度過。老師，謝謝您。

　　感謝使我衣食無缺無後顧之憂的父母，你們不肖的兒子離家求學九年，未曾替家盡過一份心力，願我入伍服役後學會成熟、負責以及爸爸您希望我體悟的服從，早日替家庭負擔生計。感謝前女友筱婷，雖然離別使我的生活頓失重心與依靠，但這段日子，我熬過來了，相信在遠方的妳也默默地為我祝福並希望我也同妳一般過得好。感謝馥，陪伴我最後三個月的研究所生涯，每逢週末的郊遊踏青、小酌閒談，是研究所後期最快樂的時光。

　　感謝兩位已畢業的學長漢偉與仁傑，將剛進實驗室的我帶上軌道，去年你們畢業時，我擔心自己的能力不足以接掌實驗室負責人以及引領學弟們，一年後，雖不臻完美卻也中規中矩。感謝同學濬清在畢業前夕苦熬著偏軸複材的壓縮試驗，提供一組近乎完美的實驗數據給我的微觀力學模型使用，沒有你的實驗配合，這本論文無法稱為完整。感謝同學世民給我不少試片製作上的觀念與技術，尤其在樹脂除氣與模具的使用上，提供了莫大的協助。感謝學弟明道與世華，在我研究苦悶之際給予精神上的支持與提供排憂解愁的管道。

　　最後，特別感謝明安國際朱國棟博士、清華大學葉孟考教授與中正大學黃崧任博士於百忙中抽空擔任學位論文口試委員並給予論文內容甚多建議，使此論文更趨完善與正確。此外，感謝工研院材料所的盧廷鉅學長與德霖技術學院邱進東博士分別教導我ABAQUS 與 MARC 的基礎操作，雖然這兩套軟體最後沒為我的論文所採用，但能順利得到有限元素法的分析成果，二位功不可沒。

　　欲感謝之人眾多，恐有疏漏，在此致上歉意並於文末一道感謝，感謝一路陪我走來的眾人，謝謝你們。

陳奎翰 2005.07.19 於交通大學

<div align="center">目　　錄</div>

LIST OF TABLES

LIST OF FIGURES

Chapter 1   Introduction

1.1 Research Motive

Composite materials, because of their high strength/weight ratio, have been extensively used not only in aerospace industry but also in marine and automotive industries.   In some of the applications, high strain rate loading may be produced, such as blast loading of a submarine hull and bird strike of an aircraft structure. Thus characterizing and modeling the high strain rate responses of composite materials is becoming an essential task for further applications.   It is well known that the polymeric materials exhibit nonlinear rate dependent behavior, which implies that the polymeric composite will somehow exhibit the rate sensitivity if the associated behavior is dominated by the matrix.   In past decades, the nonlinear rate dependent behavior of composites have been studied by many researchers who treated the unidirectional composites as orthotropic homogeneous solids.   This is so called macro-mechanical analysis.   However, in this macro-mechanical approach, the mechanism of how the fiber and the matrix material affect the overall composite nonlinearity can not be fully characterized.   Therefore, a research from the micromechanical viewpoint was proposed and used to investigate this phenomenon. In the micromechanical approach, the fiber arrangement, the fiber shape, fiber properties and matrix properties were taken into account and the effect of the ingredients on the rate sensitivity of the composites were further examined.

1.2 Paper Review

Unidirectional fiber composite materials exhibit nonlinear rate dependent behavior under off-axis loading.   There are two points of view to discuss this physical phenomenon, i.e. macromechanical and micromechanical mechanics, and all published literatures originated from either of the two perspectives.   Based on the

viewpoint of macromechanics, Sun and Chen [1] developed a single parameter yield function under plane stress assumption and brought it into the flow rule with a power law curve fitting effective stress – effective plastic strain relation to describe the nonlinearity of fiber composites. This single parameter in the yield function was chosen suitably so that all off-axis experimental data collapse into a single master curve in the effective stress versus effective plastic strain domain. It is a fact that the single parameter model has good agreements with experiments. Because of rate independence in this model, some improvements were carried out. Gates and Sun [2] combined the over stress model [3] with the single parameter model to predict the rate dependent behavior of composites under loading (the over stress is positive) and unloading (the over stress is zero) conditions. In order to use the over stress model, a quasistatic stress - strain relation was set as a reference state, and when the strain rate is higher, the corresponding relative effective stress was calculated by subtracting the quasistatic effective stress from the current effective stress associated with the same strain level. The relative effective stress and effective plastic strain rate relations obtained from the over stress model were then employed together with the flow rule for characterizing the plastic deformation of composites subjected off-axis loading. Yoon and Sun [4] used the same way as Gates and Sun [2] to investigate the effects of variant strain rates on a monotonic tension process under off-axis loading. The results were also compared with a modified Bodner and Partom's model [5]. Weeks and Sun [6] modeled off-axis composites using a mathematical form similar to Johnson-Cook model [7] in conjunction with the single parameter model. A quasistatic state was chosen as a reference state to get the corresponding reference effective plastic strain rate and effective stress while the Johnson-Cook model was working. Then, the effective stress and effective plastic strain rate relation at high strain rate analyses could be obtained via this model and applied into

flow rule to get corresponding plastic responses like the over stress model. Thiruppukuzhi and Sun [8] directly introduced a rate dependent term into the effective stress − effective plastic strain power law relation and proposed a three parameters model for modeling the nonlinear rate dependent behavior of unidirectional fiber composites. Since the power law equation is a convenient form to use, in this study, the three parameters model was adopted as the viscoplasticity model to describe the rate dependent nonlinearity of the matrix phase.

In order to investigate the nonlinear effect of matrix on the mechanical behavior of fiber composites, a micromechanical approach is proposed by modeling the composites as heterogeneous solids consisting of fiber and matrix phases. Through the characteristics of repetition, a Representative Volume Element (RVE) was selected to represent the whole composite materials. By analyzing the mechanical behavior of the RVE, the overall material responses of composites could be determined. There are several micromechanical models available for describing the mechanical behaviors of composites, i.e., Eshelby model [9], Mori-Tanaka model [10,11], square fiber model [12] and generalized method of cells [13-15]. Eshelby [9] introduced Eshelby's tensor together with the equivalent principal concept to model a homogeneous inclusion embedded in an infinite matrix. Basically, Eshelby model is a dilute model because only one inclusion is considered. Mori and Tanaka [10] extended Eshelby's approach to establish a non-dilute model in which the stress and strain states of the inclusion and the matrix were considered in an average sense. Benveniste [11] gave alternative explanations of Eshelby model and Mori-Tanaka model by introducing the strain concentration concept and obtained succinct formulas for these two models. Commonly, the Eshelby model and Mori-Tanaka model were mainly applied to characterize the stiffness of short fiber composites. However, they could be extended to characterize the long fiber composites if the aspect ratio of the

3

inclusion was assumed to be infinity [16] and the nonlinear behavior of composites can be described if an incremental Mori-Tanaka mean field approach was adopted [17]. Sun and Chen [12] proposed a "Square Fiber Model" constructed by a RVE composed of one square fiber and two pure matrix regions. A 2-D plane stress plastic potential modified from von Mises J_2 function was applied in conjunction with the associated flow rule to describe the plastic strain of the matrix material, while the fiber was regarded as an orthotropic elastic material. The entire stiffness matrix of the composite was derived from some suitable constant stress and constant strain assumptions between each subcell in the RVE. Therefore, we can obtain the total strain increments due to a given stress history by using this model. Similar to this way, Goldberg and Stouffer [18] suggested a four regions model with one square fiber and three matrix regions. Not a plane stress condition but both two transverse directions have to be applied constant stress and strain assumptions in all subregions to obtain the overall constitutive equation. The matrix phase was described using the Bodner and Partom's model [5] and the corresponding deformation was solved by using the Runge-Kutta method. Away from the forgoing theories, Aboudi [13, 14] derived a four regions micro-mechanical model called "Method of Cells", which is very efficient in modeling the elastic and inelastic behavior of fiber-reinforced unidirectional composites. Based on the displacement and traction continuity at the interfaces of all subcells as well as the periodicity at the RVE, a stress - strain relation was described in a matrix form to predict mechanical behavior of composite materials. By extending the method of cells, Paley and Aboudi [15] proposed a scheme called Generalized Method of Cells (GMC) which can deal with an undetermined numbers of subcells. The weak point in GMC is that the more subcells you have, the more CPU time is required. To enhance computational efficiency of GMC, Orozco [19] took advantage of the sparse features of the strain concentration matrix. It is

basically an improvement in the numerical processing. The sparse implementation of GMC made it possible to solve the problems with complex micro-structures and tiny refinements. Pindera and Bednarcyk [20] adopted a different manner to enhance the computational efficiency of GMC. They expressed the displacement continuity between the subcells in terms of stresses and then derived a modified formulation of GMC. This formulation is regarded as the most efficient way in the employment of GMC until now. The feature of the GMC is that which cells were fibers or matrices were not indicated in advance. In other words, we can assign the cells with either fibers or matrix after forward when the final constitutive equation was established. In applications of the GMC, Orozco and Pindera [21] combined the GMC with an available tangent plasticity matrix to analyze transverse mechanical behavior of composites under different fiber arrangements and fiber shapes. A large number of subcells were constructed in their study to model the complex microstructures. It showed that different fiber arrangements and fiber shapes lead to distinct constitutive behavior. Ogihara et al. [22] characterized the nonlinear behavior of carbon/epoxy unidirectional and angle-ply laminates. The GMC was applied first to obtain the property of unidirectional fiber composites under off-axis loading. Together with the laminate plate theory, the angle-ply laminates were calculated from the unidirectional composites. Kawai et al. [23] investigated the AS4/PEEK composites under loading and unloading conditions on the off-axis response at strain rate up to 0.01/min. The PEEK matrix was described by Chaboche model and the composite was predicted using GMC. The results showed good agreements with the experimental results for AS4/PEEK composites. However, the strain rates in their investigation were not high enough for engineering applications. Using finite element analysis, Zhu and Sun [24] investigated the nonlinear behaviors of fiber composites by applying suitable boundary conditions on a RVE selected properly with three different fiber

5

arrangements.   It was shown that the square diagonal packing array provides the best prediction on the experimental results for all samples with various off-axis angles

1.3 Research Approach

In view of the forgoing, most of efforts were made on the nonlinear behaviors of fiber composites.   While very few studies concerning the rate effect on the constitutive behaviors were reported.   Therefore, this research aims to characterize the nonlinear rate dependent behavior of graphite/epoxy composites.   More emphases will be placed on the combination effect of microstructure and strain rate. As a result, a micromechanical model consisting of fiber and matrix phases together with their respective constitutive relations will be employed for this analysis.   It is noted that the fiber phase was assumed as transverse isotropic elastic materials.   For matrix phase, the cylindrical specimens were tested in compression on a MTS system to characterize its rate dependent behavior.   Based on the experimental results, the three parameters model [8] was employed to describe the rate sensitivity of the matrix material.   With the matrix and fiber constitutive curves, the micromechanical models will be implemented for modeling the nonlinearity of the fiber composites.   It is noted that there were two different micromechanical models utilized in this analysis, i.e. Square Fiber Model (SFM) [12] and Generalized Method of Cells (GMC) [15]. The effect of the fiber arrangements and fiber shapes will be taken into account in the micromechanical modeling together with the finite element method (FEM) and the results will be compared to one another.   In addition, the effect of thermal residual stresses are also involved in the analysis.   Finally, the square fiber embedded in the RVE with square edge packing array was performed using SFM and GMC and has a comparison to the experimental results obtained by testing off-axis graphite/epoxy composites at strain rates from 10^{-4}/s to 550/s.

6

Chapter 2   Polymer Modeling

Since material properties of the polymer, i.e. Young's Modules, Poisson's ratio, and viscoplastic behavior, are required for modeling the behaviors of composites, tensile and compression tests were performed to determine the corresponding properties. The tensile test was performed to determine the Poisson's ratio of the polymer while the compression test was employed to determine the Young's modulus and the viscoplastic behavior of the polymer. Based on the experimental data of compression test at 10^{-4}, 10^{-2}, 1/s strain rates, the model coefficients of three parameters model [8] were determined and this model was applied to predict the Split Hopkinson Pressure Bar (SHPB) results up to 650/s strain rate. Besides, the coefficient of thermal expansion (CTE) of the polymer was measured to investigate the thermal stress effects on the off-axis composites.

2.1 Experiments

2.1.1 Compression Test

The polymer (Bisphenol A) in the form of powder provided from Ad-group Taiwan was filled into a pre-designed stainless mold for fabricating the cylindrical specimens. In the beginning, the mold was putted into a vacuum oven and heated from room temperature to $75\,^\circ$C within 50 minutes. During this process, the polymer was changed from powder state to liquid state with very high viscosity and its volume decreased due to gas disappearance, then, some powder was replenished until the desired amount of polymer was reached. In the next 8 minutes, the temperature was raised to $95\,^\circ$C and then kept for 130 minutes. At the same time, the polymer was also degassing in the vacuum oven. After degassing for a period of time, the polymer was overflowed on the mold easily and we should open the door of the vacuum oven and scrape the polymer to retreat to cavities by using a thin plate.

It was to be noted that this scraping process must be finished as soon as possible (within 5 minutes) to avoid a large drop of oven temperature. After repeating the degassing and scraping process 6 times within the 130 minute, the temperature was held on 90°C for 30 minutes to perform the curing process and raised to 145°C within 10 minutes and maintained 60 minutes to carry out the post curing process. After the curing and post-curing processes, the specimens were removed from the mold with care. In order to have parallel and smooth loading surfaces, all specimens were polished using a polishing machine with 25.0μ aluminum oxide powers. After polishing, the final dimensions for the specimens are 10 mm in height and 12mm in diameter as shown in Fig. 2.1(a). To demonstrate the strain rate effect on the polymer, compression tests were performed on the cylindrical specimens using hydraulic MTS machine at three different strain rates, 10^{-4}, 10^{-2} and 1/s. Back to back strain gages were adhered on the specimens for the strain measurement during compression tests. Fig. 2.2 demonstrates the experimental setup for the compression tests. The stress history was obtained from the load cell and the associated strain history was measured from the strain gages mounted on the specimens. During the tests, both stress and strain signals were recorded by LabView together with PC computer. All results of compression test were shown in Fig. 2.3 and the Young's modulus of the polymer was determined as 3.4 GPa.

2.1.2 Tensile Test

For measuring the Poisson's ratio of the polymer, tensile tests were carried out on the coupon specimens, with the dimensions as shown in Fig. 2.1(b), fabricated in the same manner as described early excepted that the designed mode is different. Two strain gages were mounted on the centers of the specimens. One was in the axial direction and the other was in the lateral direction to measure the axial and

transverse strains, respectively. The tensile test was implemented on a hydraulic MTS system at 10^{-4}/s strain rate and the result was shown in Fig. 2.4. According to this result, the Poisson's ratio of the polymer was evaluated as 0.37.

2.1.3 Measurement of Coefficient of Thermal Expansion

In the analysis of thermal residual stress effect, the coefficient of thermal expansion (CTE) of the matrix was measured first. A simple method [25-27] has been applied to finish this measurement in which the EA-06-062TT-120 strain gage was chosen and the adhesive M-bond 610 was used for its high operation temperature. The EA-06-062TT-120 strain gage has two pieces of electrical resistance on a unit, one is an axial field and the other is transverse. Therefore, axial and transverse deformations of a specimen can be measured at the same time. Based on the strain gage technique, when the gage was subjected to a biaxial strain field, as shown in Fig. 2.5, the following relation was found

$$\frac{\Delta R}{R} = F_a \varepsilon_a + F_t \varepsilon_t \qquad (2.1.1)$$

where

R = original gage resistance

F_a = axial gage factor

F_t = transverse gage factor

ε_a = axial strain field

ε_t = transverse strain field

Define the transverse sensitivity coefficient K as

$$K = \frac{F_t}{F_a} \qquad (2.1.2)$$

If the strain gage was mounted on a specimen with Poisson's ratio ν_0 and the specimen was under a uniaxial loading, the strain fields can be represented as

9

$$\varepsilon_t = -\nu_0 \varepsilon_a \tag{2.1.3}$$

Substituting eqns (2.1.2) and (2.1.3) into eqn (2.1.1) yields

$$\frac{\Delta R}{R} = F_a(1 - \nu_0 K)\varepsilon_a = F_g \varepsilon_a \tag{2.1.4}$$

where $F_g = F_a(1 - \nu_0 K)$ is the well-known gage factor and the measured strain can

be represented as

$$\varepsilon_a = \frac{\Delta R/R}{F_g} \tag{2.1.5}$$

Since eqn (2.1.4) can be applied only if the specimen was subjected to a

uniaxial stress field and the transverse strain field was due to the Poisson's ratio effect

only, on the measurement of CTE, the matrix under thermal expansion was within a

biaxial strain field and eqn (2.1.4) can not be followed directly.   Therefore, the

transverse sensitivity must be embraced to correct the gage results.   With the

assistance of measured strains at the axial and transverse direction, ε_{mx} and ε_{my},

the corrected strains ε_x and ε_y are given by [25]

$$\varepsilon_x = \frac{(1 - \nu_0 K)(\varepsilon_{mx} - K\varepsilon_{my})}{1 - K^2} \tag{2.1.6}$$

$$\varepsilon_y = \frac{(1 - \nu_0 K)(\varepsilon_{my} - K\varepsilon_{mx})}{1 - K^2} \tag{2.1.7}$$

It can be shown that in the current analysis, the strain of isotropic test material

with Poisson's ratio equal to 0.37 under the same measured strain $\varepsilon_{mx} = \varepsilon_{my}$ will be

about 2 % error if the correction equations (2.1.6) and (2.1.7) are not applied.   It's a

slight effect so the correction hasn't been done here.

It was noted that when the gage was mounted on a stress free specimen and

underwent temperature change, we can not say the gage signal was fully induced by

the specimen deformation but also affected by the thermal effect.   To cancel the

thermal effect on the electrical resistance, a half-bridge circuit as shown in Fig. 2.6

was applied [26].   There are two materials in the system, one is the test material and the other is the reference material.   The CTE of the test material is unknown but known for the reference material.   Since

$$\alpha_x - \alpha_r = \frac{\varepsilon_x - \varepsilon_r}{\Delta T} \qquad (2.1.8)$$

and

$$\Delta E = V \frac{R_1 R_2}{(R_1 + R_2)^2} \left(\frac{\Delta R_1}{R_1} - \frac{\Delta R_2}{R_2} + \frac{\Delta R_3}{R_3} - \frac{\Delta R_4}{R_4} \right) \qquad (2.1.9)$$

where α_x is the CTE of the test material at measured direction, α_r is the CTE of the reference material, ε_x is the thermal strain from the test material and ε_r is the thermal strain from the reference material.   By means of eqns (2.1.8) and (2.1.9), the thermal effect on the electrical resistance can be eliminated skillfully and the CTE of the test material can be determined.

The experimental system was placed in a programmable-control vacuum oven where the test material is a $30 \times 20 \times 2$ mm^3 thin plate and the reference material is a titanium silicate material with very small CTE (here we assume it is equal to zero). A thermal couple was adhered on the reference material to record the history of temperature change but not on the test material due to the limitation of specimen size. Because of low heating and cooling rate (about 19 ^{0}C/hr and 22 ^{0}C/hr, respectively), it can be assumed that the test and reference material possess the same temperature during heating and cooling processes so the temperature signal of the reference material can present the temperature of the test material, too.   According to the final result shown in Fig. 2.7, the CTE of the matrix is about $5.9 \times 10^{-5}/^\circ$C from the average of heating and cooling slopes.

2.2 Visco-Plasticity Model

A viscoplasticity model can be derived based on the low strain rate compression tests to describe the nonlinear rate dependent behavior of the epoxy materials. The epoxy material was treated as an isotropic von Mises plastic material and the J_2 plastic potential

$$J_2 = \frac{1}{6}\left[(\sigma_{11} - \sigma_{22})^2 + (\sigma_{22} - \sigma_{33})^2 + (\sigma_{33} - \sigma_{11})^2\right] + \sigma_{12}^2 + \sigma_{23}^2 + \sigma_{13}^2 \qquad (2.2.1)$$

was employed to develop the viscoplasticity model. By using the associated flow rule, the plastic strain rate is expressed as

$$\dot{\varepsilon}_{ij}^{p} = \dot{\lambda}\frac{\partial J_2}{\partial \sigma_{ij}} \qquad (2.2.2)$$

where $\dot{\lambda}$ is a proportional factor.

Defining an effective stress $\overline{\sigma}$ as

$$\overline{\sigma} = \sqrt{3J_2} \qquad (2.2.3)$$

through the plastic work rate relation, i.e.

$$\dot{W}^{p} = \sigma_{ij}\dot{\varepsilon}_{ij}^{p} = \overline{\sigma}\dot{\overline{\varepsilon}}^{p} = 2J_2\dot{\lambda} \qquad (2.2.4)$$

the effective plastic strain rate $\dot{\overline{\varepsilon}}^{p}$ can be expressed explicitly as

$$\dot{\overline{\varepsilon}}^{p} = \frac{2}{3}\left\{\frac{1}{2}\left[\left(\dot{\varepsilon}_{11}^{p} - \dot{\varepsilon}_{22}^{p}\right)^2 + \left(\dot{\varepsilon}_{22}^{p} - \dot{\varepsilon}_{33}^{p}\right)^2 + \left(\dot{\varepsilon}_{33}^{p} - \dot{\varepsilon}_{11}^{p}\right)^2\right] + \frac{3}{4}\left(\dot{\gamma}_{12}^{p}{}^2 + \dot{\gamma}_{23}^{p}{}^2 + \dot{\gamma}_{13}^{p}{}^2\right)\right\}^{1/2} \qquad (2.2.5)$$

and the proportional factor $\dot{\lambda}$ in eqn (2.2.2) was derived as

12

$$\dot{\lambda} = \frac{3}{2} \frac{\bar{\dot{\varepsilon}}^p}{\bar{\sigma}} = \frac{3}{2} \frac{\dot{\bar{\sigma}}}{H_p \bar{\sigma}} \qquad (2.2.6)$$

where H_p

$$H_p = \frac{\dot{\bar{\sigma}}}{\bar{\dot{\varepsilon}}^p} \qquad (2.2.7)$$

is the rate dependent plastic modulus.

It is noted that for the J_2 material subjected to uniaxial loading, the effective stress is equal to the axial stress and the effective plastic strain is the same as the axial plastic strain ε_x^p obtained by subtracting the elastic part from the total measured strain ε_x. As a result, the effective stress and effective plastic strain curves of the epoxy can be obtained directly from the experimentally determined axial stress and axial plastic strain curves. Fig. 2.8 shows the effective stress and effective plastic strain curves measured at strain rates of 10^{-4}, 10^{-2} and $1/s$.

Let the effective stress – effective plastic strain curves could be fitted individually by a power law as

$$\bar{\varepsilon}^p = A(\bar{\sigma})^n \qquad (2.2.8)$$

and the results were also illustrated in Fig. 2.8. It was found that the power index n in eqn (2.2.8) is constant for all strain rates. However, the amplitude A is a function of strain rate. Again, assume that the amplitude A is a power law function of effective plastic strain rate as [8]

$$A = \chi \left(\bar{\dot{\varepsilon}}^p \right)^m \qquad (2.2.9)$$

Then a viscoplasticity model can be expressed in the form

$$\bar{\varepsilon}^p = \chi \left(\bar{\dot{\varepsilon}}^p \right)^m (\bar{\sigma})^n \qquad (2.2.10)$$

It is noted that the effective stress and effective plastic strain curves plotted in Fig. 2.8 were produced for respective constant strain rates but not for constant effective plastic strain rates as required in the viscoplasticity model. By subtracting the elastic component from the total strain, the plastic strain component, and thus the effective plastic strain, can be obtained. Fig. 2.9 shows the effective plastic strain-time curves for epoxy specimens corresponding to strain rate of 10^{-4}/s. It is evident from Fig. 2.9 that the effective plastic strain rate is not constant over the entire loading range. Nevertheless, it almost reaches a constant value beyond $\bar{\varepsilon}^p = 0.25\%$. Since the initial deformation of the stress-strain curve is mainly dominated by the elastic response, in determining parameters χ and m in eqn (2.2.9), the data corresponding to the initial portion for which the effective plastic strain is less than 0.25% was truncated. Fig. 2.10 shows amplitude A as a function of effective plastic strain rate on the log-log scale for the epoxy material obtained from the compression tests. The parameters χ and m are then determined from these plots as the intercept and the slope, respectively. Once m and χ are determined, this model can be extrapolated to predict the material behavior at any strain rates. The values of the parameters in the viscoplasticity model for epoxy are listed in Table 1.

With eqn (2.2.10), the rate dependent plastic modulus is expressed as

$$H_p = \frac{1}{n\chi(\dot{\bar{\varepsilon}}^p)^m(\bar{\sigma})^{n-1}} \tag{2.2.11}$$

According to the definition of the effective stress given in eqn (2.2.3), $\dot{\bar{\sigma}}$ was derived as

$$\dot{\bar{\sigma}} = \frac{1}{2\bar{\sigma}}(2\sigma_{11} - \sigma_{22} - \sigma_{33})\dot{\sigma}_{11} + (-\sigma_{11} + 2\sigma_{22} - \sigma_{33})\dot{\sigma}_{22} + (-\sigma_{11} - \sigma_{22} + 2\sigma_{33})\dot{\sigma}_{33}$$
$$+ 6\sigma_{23}\dot{\sigma}_{23} + 6\sigma_{13}\dot{\sigma}_{13} + 6\sigma_{12}\dot{\sigma}_{12} \tag{2.2.12}$$

By substituting eqn (2.2.12) together with eqn (2.2.6) into eqn (2.2.2), the plastic strain rate is written as

$$
\begin{Bmatrix} \dot{\varepsilon}_{11}^p \\ \dot{\varepsilon}_{22}^p \\ \dot{\varepsilon}_{33}^p \\ \dot{\gamma}_{23}^p \\ \dot{\gamma}_{13}^p \\ \dot{\gamma}_{12}^p \end{Bmatrix} = \frac{9}{4} \frac{1}{H_p \bar{\sigma}^2} \begin{bmatrix} S_1^2 & S_1 S_2 & S_1 S_3 & S_1 S_4 & S_1 S_5 & S_1 S_6 \\ & S_2^2 & S_2 S_3 & S_2 S_4 & S_2 S_5 & S_2 S_6 \\ & & S_3^2 & S_3 S_4 & S_3 S_5 & S_3 S_6 \\ & \text{symmetric} & & S_4^2 & S_4 S_5 & S_4 S_6 \\ & & & & S_5^2 & S_5 S_6 \\ & & & & & S_6^2 \end{bmatrix} \begin{Bmatrix} \dot{\sigma}_{11} \\ \dot{\sigma}_{22} \\ \dot{\sigma}_{33} \\ \dot{\sigma}_{23} \\ \dot{\sigma}_{13} \\ \dot{\sigma}_{12} \end{Bmatrix} \quad (2.2.13)
$$

where

$$
\begin{aligned}
S_1 &= \frac{1}{3} \left(2\sigma_{11} - \sigma_{22} - \sigma_{33} \right) \\
S_2 &= \frac{1}{3} \left(-\sigma_{11} + 2\sigma_{22} - \sigma_{33} \right) \\
S_3 &= \frac{1}{3} \left(-\sigma_{11} - \sigma_{22} + 2\sigma_{33} \right) \\
S_4 &= 2\sigma_{23} \\
S_5 &= 2\sigma_{13} \\
S_6 &= 2\sigma_{12}
\end{aligned} \quad (2.2.14)
$$

In combination of the elastic parts, the constitutive relation of epoxy material at various strain rates was established as

$$
\{ \dot{\varepsilon} \} = \left[S^M \right] \{ \dot{\sigma} \} \quad (2.2.15)
$$

where

$$
\left[S^M \right] = \left[S^e \right] + \left[S^p \right] \quad (2.2.16)
$$

In eqn (2.2.16), $\left[S^e \right]$ represents the elastic compliance matrix of the epoxy and $\left[S^p \right]$ denotes the plastic compliance matrix given in eqn (2.2.13). It is to be noted that with eqn (2.2.15), the epoxy material properties at different loading rates could be characterized from which, through a micromechanical analysis, the mechanical behaviors of polymeric composites could also be generated. Inverting eqn (2.2.15), we derived

15

$$\{ \dot{\sigma} \} = \left[C^M \right] \{ \dot{\varepsilon} \} \qquad (2.2.17)$$

where

$$\left[C^M \right] = \left[S^M \right]^{-1} \qquad (2.2.18)$$

The constitutive relation expressed in the form of eqn (2.2.17) was used in chapter 4 as the matrix material properties for the generalized method of cells micromechanical model.

2.3 Modeling of Split Hopkinson Pressure Bar Results

The stress and strain relations of polymer (Bisphenol A) under high strain rate were found using the steel SHPB apparatus. The gas pressure of 100 psi was used to push the steel striker bar and the compression wave was generated in the steel incident bar with 3 mm thickness copper pulse shaper attached on the impact surface. The compression wave signals were obtained by a pair of diametrically opposite gages mounted on the middle of the incident bar and the transmission bar. The amplification factors of incident bar channel and transmission bar channel were both set at 400. The excitation voltages of the Wheatstone bridge circuits were set at 5V. However, the amplification factor of specimen gage signal was set at 25 and excitation voltage was set at 3V. The sampling rate of oscilloscope was set at 10 MHz to record the voltage signals from Wheatstone bridge circuits and the final stress - strain curve of the polymer was shown in Fig. 2.11 where the Young's modulus was determined as 3.9 GPa. With the assistance of given stress history from experiments as shown in Fig. 2.12, the associated plastic strain rates can be estimated by eqn (2.2.13) in which the effective stress was evaluated using eqn (2.2.3) and the effective

plastic strain rate embedded in the plastic modulus H_p was determined through eqn

(2.2.5).　Then, the total strain was constructed through the combination of elastic

strains and plastic strains.　The prediction result was plotted together with MTS

results and shown in Fig. 2.13.　Since the Young's modulus of the polymer up to

650/s strain rate attains to 3.9 GPa greater than the MTS result 3.4 GPa, the polymer

somehow exists viscoelastic behavior but wasn't considered in the three parameters

model.　Therefore, there is a significant distinction between the prediction and

experimental results due to the effect of different elastic strain.

Chapter 3   Square Fiber Model

In this chapter, the square fiber model (SFM) proposed by Sun and Chen [12] for modeling the composite nonlinearity was reviewed.   Since the typical square fiber model was constructed based on the square edge packing array as shown in Fig. 3.1(a), it can not be applied to other fiber arrangements, like the square diagonal packing array demonstrated in Fig. 3.1(b).   As a result, a modified SFM was developed to account for the RVE with various fiber arrangements.   In addition, the thermal stress effect was considered using SFM and will be discussed in chapter 6.

3.1 Square Fiber Model

Sun and Chen [12] proposed a representative volume element (RVE) as shown in Fig. 3.2 for unidirectional composites.   This RVE is so-called square edge packing array (SEP) as shown in Fig. 3.1(a).   In this RVE, the round fiber is approximated by a square one with a cross-section area equal to that of the circular one.   It is noted that because of geometric symmetry, only a quarter of the RVE is considered.   This RVE is composed of three subregions, AF, AM and B, in which AF stands for the fiber; AM and B stand for the matrix.   Subregions AF and AM were assembled into Region A.   The fiber subregion AF is considered to be a square cross-section with the same cross section area of the original quarter circle.   The coordinate system is set up such that the fiber direction is parallel to the x_1 axis.   A plane stress assumption prevails in the $x_1 - x_2$ plane such that the out of plane stress components would vanish ($\sigma_{13} = \sigma_{23} = \sigma_{33} = 0$).   In addition, the follow assumptions are also made.

(a) The stress and strain states are uniform in all subregions.

(b) In region A, the stress and strain fields in AF and AM follow suitable constant stress or constant strain assumptions, i.e.

$$\sigma_{12}^{AF} = \sigma_{12}^{AM} = \sigma_{12}^{A} \quad \text{(constant stress)}$$
$$\sigma_{22}^{AF} = \sigma_{22}^{AM} = \sigma_{22}^{A} \quad \text{(constant stress)} \qquad (3.1.1)$$
$$\varepsilon_{11}^{AF} = \varepsilon_{11}^{AM} = \varepsilon_{11}^{A} \quad \text{(constant strain)}$$

(c) For combination of region A and B, the constant strain assumptions are made, i.e.

$$\varepsilon_{11}^{A} = \varepsilon_{11}^{B} = \varepsilon_{11}$$
$$\varepsilon_{22}^{A} = \varepsilon_{22}^{B} = \varepsilon_{22} \qquad (3.1.2)$$
$$\gamma_{12}^{A} = \gamma_{12}^{B} = \gamma_{12}$$

Based on the micromechanics, the average stress and strain fields in the subregion A are treated as

$$\sigma_{ij}^{A} = \frac{1}{AF + AM} \left(\int_{AF} \sigma_{ij}^{AF} dA + \int_{AM} \sigma_{ij}^{AM} dA \right) \qquad (3.1.3)$$

$$\varepsilon_{ij}^{A} = \frac{1}{AF + AM} \left(\int_{AF} \varepsilon_{ij}^{AF} dA + \int_{AM} \varepsilon_{ij}^{AM} dA \right) \qquad (3.1.4)$$

, and the average stress and strain fields in the RVE are given by

$$\sigma_{ij} = \frac{1}{A + B} \left(\int_{A} \sigma_{ij}^{A} dA + \int_{B} \sigma_{ij}^{B} dA \right) \qquad (3.1.5)$$

$$\varepsilon_{ij} = \frac{1}{A + B} \left(\int_{A} \varepsilon_{ij}^{A} dA + \int_{B} \varepsilon_{ij}^{B} dA \right) \qquad (3.1.6)$$

The explicit forms for eqns (3.1.3)-(3.1.6) expressed in terms of local stress and strain with the assistance of eqns (3.1.1) and (3.1.2) are derived as

$$\sigma_{11}^{A} = v_1 \sigma_{11}^{AF} + v_2 \sigma_{11}^{AM}$$
$$\varepsilon_{22}^{A} = v_1 \varepsilon_{22}^{AF} + v_2 \varepsilon_{22}^{AM} \qquad (3.1.7)$$
$$\gamma_{12}^{A} = v_1 \gamma_{12}^{AF} + v_2 \gamma_{12}^{AM}$$

and

$$\sigma_{11} = v_A \sigma_{11}^{A} + v_B \sigma_{11}^{B}$$
$$\sigma_{22} = v_A \sigma_{22}^{A} + v_B \sigma_{22}^{B} \qquad (3.1.8)$$
$$\sigma_{12} = v_A \sigma_{12}^{A} + v_B \sigma_{12}^{B}$$

where

$$v_1 = \frac{h_1}{h_1 + h_2} \qquad v_2 = \frac{h_2}{h_1 + h_2} \qquad v_A = \frac{h_3}{h_3 + h_4} \qquad v_B = \frac{h_4}{h_3 + h_4} \qquad (3.1.9)$$

It is noted that v_1 and v_2, represent the volume fraction of subregions AF and AM with respective to the region A, and v_A and v_B indicate the volume fraction of regions, A, B, respectively to the RVE.   With eqns (3.1.1), (3.1.2), (3.1.7) and (3.1.8), the relationships between the subregion stresses and strains and the RVE stresses and strains were established.   To derive the stress and strain relations of the RVE, the corresponding fiber and matrix properties must be given in advance.   The fiber is considered to be an orthotropic elastic material.   Therefore, in the region AF, we have the incremental stress and strain relations

$$\{d\varepsilon^{AF}\} = [S^{AF}]\{d\sigma^{AF}\} \qquad (3.1.10)$$

where

$$[S^{AF}] = \begin{bmatrix} \dfrac{1}{E_1^F} & \dfrac{-v_{21}^F}{E_2^F} & 0 \\[2mm] \dfrac{-v_{12}^F}{E_1^F} & \dfrac{1}{E_2^F} & 0 \\[2mm] 0 & 0 & \dfrac{1}{G_{12}^F} \end{bmatrix} \qquad (3.1.11)$$

While, the matrix phase is considered to be an elastic-plastic material and can be characterized by the plasticity model mentioned in chapter 2.   Since the square fiber model is a 2-D plane stress model, the 2-D von Mises J_2 is given as

$$J_2 = \frac{1}{3}\left[\left(\sigma_{11}^{AM}\right)^2 + \left(\sigma_{22}^{AM}\right)^2 - \sigma_{11}^{AM}\sigma_{22}^{AM} + 3\left(\sigma_{12}^{AM}\right)^2 \right] \qquad (3.1.12)$$

Substituting J_2 into flow rule and following the same derivatives in chapter 2 with the assistance of power law relation given in eqn (2.2.8) leads to

$$\{d\varepsilon^{AM}\} = [S^{AM}]\{d\sigma^{AM}\} \qquad (3.1.13)$$

which gives a relation between total strain increment and stress increment for all pure matrix regions, i.e. AM and B, and the components of compliance matrix $[S^{AM}]$ in

eqn (3.1.13) were

$$S_{11}^{AM} = \frac{1}{E^M} + \frac{9}{4} An \left(\overline{\sigma}^{AM} \right)^{n-3} S_1^{AM} S_1^{AM}$$

$$S_{12}^{AM} = S_{21}^{AM} = -\frac{v^M}{E^M} + \frac{9}{4} An \left(\overline{\sigma}^{AM} \right)^{n-3} S_1^{AM} S_2^{AM}$$

$$S_{16}^{AM} = S_{61}^{AM} = \frac{9}{2} An \left(\overline{\sigma}^{AM} \right)^{n-3} S_1^{AM} S_3^{AM}$$

$$S_{22}^{AM} = \frac{1}{E^M} + \frac{9}{4} An \left(\overline{\sigma}^{AM} \right)^{n-3} S_2^{AM} S_2^{AM} \qquad (3.1.14)$$

$$S_{26}^{AM} = S_{62}^{AM} = \frac{9}{2} An \left(\overline{\sigma}^{AM} \right)^{n-3} S_2^{AM} S_3^{AM}$$

$$S_{66}^{AM} = \frac{1}{G^M} + 9An \left(\overline{\sigma}^{AM} \right)^{n-3} S_3^{AM} S_3^{AM}$$

in which

$$S_1^{AM} = \frac{1}{3} \left(2\sigma_{11}^{AM} - \sigma_{22}^{AM} \right)$$

$$S_2^{AM} = \frac{1}{3} \left(2\sigma_{22}^{AM} - \sigma_{11}^{AM} \right) \qquad (3.1.15)$$

$$S_3^{AM} = \sigma_{12}^{AM}$$

With the stresses and strains relations for subregions AF and AM (given in eqn (3.1.10) and eqn (3.1.13), respectively), the constitutive relation of subregion A was generated through eqns (3.1.1) and (3.1.7) and the explicit results are given by

$$\begin{Bmatrix} d\varepsilon_{11}^A \\ d\varepsilon_{22}^A \\ d\gamma_{12}^A \end{Bmatrix} = \begin{bmatrix} S_{11}^A & S_{12}^A & S_{13}^A \\ S_{21}^A & S_{22}^A & S_{23}^A \\ S_{61}^A & S_{62}^A & S_{66}^A \end{bmatrix} \begin{Bmatrix} d\sigma_{11}^A \\ d\sigma_{22}^A \\ d\sigma_{12}^A \end{Bmatrix} \qquad (3.1.16)$$

where

$$S_{11}^A = a_1 / E_1^F$$

$$S_{12}^A = S_{21}^A = a_2 / E_1^F - v_{12}^F / E_1^F$$

$$S_{16}^A = S_{61}^A = a_3 / E_1^F$$

$$S_{22}^A = v_1 \left(1/E_2^F - v_{12}^F a_2 / E_1^F \right) + v_2 \left(b_2 S_{21}^{AM} + S_{22}^{AM} \right) \qquad (3.1.17)$$

$$S_{26}^A = S_{62}^A = -v_1 a_3 v_{12}^F / E_1^F + v_2 \left(b_3 S_{21}^{AM} + S_{26}^{AM} \right)$$

$$S_{66}^A = v_1 / G_{12}^F + v_2 \left(b_3 S_{61}^{AM} + S_{66}^{AM} \right)$$

in which

$$a_1 = (1 - v_2 b_1)/v_1$$
$$a_2 = -v_2 b_2/v_1$$
$$a_3 = -v_2 b_3/v_1$$
$$b_1 = \left(v_1 E_1^F S_{11}^{AM} + v_2\right)^{-1}$$
$$b_2 = -v_1 \left(E_1^F S_{12}^{AM} + v_{12}^F\right)\left(v_1 E_1^F S_{11}^{AM} + v_2\right)^{-1}$$
$$b_3 = -v_1 E_1^F S_{16}^{AM}\left(v_1 E_1^F S_{11}^{AM} + v_2\right)^{-1}$$

(3.1.18)

Inverting eqn (3.1.16), we obtain

$$\{d\sigma^A\} = [C^A]\{d\varepsilon^A\}$$

(3.1.19)

where

$$[C^A] = [S^A]^{-1}$$

(3.1.20)

For the region B, since it is matrix materials, the compliance matrix is exactly the same as that in eqn (3.1.13). Thus, the incremental stresses and strain relation is expressed as
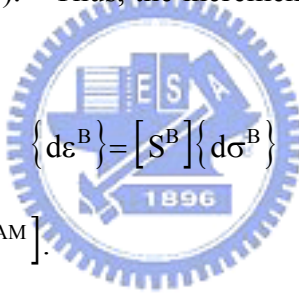
$$\{d\varepsilon^B\} = [S^B]\{d\sigma^B\}$$

(3.1.21)

, and $[S^B]$ is the same as $[S^{AM}]$.

Inverting eqn (3.1.21), we obtain

$$\{d\sigma^B\} = [C^B]\{d\varepsilon^B\}$$

(3.1.22)

where

$$[C^B] = [S^B]^{-1}$$

(3.1.23)

Again, with constitutive relation of region A and B (given by (3.1.19), and (3.1.21)), through eqn (3.1.8) and eqns (3.1.2), the incremental stress and strain relation of entire RVE was derived as

$$\{d\sigma\} = [C]\{d\varepsilon\}$$

(3.1.24)

where

$$[C] = v_A[C^A] + v_B[C^B]$$

(3.1.25)

With eqn (3.1.24), for a given loading history, the constitutive relation of the composites can be generated by using the numerical iteration. At the beginning, the overall stiffness matrix $[C]$ of composites in eqn (3.1.24) was constructed with initial stress states equal to zero. For a tiny stress increment, the corresponding strain increment was calculated from eqn (3.1.24). The strain increments in RVE are exactly the same as those in regions A and B based on the constant strain assumption given in eqn (3.1.2), and the corresponding stress increments in the two regions were evaluated with the assistance of the respective constitutive law given in eqns (3.1.19) and (3.1.22). Since region B was pure matrix, its stress components was directly substituted into eqn (3.1.14) to update the stiffness matrix $[C^B]$. However, for region A, there are two subregions, AM and AF enclosed. In order to update the stiffness matrix $[C^A]$, the stress components in the subregion AM need to be evaluated, since the compliance matrix $[S^{AM}]$ in eqn (3.1.13) is dependent on the stress states. The incremental stress states $d\sigma_{22}^{AM}$ and $d\sigma_{12}^{AM}$ in the subregion AM can be evaluated directly from $d\sigma_{22}^{A}$ and $d\sigma_{12}^{A}$ in the region A based on the constant stress assumption. Similarly, the incremental strain sate $d\varepsilon_{11}^{AM}$ was also obtained from $d\varepsilon_{11}^{A}$ with constant strain assumption. Once the stress components $d\sigma_{22}^{AM}$ and $d\sigma_{12}^{AM}$ and the strain component $d\varepsilon_{11}^{AM}$ were determined, the stress increment $d\sigma_{11}^{AM}$ could be derived through the first relation of eqn (3.1.13). With the stress components in the subregion AM, the corresponding compliance $[S^{AM}]$ matrix in eqn (3.1.13) was renewed. By combining the compliance $[S^{AF}]$ of subregion AF, an updated stiffness matrix $[C^A]$ was obtained and thereafter, the new stiffness $[C]$ of the RVE was calculated which was employed to evaluate the strain increment in the next step associated with other tiny stress increments. The detail program for the

SFM combined with three parameters model was attached in the Appendix A.

3.2 Modified Square Fiber Model

Since the square fiber model (SFM) proposed by Sun and Chen [12] was derived based on the square edge packing with a square fiber inside, it is difficult to deal with the RVE with circular fiber together with different fiber arrangements by using the SFM. To overcome this problem, a modified SFM was proposed in this section by dividing the representative volume element (RVE) into numbers of horizontal tiny subcells. The constant stress (or constant strain) conditions applied in the SFM (shown in the previous section) were again employed at each subcells in the modified SFM. There are two fiber arrangements considered here, i.e. square edge packing array and square diagonal packing array, which were illustrated respectively in Fig. 3.1(a) and Fig. 3.1(b).
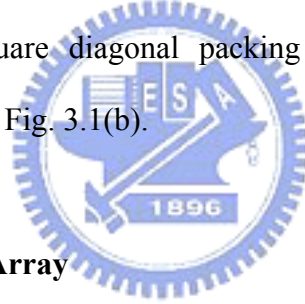
3.2.1 Square Edge Packing Array

In the case of square edge packing array as shown in Fig. 3.3, the RVE consists of a region A with a height h_f equal to the radius r of the fiber and a pure matrix region B with a height of h_m which is equal to $l - r$. It is noted that l is the length of the square RVE. There are two subregions AF and AM contained in the region A. The region A was divided into N subcells horizontally from A_1 to A_n and the height of each subcell is h_f/N. Thus, in each subregion A_n consisting of AF_n and AM_n, the stress and strain fields follow constant stress or constant strain assumptions, i.e.

$$\sigma_{12}^{AF_n} = \sigma_{12}^{AM_n} = \sigma_{12}^{A_n}$$
$$\sigma_{22}^{AF_n} = \sigma_{22}^{AM_n} = \sigma_{22}^{A_n} \qquad n = 1,2,3,...,N \qquad (3.2.1)$$
$$\varepsilon_{11}^{AF_n} = \varepsilon_{11}^{AM_n} = \varepsilon_{11}^{A_n}$$

On the other hand, for the RVE, the following assumptions were applied,

$$\varepsilon_{11}^{A_1} = \varepsilon_{11}^{A_2} = \cdots = \varepsilon_{11}^{A_N} = \varepsilon_{11}^{B} = \varepsilon_{11}$$
$$\varepsilon_{22}^{A_1} = \varepsilon_{22}^{A_2} = \cdots = \varepsilon_{22}^{A_N} = \varepsilon_{22}^{B} = \varepsilon_{22} \qquad (3.2.2)$$
$$\gamma_{12}^{A_1} = \gamma_{12}^{A_2} = \cdots = \gamma_{12}^{A_N} = \gamma_{12}^{B} = \gamma_{12}$$

Based on the micromechanics, the average stress and strain fields for each subcell A_n are defined as

$$\sigma_{ij}^{A_n} = \frac{1}{AF_n + AM_n}\left(\int_{AF_n} \sigma_{ij}^{AF_n} dA + \int_{AM_n} \sigma_{ij}^{AM_n} dA \right) \qquad (3.2.3)$$

$$\varepsilon_{ij}^{A_n} = \frac{1}{AF_n + AM_n}\left(\int_{AF_n} \varepsilon_{ij}^{AF_n} dA + \int_{AM_n} \varepsilon_{ij}^{AM_n} dA \right) \qquad (3.2.4)$$

and, for the RVE, they are given by

$$\sigma_{ij} = \frac{1}{B + \sum_{n=1}^{N} A_n}\left(\int_{B} \sigma_{ij}^{B} dA + \sum_{n=1}^{N}\int_{A_n} \sigma_{ij}^{A_n} dA \right) \qquad (3.2.5)$$

$$\varepsilon_{ij} = \frac{1}{B + \sum_{n=1}^{N} A_n}\left(\int_{B} \varepsilon_{ij}^{B} dA + \sum_{n=1}^{N}\int_{A_n} \varepsilon_{ij}^{A_n} dA \right) \qquad (3.2.6)$$

Substituting eqns (3.2.1) and (3.2.2) into eqns (3.2.3)-(3.2.6) yields

$$\sigma_{11}^{A_n} = v^{AF_n}\sigma_{11}^{AF_n} + v^{AM_n}\sigma_{11}^{AM_n}$$
$$\varepsilon_{22}^{A_n} = v^{AF_n}\varepsilon_{22}^{AF_n} + v^{AM_n}\varepsilon_{22}^{AM_n} \qquad n = 1,2,3,...N \qquad (3.2.7)$$
$$\gamma_{12}^{A_n} = v^{AF_n}\gamma_{12}^{AF_n} + v^{AM_n}\gamma_{12}^{AM_n}$$

and

$$\sigma_{11} = \sum_{n=1}^{N}\left(v^{A_n}\sigma_{11}^{A_n} \right) + v^{B}\sigma_{11}^{B}$$

$$\sigma_{22} = \sum_{n=1}^{N}\left(v^{A_n}\sigma_{22}^{A_n} \right) + v^{B}\sigma_{22}^{B} \qquad (3.2.8)$$

$$\sigma_{12} = \sum_{n=1}^{N}\left(v^{A_n}\sigma_{12}^{A_n} \right) + v^{B}\sigma_{12}^{B}$$

where v^{AF_n} and v^{AM_n} represent the volume fraction of fiber and matrix phases with respect to the subcell A_n, and v^{A_n} and v^{B} denote the volume fraction of subregion A_n and subregion B with respect to entire RVE, respectively. Based on geometric correlation given in Fig. 3.2, the volume fractions, v^{A_n} and v^{B} can be

determined directly as

$$v^{A_n} = \frac{h_f / N}{h_f + h_m}$$

$$v^B = \frac{h_m}{h_f + h_m} \tag{3.2.9}$$

However, in order to evaluate the volume fraction, v^{AF_n} and v^{AM_n} in the subcell A_n with convenience, the angle θ_n was defined as the orientation of the ray emanating from the fiber center to the intersection of the fiber circumference and the nth horizontal grid line. Thus, the corresponding volume fraction is written as

$$v^{AF_n} = \frac{r \cos \theta_n}{l} \qquad v^{AM_n} = 1 - v^{AF_n} \tag{3.2.10}$$

where

$$\theta_n = \sin^{-1} \frac{(n-1) h_f}{rN} \qquad n = 1,2,3,...,N \tag{3.2.11}$$

can be determined from the geometric correlation given in Fig. 3.2. For the sub-region A_n, it has the same constitutive relation as shown in eqn (3.1.16) except that the volume fractions v_1 and v_2 are replaced by v^{AF_n} and v^{AM_n}, respectively, and also that in the sub-cell AM_n, the compliance matrix becomes $\left[S^{AM_n} \right]$ instead of $\left[S^{AM} \right]$. Therefore, the constitutive equation for subcell A_n is expressed as

$$\begin{Bmatrix} d\varepsilon_{11}^{A_n} \\ d\varepsilon_{22}^{A_n} \\ d\gamma_{12}^{A_n} \end{Bmatrix} = \begin{bmatrix} S_{11}^{A_n} & S_{12}^{A_n} & S_{13}^{A_n} \\ S_{21}^{A_n} & S_{22}^{A_n} & S_{23}^{A_n} \\ S_{61}^{A_n} & S_{62}^{A_n} & S_{66}^{A_n} \end{bmatrix} \begin{Bmatrix} d\sigma_{11}^{A_n} \\ d\sigma_{22}^{A_n} \\ d\sigma_{12}^{A_n} \end{Bmatrix} \tag{3.2.12}$$

where

$$S_{11}^{A_n} = a_1 / E_1^F$$

$$S_{12}^{A_n} = S_{21}^{A_n} = a_2 / E_1^F - v_{12}^F / E_1^F$$

$$S_{16}^{A_n} = S_{61}^{A_n} = a_3 / E_1^F$$

$$S_{22}^{A_n} = v^{AF_n} \left(1/E_2^F - v_{12}^F a_2 / E_1^F \right) + v^{AM_n} \left(b_2 S_{21}^{AM_n} + S_{22}^{AM_n} \right)$$

$$S_{26}^{A_n} = S_{62}^{A_n} = -v^{AF_n} a_3 v_{12}^F / E_1^F + v^{AM_n} \left(b_3 S_{21}^{AM_n} + S_{26}^{AM_n} \right)$$

$$S_{66}^{A_n} = v^{AF_n} / G_{12}^F + v^{AM_n} \left(b_3 S_{61}^{AM_n} + S_{66}^{AM_n} \right)$$

(3.2.13)

in which

$$a_1 = \left(1 - v^{AM_n} b_1 \right) / v^{AF_n}$$

$$a_2 = -v^{AM_n} b_2 / v^{AF_n}$$

$$a_3 = -v^{AM_n} b_3 / v^{AF_n}$$

$$b_1 = \left(v^{AF_n} E_1^F S_{11}^{AM_n} + v^{AM_n} \right)^{-1}$$

$$b_2 = -v^{AF_n} \left(E_1^F S_{12}^{AM_n} + v_{12}^F \right) \left(v^{AF_n} E_1^F S_{11}^{AM_n} + v^{AM_n} \right)^{-1}$$

$$b_3 = -v^{AF_n} E_1^F S_{16}^{AM_n} \left(v^{AF_n} E_1^F S_{11}^{AM_n} + v^{AM_n} \right)^{-1}$$

(3.2.14)

where $\left[S^{An} \right]$ is the compliance matrix of subcell A_n. It is to be noted that the mathematical form of compliance matrix $\left[S^{AM_n} \right]$ is the same as that in eqn (3.1.13), which was evaluated in terms of the current stress states of subcell AM_n.

Again, for the region B, the constitutive equation is the same as eqn (3.1.21) which was rewritten as

$$\left\{ d\varepsilon^B \right\} = \left[S^B \right] \left\{ d\sigma^B \right\}$$

(3.2.15)

With ingredient constitutive equations given in eqns (3.2.12) and (3.2.15) together with eqns (3.2.2), (3.2.8), we derived the incremental form of overall constitutive equation as

$$\left\{ d\sigma \right\} = \left[C \right] \left\{ d\varepsilon \right\}$$

(3.2.16)

where

$$[C] = v^{A_1} \left[C^{A_1} \right] + v^{A_2} \left[C^{A_2} \right] + \cdots + v^{A_N} \left[C^{A_N} \right] + v^B \left[C^B \right]$$

$$= \sum_{n=1}^{N} v^{A_n} \left[C^{A_n} \right] + v^B \left[C^B \right]$$

(3.2.17)

3.2.2 Square Diagonal Packing Array

In addition to the square edge packing array for the fiber arrangement, there are other fiber arrangements called the square diagonal packing (SDP) array which will be discussed in this section. Fig. 3.1(b) shows the typical RVE for this fiber arrangement. Because of symmetry, only one quarter of the RVE will be considered in the analysis. In fact, due to different fiber fractions, there are three possible situations to be accounted for the generation of the constitutive relations as shown in Fig 3.4. It was found that the critical fiber volume fraction for SDP is 39.3 %. Above this value, two quarter fibers will have interaction within the center region of the RVE as shown in Fig. 3.4(c). It was noted that Fig. 3.4(d) shows the maximum fiber volume fraction of SDP is 78.5 %. Since, in industrial applications of fiber composites, the fiber volume fraction is around 60% which is greater than the critical value, and thus we only consider the case with higher volume fractions. As shown in Fig. 3.5, the RVE was separated into three partitions initially with two horizontal lines. One was along the top of the left fiber and the other was passing through the bottom of the right fiber. Let us denote the center region as subregion B with a height of h_B which is equal to $2r - l$, and the other two regions as subregion A with the individual height, h_A, equal to $l - r$, where l is the length of the square RVE and r is the radius of the fiber. Noted that there are two subregions, i.e., AF (fiber phase of region A) and AM (matrix phase of region A) contained in the region A, and three subregions, i.e., BFL (fiber phase in the left side of region B), BM (matrix phase of region B) and BFR (fiber phase in the right side of region B), were included in the region B. Subsequently, regions A and B were divided into N and M horizontal subcells, represented by A_n and B_n respectively, such that totally there are 2N+M subcells enclosed in the RVE. The height for each subcell A_n in region A is h_A/N, while for subcell B_n in region B, the height is h_B/M. In order to determine the

fiber volume fraction in the region An, the angle θ_{A_n} as shown in Fig. 3.5, were

defined in the same manner as described in the previous section.   In addition, for the

region B, two angles, i.e., ϕ_{B_n} and θ_{B_n}, as shown in Fig. 3.5 were defined based on

the orientation of the ray starting from the fiber center to the intersection of the nth

grid line and the fiber circumference.   It is noted that the two angles are not

independent but correlated by following the relation.

$$\phi_{B_n} = \theta_{B_{n+M-2}} \qquad\qquad n = 2,3,...,M+1 \qquad\qquad (3.2.18)$$

In addition, the corresponding angles can be expressed explicitly as

$$
\begin{aligned}
\theta_{A_n} &= \sin^{-1} \frac{(n-1)h_A}{rN} &\qquad n = 1,2,3,...,N \\
\theta_{B_n} &= \sin^{-1} \frac{Mh_A + (n-1)h_B}{rM} &\qquad n = 1,2,3,...,M
\end{aligned}
\qquad (3.2.19)
$$

which determined from the geometric correlation shown in Fig. 3.5.

In addition, there are two areas covered by region A and both of the areas are the

same.   Thus, only one area was taken into account in the analysis.   For each subcell

A_n, subregions AF_n and AM_n would follow the constant stress and constant strain

assumptions, i.e.

$$
\begin{aligned}
\sigma_{12}^{AF_n} &= \sigma_{12}^{AM_n} = \sigma_{12}^{A_n} \\
\sigma_{22}^{AF_n} &= \sigma_{22}^{AM_n} = \sigma_{22}^{A_n} &\qquad n = 1,2,3,...,N \\
\varepsilon_{11}^{AF_n} &= \varepsilon_{11}^{AM_n} = \varepsilon_{11}^{A_n}
\end{aligned}
\qquad (3.2.20)
$$

Similarly, in each subcell B_n, all subregions BFL_n, BM_n and BFR_n obey

$$
\begin{aligned}
\sigma_{12}^{BFL_n} &= \sigma_{12}^{BM_n} = \sigma_{12}^{BFR_n} = \sigma_{12}^{B_n} \\
\sigma_{22}^{BFL_n} &= \sigma_{22}^{BM_n} = \sigma_{22}^{BFR_n} = \sigma_{22}^{B_n} &\qquad n = 1,2,3,...,M \\
\varepsilon_{11}^{BFL_n} &= \varepsilon_{11}^{BM_n} = \varepsilon_{11}^{BFR_n} = \varepsilon_{11}^{B_n}
\end{aligned}
\qquad (3.2.21)
$$

For the RVE, the following assumptions were applied,

29

$$\varepsilon_{11}^{A_1} = \varepsilon_{11}^{A_2} = \cdots = \varepsilon_{11}^{A_N} = \varepsilon_{11}^{B_1} = \varepsilon_{11}^{B_2} = \cdots = \varepsilon_{11}^{B_M} = \varepsilon_{11}$$

$$\varepsilon_{22}^{A_1} = \varepsilon_{22}^{A_2} = \cdots = \varepsilon_{22}^{A_N} = \varepsilon_{22}^{B_1} = \varepsilon_{22}^{B_2} = \cdots = \varepsilon_{22}^{B_M} = \varepsilon_{22} \qquad (3.2.22)$$

$$\gamma_{12}^{A_1} = \gamma_{12}^{A_2} = \cdots = \gamma_{12}^{A_N} = \gamma_{12}^{B_1} = \gamma_{12}^{B_2} = \cdots = \gamma_{12}^{B_M} = \gamma_{12}$$

The average stress and strain fields in subcells A_n, B_n and the RVE can be defined as

$$\sigma_{ij}^{A_n} = \frac{1}{AF_n + AM_n}\left(\int_{AF_n} \sigma_{ij}^{AF_n} dA + \int_{AM_n} \sigma_{ij}^{AM_n} dA \right) \qquad (3.2.23)$$

$$\varepsilon_{ij}^{A_n} = \frac{1}{AF_n + AM_n}\left(\int_{AF_n} \varepsilon_{ij}^{AF_n} dA + \int_{AM_n} \varepsilon_{ij}^{AM_n} dA \right) \qquad (3.2.24)$$

$$\sigma_{ij}^{B_n} = \frac{1}{BFL_n + BM_n + BFR_n}\left(\int_{BFL_n} \sigma_{ij}^{BFL_n} dA + \int_{BM_n} \sigma_{ij}^{BM_n} dA + \int_{BFR_n} \sigma_{ij}^{BFR_n} dA \right) \qquad (3.2.25)$$

$$\varepsilon_{ij}^{B_n} = \frac{1}{BFL_n + BM_n + BFR_n}\left(\int_{BFL_n} \varepsilon_{ij}^{BFL_n} dA + \int_{BM_n} \varepsilon_{ij}^{BM_n} dA + \int_{BMR_n} \varepsilon_{ij}^{BMR_n} dA \right) \qquad (3.2.26)$$

$$\sigma_{ij} = \frac{1}{2\sum\limits_{n=1}^{N} A_n + \sum\limits_{n=1}^{M} B_n}\left(2\sum\limits_{n=1}^{N} \int_{A_n} \sigma_{ij}^{A_n} dA + \sum\limits_{n=1}^{M} \int_{B_n} \sigma_{ij}^{B_n} dA \right) \qquad (3.2.27)$$

$$\varepsilon_{ij} = \frac{1}{2\sum\limits_{n=1}^{N} A_n + \sum\limits_{n=1}^{M} B_n}\left(2\sum\limits_{n=1}^{N} \int_{A_n} \varepsilon_{ij}^{A_n} dA + \sum\limits_{n=1}^{M} \int_{B_n} \varepsilon_{ij}^{B_n} dA \right) \qquad (3.2.28)$$

Although there are two fiber phases BFL_n and BFR_n in each subcell B_n, it can be demonstrated that these two isolated fiber phases can be treated as a whole one BF_n and the constant stress and constant strain conditions mentioned previously are still remained. Thus, the fiber volume fraction in this region can be represented using only one variable v^{BF_n} as shown in Fig. 3.6. By substituting eqns (3.2.20)-(3.2.22) into eqns (3.2.23)-(3.2.28), the following equations were obtained.

$$\sigma_{11}^{A_n} = v^{AF_n}\sigma_{11}^{AF_n} + v^{AM_n}\sigma_{11}^{AM_n}$$

$$\varepsilon_{22}^{A_n} = v^{AF_n}\varepsilon_{22}^{AF_n} + v^{AM_n}\varepsilon_{22}^{AM_n} \qquad (3.2.29)$$

$$\gamma_{12}^{A_n} = v^{AF_n}\gamma_{12}^{AF_n} + v^{AM_n}\gamma_{12}^{AM_n}$$

$$\sigma_{11}^{B_n} = v^{BF_n} \sigma_{11}^{BF_n} + v^{BM_n} \sigma_{11}^{BM_n}$$

$$\varepsilon_{22}^{B_n} = v^{BF_n} \varepsilon_{22}^{BF_n} + v^{BM_n} \varepsilon_{22}^{BM_n} \qquad (3.2.30)$$

$$\gamma_{12}^{B_n} = v^{BF_n} \gamma_{12}^{BF_n} + v^{BM_n} \gamma_{12}^{BM_n}$$

and

$$\sigma_{11} = 2\sum_{n=1}^{N} v^{A_n} \sigma_{11}^{A_n} + \sum_{n=1}^{M} v^{B_n} \sigma_{11}^{B_n}$$

$$\sigma_{22} = 2\sum_{n=1}^{N} v^{A_n} \sigma_{22}^{A_n} + \sum_{n=1}^{M} v^{B_n} \sigma_{22}^{B_n} \qquad (3.2.31)$$

$$\sigma_{12} = 2\sum_{n=1}^{N} v^{A_n} \sigma_{12}^{A_n} + \sum_{n=1}^{M} v^{B_n} \sigma_{12}^{B_n}$$

in which

$$v^{AF_n} = \frac{r\cos\theta_{A_n}}{l} \qquad\qquad v^{AM_n} = 1 - v^{AF_n}$$

$$v^{BF_n} = \frac{r\cos\theta_{B_n} + r\cos\phi_{B_{n+1}}}{l} \qquad v^{BM_n} = 1 - v^{BF_n} \qquad (3.2.32)$$

$$v^{A_n} = \frac{h_A/N}{2h_A + h_B} \qquad\qquad v^{B_n} = \frac{h_B/M}{2h_A + h_B}$$

where v^{AF_n} and v^{AM_n} represent the volume fraction of the fiber and matrix with respect to subcell A_n while v^{BF_n} and v^{BM_n} denote the volume fraction of the fiber and matrix respectively to subcell B_n. And v^{A_n} and v^{B_n} are the volume fraction of subcell A_n and B_n with respect to the RVE.

Similar to square edge packing array, the constitutive equations of subcells A_n and B_n were the same as eqn (3.2.12) except that the volume fraction were replaced with eqn (3.2.32). Furthermore, the compliance matrix of the matrix phase was evaluated according to individual stress states in each tiny step associated with the loading history. Since the procedure for the formulation had been described in previous section 3.2.1, the detail processes were not repeated here. As a result, the constitutive equations of subcells A_n and B_n can be written as

$$\{d\sigma^{A_n}\} = [C^{A_n}]\{d\varepsilon^{A_n}\} \qquad (3.2.33)$$

31

and

$$\left\{ d\sigma^{B_n} \right\} = \left[C^{B_n} \right] \left\{ d\varepsilon^{B_n} \right\} \qquad (3.2.34)$$

where $\left[C^{A_n} \right]$ and $\left[C^{B_n} \right]$ are the stiffness matrix of regions A_n and B_n, respectively.

From eqn (3.2.31) together with eqns (3.2.22), (3.2.33), (3.2.34), the overall constitutive equation can be represented by a incremental form,

$$\left\{ d\sigma \right\} = \left[C \right] \left\{ d\varepsilon \right\} \qquad (3.2.35)$$

where

$$[C] = 2\sum_{n=1}^{N} v^{A_n} \left[C^{A_n} \right] + \sum_{n=1}^{M} v^{B_n} \left[C^{B_n} \right] \qquad (3.2.36)$$

Chapter 4 Generalized Method of Cells

In order to realize the nonlinear rate dependent behavior, the micromechanical approach was employed with the ingredient material properties in the analysis.   In chapter three, the square fiber model and modified square fiber model were proposed to characterize the material properties of composites.   While, in this chapter, the generalized method of cells (GMC) proposed by Paley and Aboudi [15] will be adopted for investigations.   However, some interpretations and reorganizations on the derivation of GMC will be conducted by the present author to easily extend the GMC for modeling the nonlinear rate dependent behavior of composites.

4.1 Generalized Method of Cells (GMC)

The generalized method of cells proposed by Paley and Aboudi [15] was adopted for investigating the nonlinear behavior of composites.   The corresponding mechanical properties of the composites can be derived from a repeating microstructure of the composite so called a representative volume element (RVE). In GMC, the RVE were divided into many rectangular subcells $(\beta\gamma)$ with $\beta = 1,....,N_\beta$ and $\gamma = 1,...,N_\gamma$, and depending on the fiber arrangement, each subcell indicates either fiber or matrix on the RVE.   In Fig. 4.1, the fiber extends in the x_1 direction and the area of each subcell is equal to $N_\beta l_\gamma$.   Assume that a local coordinate system $\left(x_1, \overline{x}_2^{(\beta)}, \overline{x}_3^{(\gamma)}\right)$ locate at the center of each subcell (see Fig. 4.2). When the RVE deforms, the displacement rates $\dot{u}_i^{(\beta\gamma)}$ for each subcell was assumed to be a linear expansion in terms of the distances from the center of the subcell, it is

$$\dot{u}_i^{(\beta\gamma)} = \dot{w}_i^{(\beta\gamma)}\left(x_1, x_2, x_3\right) + \overline{x}_2^{(\beta)}\dot{\phi}_i^{(\beta\gamma)} + \overline{x}_3^{(\gamma)}\dot{\psi}_i^{(\beta\gamma)} \qquad i = 1, 2, 3 \qquad (4.1.1)$$

where $\dot{w}_i^{(\beta\gamma)}$ is the displacement rate at the center of the subcell, which could be

different from subcell to subcell. It is to be noted that this displacement function is expressed in terms of the global coordinate system (x_1, x_2, x_3) [13]. In eqn (4.1.1), $\dot{\phi}_i^{(\beta\gamma)}$, $\dot{\psi}_i^{(\beta\gamma)}$ are variables rates which could be realized as a constant in each subcell. Based on elasticity, the small strain rate tensor is written as

$$\eta_{ij}^{(\beta\gamma)} = \frac{1}{2}\left(\partial_i \dot{u}_j^{(\beta\gamma)} + \partial_j \dot{u}_i^{(\beta\gamma)}\right) \quad i, j = 1, 2, 3 \tag{4.1.2}$$

where $\partial_1 = \partial/\partial x_1$, $\partial_2 = \partial/\partial \overline{x}_2^{(\beta)}$ and $\partial_3 = \partial/\partial \overline{x}_3^{(\gamma)}$. Substituting eqn (4.1.1) into eqn (4.1.2) and then using the average formula of micromechanics

$$\overline{\eta}_{ij}^{(\beta\gamma)} = \frac{1}{h_\beta l_\gamma}\int_{-l_\gamma/2}^{l_\gamma/2}\int_{-h_\beta/2}^{h_\beta/2}\eta_{ij}^{(\beta\gamma)}d\overline{x}_2^{(\beta)}d\overline{x}_3^{(\gamma)} \tag{4.1.3}$$

we can obtain the average strain rates in any subcell $(\beta\gamma)$, i.e.

$$\begin{aligned}
\overline{\eta}_{11}^{(\beta\gamma)} &= \frac{\partial}{\partial x_1}\dot{w}_1^{(\beta\gamma)} \\
\overline{\eta}_{22}^{(\beta\gamma)} &= \dot{\phi}_2^{(\beta\gamma)} \\
\overline{\eta}_{33}^{(\beta\gamma)} &= \dot{\psi}_3^{(\beta\gamma)} \\
2\overline{\eta}_{23}^{(\beta\gamma)} &= \dot{\phi}_3^{(\beta\gamma)} + \dot{\psi}_2^{(\beta\gamma)} \\
2\overline{\eta}_{13}^{(\beta\gamma)} &= \dot{\psi}_1^{(\beta\gamma)} + \frac{\partial}{\partial x_1}\dot{w}_3^{(\beta\gamma)} \\
2\overline{\eta}_{12}^{(\beta\gamma)} &= \dot{\phi}_1^{(\beta\gamma)} + \frac{\partial}{\partial x_1}\dot{w}_2^{(\beta\gamma)}
\end{aligned} \tag{4.1.4}$$

Under deformation, the displacement rates should be continuous at the interfaces between the internal subcells and between neighboring repeating RVE. This leads to the following relations

$$\dot{u}_i^{(\beta\gamma)}\big|_{\overline{x}_2^{(\beta)}=h_\beta/2} = \dot{u}_i^{(\hat{\beta}\gamma)}\big|_{\overline{x}_2^{(\hat{\beta})}=-h_{\hat{\beta}}/2} \tag{4.1.5}$$

$$\dot{u}_i^{(\beta\gamma)}\big|_{\overline{x}_3^{(\gamma)}=l_\gamma/2} = \dot{u}_i^{(\beta\hat{\gamma})}\big|_{\overline{x}_3^{(\hat{\gamma})}=-l_{\hat{\gamma}}/2} \tag{4.1.6}$$

where $\hat{\beta}$ and $\hat{\gamma}$ are defined by

$$\hat{\beta} = \begin{cases} \beta+1, & \beta < N_\beta \\ 1, & \beta = N_\beta \end{cases} \tag{4.1.7}$$

and

$$\hat{\gamma} = \begin{cases} \gamma + 1, & \gamma < N_\gamma \\ 1, & \gamma = N_\gamma \end{cases} \tag{4.1.8}$$

Note that $\hat{\beta} = 1$ for $\beta = N_\beta$ and $\hat{\gamma} = 1$ for $\gamma = N_\gamma$ are employed to represent the periodic boundary conditions. Instead of using the displacement continuity conditions from point to point as given in (4.1.5), Paley and Aboudi imposed the continuity condition on an average sense as

$$\int_{-l_\gamma/2}^{l_\gamma/2} \dot{u}_i^{(\beta\gamma)} \big|_{\bar{x}_2^{(\beta)}=h_\beta/2} \, d\bar{x}_3^{(\gamma)} = \int_{-l_\gamma/2}^{l_\gamma/2} \dot{u}_i^{(\hat{\beta}\gamma)} \big|_{\bar{x}_2^{(\hat{\beta})}=-h_{\hat{\beta}}/2} \, d\bar{x}_3^{(\gamma)} \tag{4.1.9}$$

Using eqn (4.1.1), it follows that

$$\dot{w}_i^{(\beta\gamma)} + \frac{1}{2}h_\beta \dot{\phi}_i^{(\beta\gamma)} = \dot{w}_i^{(\hat{\beta}\gamma)} - \frac{1}{2}h_{\hat{\beta}} \dot{\phi}_i^{(\hat{\beta}\gamma)} \tag{4.1.10}$$

A similar relation obtained from eqn (4.1.6) with the integration from $-h_\beta/2$ to $h_\beta/2$ with respect to $\bar{x}_2^{(\beta)}$ was given by

$$\dot{w}_i^{(\beta\gamma)} + \frac{1}{2}l_\gamma \dot{\psi}_i^{(\beta\gamma)} = \dot{w}_i^{(\beta\hat{\gamma})} - \frac{1}{2}l_{\hat{\gamma}} \dot{\psi}_i^{(\beta\hat{\gamma})} \tag{4.1.11}$$

Apparently, both eqns (4.1.10) and (4.1.11) represent the displacement continuity in the interfaces between the subcells and all field quantities are originated from the centerline $x_2^{(\beta)}$ of the subcell $(\beta\gamma)$ and the centerline $x_2^{(\hat{\beta})}$ of the subcell $(\hat{\beta}\gamma)$ as shown in Fig. 4.2. These discrete field quantities can also be observed directly from the interface rather than from the central line, which could be done simply by introducing the location of the interface $x_2^{(I)}$ between subcells $(\beta\gamma)$ and $(\hat{\beta}\gamma)$ as

$$x_2^{(\beta)} = x_2^{(I)} - \frac{1}{2}h_\beta \tag{4.1.12}$$

$$x_2^{(\hat{\beta})} = x_2^{(I)} + \frac{1}{2}h_{\hat{\beta}} \tag{4.1.13}$$

Through a Taylor expansion of the field variables in eqn (4.1.10) with only linear

terms kept, we have

$$\dot{w}_i^{(\beta\gamma)} - \frac{1}{2}h_\beta \left(\frac{\partial}{\partial x_2} \dot{w}_i^{(\beta\gamma)} - \dot{\phi}_i^{(\beta\gamma)} \right) = \dot{w}_i^{(\hat{\beta}\gamma)} + \frac{1}{2}h_{\hat{\beta}} \left(\frac{\partial}{\partial x_2} \dot{w}_i^{(\hat{\beta}\gamma)} - \dot{\phi}_i^{(\hat{\beta}\gamma)} \right) \qquad (4.1.14)$$

It is noted that all field variables in eqn (4.1.14) are evaluated at the interface $x_2^{(I)}$.

The displacement continuity also implies the field variables of the $\dot{w}_i^{(\beta\gamma)}$ and $\dot{w}_i^{(\hat{\beta}\gamma)}$ expressed in terms of the position vectors on the interface should be the same as

$$\dot{w}_i^{(\beta\gamma)} = \dot{w}_i^{(\hat{\beta}\gamma)} \qquad (4.1.15)$$

Define

$$F_i^{(\beta)} = \dot{w}_i^{(\beta\gamma)} + f_i^{(\beta)} - \dot{w}_i^{(\hat{\beta}\gamma)} + f_i^{(\hat{\beta})} \qquad (4.1.16)$$

where

$$f_i^{(\beta)} = -\frac{1}{2}h_\beta \left(\frac{\partial}{\partial x_2} \dot{w}_i^{(\beta\gamma)} - \dot{\phi}_i^{(\beta\gamma)} \right) \qquad (4.1.17)$$

Therefore, eqn (4.1.14) can be expressed in a compact form as

$$F_i^{(\beta)} = 0 \qquad \beta = 1,...,N_\beta \qquad (4.1.18)$$

Similarly, eqn (4.1.11) provides the continuity relations

$$\dot{w}_i^{(\beta\gamma)} - \frac{1}{2}l_\gamma \left(\frac{\partial}{\partial x_3} \dot{w}_i^{(\beta\gamma)} - \dot{\psi}_i^{(\beta\gamma)} \right) = \dot{w}_i^{(\beta\hat{\gamma})} + \frac{1}{2}l_{\hat{\gamma}} \left(\frac{\partial}{\partial x_3} \dot{w}_i^{(\beta\hat{\gamma})} - \dot{\psi}_i^{(\beta\hat{\gamma})} \right) \qquad (4.1.19)$$

and can be expressed in a compact form similar to eqn (4.1.18) as

$$G_i^{(\gamma)} = 0 \qquad \gamma = 1,...,N_\gamma \qquad (4.1.20)$$

where the following definitions have been employed

$$G_i^{(\gamma)} = \dot{w}_i^{(\beta\gamma)} + g_i^{(\gamma)} - \dot{w}_i^{(\beta\hat{\gamma})} + g_i^{(\hat{\gamma})} \qquad (4.1.21)$$

$$g_i^{(\gamma)} = -\frac{1}{2}l_\gamma \left(\frac{\partial}{\partial x_3} \dot{w}_i^{(\beta\gamma)} - \dot{\psi}_i^{(\beta\gamma)} \right) \qquad (4.1.22)$$

From eqns (4.1.18) and (4.1.20), we obtain
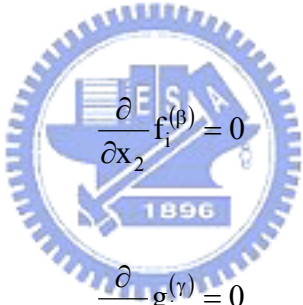
$$\sum_{\beta=1}^{N_\beta} F_i^{(\beta)} = 0 \tag{4.1.23}$$

$$\sum_{\gamma=1}^{N_\gamma} G_i^{(\gamma)} = 0 \tag{4.1.24}$$

It can be shown from eqns (4.1.23) and (4.1.24) together with periodic boundary conditions, i.e. eqns (4.1.7) and (4.1.8), that

$$\sum_{\beta=1}^{N_\beta} f_i^{(\beta)} = 0 \tag{4.1.25}$$

$$\sum_{\gamma=1}^{N_\gamma} g_i^{(\gamma)} = 0 \tag{4.1.26}$$

Since

$$\frac{\partial}{\partial x_2} f_i^{(\beta)} = 0 \tag{4.1.27}$$

and

$$\frac{\partial}{\partial x_3} g_i^{(\gamma)} = 0 \tag{4.1.28}$$

for all β and γ (neglecting the high order terms), by taking partial derivatives of eqns (4.1.18) and (4.1.20) with respect to x_2 and x_3, respectively, we obtain

$$\frac{\partial}{\partial x_2} \dot{w}_i^{(\beta\gamma)} = \frac{\partial}{\partial x_2} \dot{w}_i^{(\hat{\beta}\gamma)} \tag{4.1.29}$$

and

$$\frac{\partial}{\partial x_3} \dot{w}_i^{(\beta\gamma)} = \frac{\partial}{\partial x_3} \dot{w}_i^{(\beta\hat{\gamma})} \tag{4.1.30}$$

Eqns (4.1.29) and (4.1.30) indicate that the state variables of the first order differentiations of the functions $\dot{w}_i^{(\beta\gamma)}$ and $\dot{w}_i^{(\hat{\beta}\gamma)}$ are also equal on the interface. In

order to satisfy the eqns (4.1.29) and (4.1.30) together with eqn (4.1.15), we assumed

$$\dot{w}_i^{(\beta\gamma)} = \dot{w}_i \qquad (4.1.31)$$

This implies that the displacement rate components of the centers for each subcell are the same and also equal to $\dot{w}_i$.

Substitution of the definition of $f_i^{(\beta)}$ and $g_i^{(\gamma)}$ given in eqns (4.1.17) and (4.1.22) into eqns (4.1.25) and (4.1.26), respectively leads to

$$\sum_{\beta=1}^{N_\beta} h_\beta \dot{\phi}_i^{(\beta\gamma)} = h \frac{\partial}{\partial x_2} \dot{w}_i \qquad (4.1.32)$$

$$\sum_{\gamma=1}^{N_\gamma} l_\gamma \dot{\psi}_i^{(\beta\gamma)} = l \frac{\partial}{\partial x_3} \dot{w}_i \qquad (4.1.33)$$

where $h = \sum_{\beta=1}^{N_\beta} h_\beta$ and $l = \sum_{\gamma=1}^{N_\gamma} l_\gamma$ are the length and width of the RVE. So far, the displacement continuity conditions lead to three equations (4.1.31), (4.1.32) and (4.1.33), which will be applied in the following derivation for establishing the strain rate relations between entire RVE and all subcells. In the following, the global strain will be expressed in the function of $\dot{w}_i$, and then the local strain will be determined through eqn (4.1.4) with expressions in terms of $\dot{\phi}_i^{(\beta\gamma)}$ and $\dot{\psi}_i^{(\beta\gamma)}$. As a result, with eqns (4.1.32) and (4.1.33), the relation between the global strain rates and the local strain rates can be established.

The average strain rate of entire RVE is defined as

$$\overline{\eta}_{ij} = \frac{1}{hl} \sum_{\beta=1}^{N_\beta} \sum_{\gamma=1}^{N_\gamma} h_\beta l_\gamma \overline{\eta}_{ij}^{(\beta\gamma)} \qquad (4.1.34)$$

For $i = j = 1$, substituting the first relation in eqn (4.1.4) into eqn (4.1.34) and using eqn (4.1.31), we obtain $\overline{\eta}_{11} = \frac{\partial \dot{w}_1}{\partial x_1}$. For $i = j = 2$, let us multiply eqn (4.1.32) by l_γ

and perform a summation over γ from 1 to N_γ. This mathematical operation leads to

$$\sum_{\beta=1}^{N_\beta} \sum_{\gamma=1}^{N_\gamma} h_\beta l_\gamma \dot{\phi}_2^{(\beta\gamma)} = hl \frac{\partial \dot{w}_2}{\partial x_2} \qquad (4.1.35)$$

Comparing eqn (4.1.35) with eqn (4.1.34) and using the second relation in eqn (4.1.4) gives that $\overline{\eta}_{22} = \frac{\partial \dot{w}_2}{\partial x_2}$. For $i=1$, $j=2$, multiplying eqn (4.1.32) by l_γ and summing over γ yields

$$\sum_{\beta=1}^{N_\beta} \sum_{\gamma=1}^{N_\gamma} h_\beta l_\gamma \dot{\phi}_1^{(\beta\gamma)} = hl \frac{\partial \dot{w}_1}{\partial x_2} \qquad (4.1.36)$$

Substituting the sixth relation in eqn (4.1.4) into eqn (4.1.34) and comparing with eqn (4.1.36), we obtain $\overline{\eta}_{12} = \frac{1}{2}\left(\frac{\partial \dot{w}_2}{\partial x_1} + \frac{\partial \dot{w}_1}{\partial x_2} \right)$. The other three average strain rate components can be derived in the same way. Thus, we can conclude the following relation as

$$\overline{\eta}_{ij} = \frac{1}{2}\left(\frac{\partial \dot{w}_i}{\partial x_j} + \frac{\partial \dot{w}_j}{\partial x_i} \right) \qquad (4.1.37)$$

With eqn (4.1.37) together with eqn (4.1.4), it is possible to express the local variables, $\dot{\phi}_i^{(\beta\gamma)}$ and $\dot{\psi}_i^{(\beta\gamma)}$, and global state variables, $\dot{w}_i$, in eqns (4.1.32) and (4.1.33) in terms of local strain variables $\overline{\eta}_{ij}^{(\beta\gamma)}$ and global strain variable $\overline{\eta}_{ij}$, respectively. For strain variables $\overline{\eta}_{22}$ and $\overline{\eta}_{33}$ we set $i=2$ in eqn (4.1.32) and $i=3$ in eqn (4.1.33). Apparently, with the assistance of eqn (4.1.37) and eqn (4.1.4), the relations were given by

$$\sum_{\beta=1}^{N_\beta} h_\beta \overline{\eta}_{22}^{(\beta\gamma)} = h\overline{\eta}_{22} \qquad \gamma = 1,...,N_\gamma \qquad (4.1.38)$$

$$\sum_{\gamma=1}^{N_\gamma} l_\gamma \overline{\eta}_{33}^{(\beta\gamma)} = l\overline{\eta}_{33} \qquad \beta = 1,...,N_\beta \tag{4.1.39}$$

While, for strain variables, $\overline{\eta}_{12}$ and $\overline{\eta}_{13}$, we added $\sum_{\beta=1}^{N_\beta} h_\beta \left(\dfrac{\partial \dot{w}_2^{(\beta\gamma)}}{\partial x_1} \right)$ to the both sides

of eqn (4.1.32) and also included $\sum_{\gamma=1}^{N_\gamma} l_\gamma \left(\dfrac{\partial \dot{w}_3^{(\beta\gamma)}}{\partial x_1} \right)$ to the both sides of eqn (4.1.33)

with $i = 1$. It is noted that on the right side, the two terms, $\sum_{\beta=1}^{N_\beta} h_\beta \left(\dfrac{\partial \dot{w}_2^{(\beta\gamma)}}{\partial x_1} \right)$ and

$\sum_{\gamma=1}^{N_\gamma} l_\gamma \left(\dfrac{\partial \dot{w}_3^{(\beta\gamma)}}{\partial x_1} \right)$ can be simplified into $h \dfrac{\partial \dot{w}_2}{\partial x_1}$ and $l \dfrac{\partial \dot{w}_3}{\partial x_1}$, respectively. Thus, the

following relation was obtained as

$$\sum_{\beta=1}^{N_\beta} h_\beta \left(\dot{\phi}_1^{(\beta\gamma)} + \frac{\partial \dot{w}_2}{\partial x_1} \right) = 2h\overline{\eta}_{12} \qquad \gamma = 1,...,N_\gamma \tag{4.1.40}$$

$$\sum_{\gamma=1}^{N_\gamma} l_\gamma \left(\dot{\psi}_1^{(\beta\gamma)} + \frac{\partial \dot{w}_3}{\partial x_1} \right) = 2l\overline{\eta}_{13} \qquad \beta = 1,...,N_\beta \tag{4.1.41}$$

By comparing the left hand side of eqns (4.1.40) and (4.1.41) with eqn (4.1.4), we

obtain

$$\sum_{\beta=1}^{N_\beta} h_\beta \overline{\eta}_{12}^{(\beta\gamma)} = h\overline{\eta}_{12} \qquad \gamma = 1,...,N_\gamma \tag{4.1.42}$$

$$\sum_{\gamma=1}^{N_\gamma} l_\gamma \overline{\eta}_{13}^{(\beta\gamma)} = l\overline{\eta}_{13} \qquad \beta = 1,...,N_\beta \tag{4.1.43}$$

For the calculation of components $\overline{\eta}_{11}$, we let the subscript i and j in eqn (4.1.34)

equal to 1. It is noted that $\overline{\eta}_{11}^{(\beta\gamma)}$ is equal to $\partial \dot{w}_1 / \partial x_1$ and can be directly factored

out from the summation at the right hand side of eqn (4.1.34). Therefore the

summation of the remaining terms would become a unity and the relation was derived

as

$$\overline{\eta}_{11}^{(\beta\gamma)} = \overline{\eta}_{11} \qquad (4.1.44)$$

For the $\overline{\eta}_{23}$, eqn (4.1.34) are used directly since it cannot be simplified further with the aid of displacement continuity equations as the other components described before. It is

$$\overline{\eta}_{23} = \frac{1}{h l} \sum_{\beta=1}^{N_\beta} \sum_{\gamma=1}^{N_\gamma} h_\beta l_\gamma \overline{\eta}_{23}^{(\beta\gamma)} \qquad (4.1.45)$$

It is noted that eqns (4.1.38), (4.1.39) together with eqns (4.1.42)-(4.1.45) indicates the relation between the global strain rates and the local strain rates. We rewrite eqns (4.1.38), (4.1.39) and (4.1.42)-(4.1.45) into a matrix form as

$$A_G \eta_s = J \overline{\eta} \qquad (4.1.46)$$

where $\eta_s = \left\{ \overline{\eta}^{(11)}, \quad \overline{\eta}^{(12)}, \quad \cdots \quad \overline{\eta}^{(N_\beta N_\gamma)} \right\}$ represent the collection of the engineering strain rates for all subcells, and $\overline{\eta} = \left\{ \overline{\eta}_{11}, \quad \overline{\eta}_{22}, \quad \overline{\eta}_{33}, \quad 2\overline{\eta}_{23}, \quad 2\overline{\eta}_{13}, \quad 2\overline{\eta}_{12} \right\}$ indicates the overall strain rates of the RVE. In addition, A_G and J contain geometry parameters of the subcells and the RVE, which are $2(N_\beta + N_\gamma) + N_\beta N_\gamma + 1$

by $6 N_\beta N_\gamma$ and $2(N_\beta + N_\gamma) + N_\beta N_\gamma + 1$ by 6 matrices, respectively.

The displacement rate continuity conditions have been applied to establish the relation between the global strain rate and local subcell strain rate so far. In the following, the traction rate continuity conditions will be employed for the derivation. By using the traction rate – stress rate relation

$$\dot{T}_i = \overline{\tau}_{ij} n_j \qquad (4.1.47)$$

and considering the normal vector shown in Fig. 4.3, we obtain the traction rate

continuity conditions as

$$\bar{\tau}_{2j}^{(\beta\gamma)} = \bar{\tau}_{2j}^{(\hat{\beta}\gamma)}$$ (4.1.48)

and

$$\bar{\tau}_{3j}^{(\beta\gamma)} = \bar{\tau}_{3j}^{(\beta\hat{\gamma})}$$ (4.1.49)

where $j = 1, 2, 3$, $\beta = 1, ..., N_\beta$ and $\gamma = 1, ..., N_\gamma$. It can be shown that, due to the symmetry of stress rate tensor and periodic boundary conditions, there are only $5N_\beta N_\gamma - 2(N_\beta + N_\gamma) - 1$ independent equations. These equations are

$$\bar{\tau}_{22}^{(\beta\gamma)} = \bar{\tau}_{22}^{(\hat{\beta}\gamma)} \qquad \beta = 1, ..., N_\beta - 1, \qquad \gamma = 1, ..., N_\gamma \qquad (4.1.50)$$

$$\bar{\tau}_{33}^{(\beta\gamma)} = \bar{\tau}_{33}^{(\beta\hat{\gamma})} \qquad \beta = 1, ..., N_\beta, \qquad \gamma = 1, ..., N_\gamma - 1 \qquad (4.1.51)$$

$$\bar{\tau}_{23}^{(\beta\gamma)} = \bar{\tau}_{23}^{(\hat{\beta}\gamma)} \qquad \beta = 1, ..., N_\beta - 1, \qquad \gamma = 1, ..., N_\gamma \qquad (4.1.52)$$

$$\bar{\tau}_{32}^{(\beta\gamma)} = \bar{\tau}_{32}^{(\beta\hat{\gamma})} \qquad \beta = N_\beta, \qquad \gamma = 1, ..., N_\gamma - 1 \qquad (4.1.53)$$

$$\bar{\tau}_{21}^{(\beta\gamma)} = \bar{\tau}_{21}^{(\hat{\beta}\gamma)} \qquad \beta = 1, ..., N_\beta - 1, \qquad \gamma = 1, ..., N_\gamma \qquad (4.1.54)$$

$$\bar{\tau}_{31}^{(\beta\gamma)} = \bar{\tau}_{31}^{(\beta\hat{\gamma})} \qquad \beta = 1, ..., N_\beta, \qquad \gamma = 1, ..., N_\gamma - 1 \qquad (4.1.55)$$

There are two methods to deal with eqns (4.1.50)-(4.1.55), i.e. a stress rate – total strain rate relation and a stress rate – elastic strain rate relation. The former one for each subcell is written as

$$\bar{\tau}_{ij}^{(\beta\gamma)} = C_{ijkl}^{VP(\beta\gamma)} \bar{\eta}_{kl}^{(\beta\gamma)}$$ (4.1.56)

In eqn (4.1.56), the stiffness matrix $C^{VP(\beta\gamma)}$ contains both elastic and plastic properties and the plastic part can be constructed using eqn (2.2.13). While, the

relation for the other one is given by

$$\overline{\tau}_{ij}^{(\beta\gamma)} = C_{ijkl}^{(\beta\gamma)}\left(\overline{\eta}_{kl}^{(\beta\gamma)} - \overline{\eta}_{kl}^{P(\beta\gamma)}\right) \tag{4.1.57}$$

where $\overline{\eta}_{kl}^{P(\beta\gamma)}$ represents the plastic strain rates of each subcell and the stiffness

matrix $C_{ijkl}^{(\beta\gamma)}$ contains only elastic properties. The constitutive relation given in eqn

(4.1.56) was considered first by substituting the relation into eqns (4.1.50)-(4.1.55),

and then a matrix form based on the traction continuity is established as

$$A_M^{VP}\eta_s = 0 \tag{4.1.58}$$

where η_s has been defined previously and A_M^{VP} is a $5N_\beta N_\gamma - 2(N_\beta + N_\gamma) - 1 \times$

$6N_\beta N_\gamma$ matrix which involves the components of the tensor $C_{ijkl}^{VP(\beta\gamma)}$. Combining

the displacement rate continuity conditions in eqn (4.1.46) and the traction rate

continuity conditions in eqn (4.1.58), we obtain

$$\widetilde{A}^{VP}\eta_s = K\overline{\eta} \tag{4.1.59}$$

where the $6N_\beta N_\gamma \times 6N_\beta N_\gamma$ square matrix $\widetilde{A}^{VP}$ is composed of

$$\widetilde{A}^{VP} = \begin{bmatrix} A_M^{VP} \\ A_G \end{bmatrix} \tag{4.1.60}$$

and the $6N_\beta N_\gamma \times 6$ matrix K is constructed by

$$K = \begin{bmatrix} 0 \\ J \end{bmatrix} \tag{4.1.61}$$

Inverting eqn (4.1.59), the subcell strain rates collection matrix η_s can be expressed

as

$$\eta_s = A^{VP}\overline{\eta} \tag{4.1.62}$$

43

where

$$A^{VP} = \left[\widetilde{A}^{VP} \right]^{-1} K \tag{4.1.63}$$

Note that A^{VP} is a $6N_\beta N_\gamma \times 6$ matrix which can be partitioned into $N_\beta N_\gamma$ entries as follows and each one represents a 6×6 square matrix

$$A^{VP} = \begin{bmatrix} A^{VP(11)} \\ A^{VP(12)} \\ \vdots \\ A^{VP(N_\beta N_\gamma)} \end{bmatrix} \tag{4.1.64}$$

If we want to find the strain rates in some specified subcell, a submatrix form of eqn (4.1.62) by means of eqn (4.1.64) was used, i.e.

$$\overline{\eta}^{(\beta\gamma)} = A^{VP(\beta\gamma)} \overline{\eta} \tag{4.1.65}$$

Substituting eqn (4.1.65) into eqn (4.1.56) yields

$$\overline{\tau}^{(\beta\gamma)} = C^{VP(\beta\gamma)} A^{VP(\beta\gamma)} \overline{\eta} \tag{4.1.66}$$

The average stress rate of entire RVE follows

$$\overline{\tau}_{ij} = \frac{1}{hl} \sum_{\beta=1}^{N_\beta} \sum_{\gamma=1}^{N_\gamma} h_\beta l_\gamma \overline{\tau}_{ij}^{(\beta\gamma)} \tag{4.1.67}$$

Substituting eqn (4.1.66) into eqn (4.1.67), we obtain

$$\overline{\tau} = B^{*VP} \overline{\eta} \tag{4.1.68}$$

where

$$B^{*VP} = \frac{1}{hl} \sum_{\beta=1}^{N_\beta} \sum_{\gamma=1}^{N_\gamma} h_\beta l_\gamma C^{VP(\beta\gamma)} A^{VP(\beta\gamma)} \tag{4.1.69}$$

On the other hand, we can also used eqn (4.1.57) to derive the global stress and strain relations. By substituting eqn (4.1.57) into traction continuity equations, eqns (4.1.50)-(4.1.55), the traction continuity equations can be written in a matrix form as.

44

$$A_M\left(\eta_s - \eta_s^P\right) = 0 \tag{4.1.70}$$

where $\eta_s^p = \left\{\overline{\eta}^{p(11)}, \quad \overline{\eta}^{p(12)}, \quad \cdots \quad \overline{\eta}^{p(N_\beta N_\gamma)}\right\}$ is a collection of plastic strain rates of all subcells and the matrix A_M is somehow related to the stiffness matrix $C_{ijkl}^{(\beta\gamma)}$. Combination of the traction continuity conditions in eqn (4.1.70) with the local strain rate and global strain rate relation given in eqn (4.1.46) yields

$$\widetilde{A}\eta_s - \widetilde{A}^P\eta_s^P = K\overline{\eta} \tag{4.1.71}$$

where

$$\widetilde{A} = \begin{bmatrix} A_M \\ A_G \end{bmatrix} \tag{4.1.72}$$

and

$$\widetilde{A}^P = \begin{bmatrix} A_M \\ 0 \end{bmatrix} \tag{4.1.73}$$

where K matrix is the same with eqn (4.1.61). Through eqn (4.1.71), η_s can be expressed as

$$\eta_s = A\overline{\eta} + A^P\eta_s^P \tag{4.1.74}$$

where

$$A = \widetilde{A}^{-1}K \tag{4.1.75}$$

and

$$A^P = \widetilde{A}^{-1}\widetilde{A}^P \tag{4.1.76}$$

Similar to eqn (4.1.64), the matrices A and A^P can be partitioned into $N_\beta N_\gamma$ elements and each element consists of a 6×6 square matrix, i.e.

$$A = \begin{bmatrix} A^{(11)} \\ A^{(12)} \\ \vdots \\ A^{(N_\beta N_\gamma)} \end{bmatrix} \tag{4.1.77}$$

$$A^P = \begin{bmatrix} A^{P(11)} \\ A^{P(12)} \\ \vdots \\ A^{P(N_\beta N_\gamma)} \end{bmatrix} \tag{4.1.78}$$

Therefore, eqn (4.1.74) can be rewritten to a subcell expression

$$\overline{\eta}^{(\beta\gamma)} = A^{(\beta\gamma)}\overline{\eta} + A^{P(\beta\gamma)}\eta_s^P \tag{4.1.79}$$

Substituting eqn (4.1.79) into eqn (4.1.57) yields

$$\overline{\tau}^{(\beta\gamma)} = C^{(\beta\gamma)}\left(A^{(\beta\gamma)}\overline{\eta} + A^{P(\beta\gamma)}\eta_s^P - \overline{\eta}^{P(\beta\gamma)}\right) \tag{4.1.80}$$

The stress rate – elastic strain rate relation is expected to be

$$\overline{\tau} = B^*\left(\overline{\eta} - \overline{\eta}^P\right) \tag{4.1.81}$$

Substituting eqn (4.1.80) into eqn (4.1.67) and comparing with the eqn (4.1.81), we obtain

$$B^* = \frac{1}{hl}\sum_{\beta=1}^{N_\beta}\sum_{\gamma=1}^{N_\gamma} h_\beta l_\gamma C^{(\beta\gamma)} A^{(\beta\gamma)} \tag{4.1.82}$$

and

$$\overline{\eta}^P = -B^{*-1}\sum_{\beta=1}^{N_\beta}\sum_{\gamma=1}^{N_\gamma} h_\beta l_\gamma C^{(\beta\gamma)}\left(A^{P(\beta\gamma)}\eta_s^P - \overline{\eta}^{P(\beta\gamma)}\right)\!\Big/ hl \tag{4.1.83}$$

Here and now, there are two constitutive equations can be used to characterize the nonlinear behavior of fiber composites. If a tangent modulus composed by elastic and plastic parts can be found, eqn (4.1.68) could be employed in the analysis. Otherwise, eqn (4.1.81) should be applied.

The numerical procedures together with the numerical codes presented in Appendix B were described based on the constitutive equation, eqn (4.1.68). However, the other constitutive law, eqn (4.1.81), was not addressed here.

In the beginning, the overall strain rates $\overline{\eta}$ can be estimated with overall stress rates $\overline{\tau}$ using eqn (4.1.68). It was noted that the overall stress rates $\overline{\tau}$ is evaluated from the time derivative of the given overall stress history. , the total strain rates $\overline{\eta}^{(\beta\gamma)}$ and stress rates $\overline{\tau}^{(\beta\gamma)}$ at some specified subcell $(\beta\gamma)$ can be evaluated through eqns (4.1.65) and (4.1.66), respectively, when the overall strain rates $\overline{\eta}$ was calculated. Furthermore, the $C^{VP(\beta\gamma)}$ matrices of the matrix regions were updated through three parameters model using eqn (2.2.13), while for the $C^{VP(\beta\gamma)}$ matrices of the fiber phase, due to linear elastic property, were not updated with its current stress state. $A^{VP(\beta\gamma)}$ matrices were also updated while $C^{VP(\beta\gamma)}$ matrices changed and a new overall stiffness matrix B^{*VP} for the next time step was composed using eqn (4.1.69). As a result, with generalized method of cells in conjunction with the three parameters model for polymer, the constitutive behavior of fiber composites at different strain rate can be predicted through a numerical iteration. Furthermore, a typical four subcells RVE with square edge packing is shown in Fig. 4.4 and will be widely used in the later simulations.

Chapter 5   Finite Element Analysis

In this chapter, two fiber arrangements, i.e. square edge packing (SEP) array and square diagonal packing (SDP) array, were adopted to investigate the fiber arrangement effects on nonlinear behavior of off-axis fiber composites by using the commercial finite element program ANSYS.   The procedure for finite element analysis will be addressed in this section, and the associated results will be demonstrated in chapter 6 together with the numerical results obtained from the square fiber model and the generalized method of cells to investigate the fiber shape and fiber arrangement effects.

5.1 Finite Element Approach

The methodology about how to establish a finite element model for unidirectional composites subjected to off-axis loadings was basically coming from the paper published by Zhu and Sun [24].   Fig. 5.1 shows a 3-D RVE for the square diagonal packing (SDP) array employed in the finite element analysis, and it is noted that because of symmetry, only one quarter of the RVE was considered. The associated meshes generated automatically from ANSYS mesh generator for the RVE are shown in Figs. 5.2(a)-(b).   The element type used in this study is solid 185. Since the quantities, such as stress, strain and displacement, are independent of the x_1-axis, there is only one single layer of elements established in the fiber direction [24].   It was noted that in Fig 5.1, all stresses were shown in the positive direction, and the relation between the applied stresses in the loading coordinate system and those in the material principle coordinate system is converted through the following translation law

$$\sigma_{11} = \sigma_x \cos^2 \theta$$
$$\sigma_{22} = \sigma_x \sin^2 \theta \qquad (5.1.1)$$
$$\sigma_{12} = -\sigma_x \sin \theta \cos \theta$$

where σ_{ij} are the stresses in the material principle coordinate system, θ is the off-axis angle with respect to the loading direction and σ_x is the applied uniaxial stress. In the FEM analysis, the fiber was assumed to be an orthotropic elastic material with the material properties as shown in Table 2. While, the matrix is assuming to be elastic-plastic obeying the J_2 flow rule. The assumed stress – strain curve of the matrix shown in Fig. 5.3 was selected for FEM analysis. This constitutive curve was imported into ANSYS through the commanding process,

"Main Menu" > "Preprocessor" > "Material Props" > "Material Models" > "Structural" > "Nonlinear" > "Inelastic" > "Rate Independent" > "Isotropic Hardening Plasticity" > "Mises Plasticity" > "Nonlinear". Then, four coefficients of a nonlinear potential function have to be determined to characterize the stress and plastic strain curve. This function is

$$\sigma = k + R_0 \varepsilon^p + R_\infty (1 - e^{-b\varepsilon^p}) \qquad (5.1.2)$$

where k is the yield stress, R_0 and R_∞ are parameters and their physical meanings are shown in the ANSYS user manual [28]. Basically, only the variable b needs to be evaluated by try-and-error manner and the others can be determined directly from the given stress – plastic strain curve. The matrix properties were also listed in Table 2.

After material properties had been given, the boundary conditions were applied on the RVE shown in Fig. 5.1 to satisfy the periodicity condition when the material subjected to off-axis loading.

On $x_1 = 0$ and $x_1 = a$ faces

$$u(0, x_2, x_3) - u(a, x_2, x_3) = \text{constant}$$
$$v(0, x_2, x_3) = v(a, x_2, x_3) \qquad\qquad (5.1.3)$$
$$w(0, x_2, x_3) = w(a, x_2, x_3)$$

where u, v and w respectively to denote the displacements in the x_1, x_2 and x_3 direction. Furthermore, this equation leads $x_1 = 0$ and $x_1 = a$ faces to satisfy periodic boundary conditions. Note that the first relation in eqn (5.1.3) makes it possible for the RVE to undergo an extension in the x_1 direction but not to affects the periodicity.

On $x_2 = 0$ and $x_2 = a$ faces

$$v(x_1, 0, x_3) = 0$$
$$v(x_1, a, x_3) = \text{constant}$$
$$w(a_1, 0, x_3) = w(a_2, 0, x_3) = \text{constant} \qquad (5.1.4)$$
$$w(a_1, a, x_3) = w(a_2, a, x_3) = \text{constant}$$

where a_1 and a_2 represent any two different points with other two identical coordinates, and the first and the second relations of eqn (5.1.4) describe geometric symmetry and periodicity, respectively. Moreover, the third and the fourth relations of eqn (5.1.4) were employed to keep all nodes on faces $x_2 = 0$ or $x_2 = a$ with the same height x_3 without relative motion. It was noted that the third and the forth relations in eqn (5.1.4) were not applied in the current analysis since there was only single layer of element existing in the RVE and these two relations can also be covered by the third relation in eqn (5.1.3).

On $x_3 = 0$ and $x_3 = a$ faces

$$w(x_1, x_2, 0) = 0$$
$$w(x_1, x_2, a) = \text{constant}$$
$$v(a_1, x_2, 0) = v(a_2, x_2, 0) = \text{constant} \qquad (5.1.5)$$
$$v(a_1, x_2, a) = v(a_2, x_2, a) = \text{constant}$$

which implies similar meanings as eqn (5.1.4) and the third and the forth relations in eqn (5.1.5) are involved by the second relation in eqn (5.1.3). To avoid the rigid body translation, an additional displacement constraint was imposed in the x_1

direction, i.e.

$$u(0,0,0) = 0 \tag{5.1.6}$$

In order to implement the boundary conditions, three ANSYS options "CP", "CE" and "D" were applied. "CP" option lets a set of nodes possess the same degree of freedom. Therefore, the second and the third relations in eqn (5.1.3) and the second relation in eqns (5.1.4) and (5.1.5) are established by using this command. "CE" option lets the degree of freedoms of a set of nodes obey desired constraint equations. The first relation in eqn (5.1.3) can be expanded as

$$u_1\big|_{x_1=0} - u_1\big|_{x_1=a} = u_2\big|_{x_1=0} - u_2\big|_{x_1=a} = \ldots\ldots = u_N\big|_{x_1=0} - u_N\big|_{x_1=a} \tag{5.1.7}$$

where the subscript 1 to N denotes N sets of corresponding nodes with the same x_2 and x_3 coordinates respectively on $x_1 = 0$ and $x_1 = a$ faces and eqn (5.1.7) can be further decomposed as

$$
\begin{aligned}
u_1\big|_{x_1=0} - u_1\big|_{x_1=a} &= u_2\big|_{x_1=0} - u_2\big|_{x_1=a} \\
u_2\big|_{x_1=0} - u_2\big|_{x_1=a} &= u_3\big|_{x_1=0} - u_3\big|_{x_1=a} \\
&\vdots \\
u_{N-1}\big|_{x_1=0} - u_{N-1}\big|_{x_1=a} &= u_N\big|_{x_1=0} - u_N\big|_{x_1=a}
\end{aligned}
\tag{5.1.8}
$$

Obviously, there are N-1 independent constraint equations existing in the RVE and can be built up using "CE" command. The latest option "D" can assign a fixed displacement value on desired nodes, so the displacements equal to zero in the boundary conditions can be carried out. After the boundary conditions were appropriately defined, the stresses evaluated from eqn (5.1.1) at material principle coordinate system were multiplied by the loading surface area to obtain external forces. Shear forces on $x_1 = 0$ and $x_2 = a$ faces and all normal forces were placed at single node on associated loading surface since the boundary conditions had been appropriately defined. But the shear forces at $x_2 = 0$ and $x_2 = a$ must be

distributed to every node through the element shape function provided by user manual [29] to ensure the nodal force being consistent with the distributed loading. All forces were divided into several tiny steps and implemented gradually by using the following commands

"Main Menu" > "Solution" > "Analysis Type" > "Sol'n Controls"

By collecting element strains at each load step, the average strain of the RVE can be evaluated by taking an average from all element strains, i.e.

$$\bar{\varepsilon} = \frac{1}{V} \sum_{i=1}^{M} \varepsilon_i V_i \qquad (5.1.9)$$

where M is the total number of elements, $\bar{\varepsilon}$ and ε_i are respectively to average strain and element strain, and V and V_i represent the volume of RVE and the element volume, respectively.

Chapter 6   Results and Discussion

In this chapter, thermal stress effect on off-axis fiber composites was investigated by using square fiber model (SFM) and generalized method of cells (GMC). Then, the fiber shape effect on square edge packing (SEP) array was studied through GMC and modified SFM. Moreover, the investigation of fiber arrangement effect was performed by using modified SFM, GMC, and finite element method (FEM), respectively. Finally, the model predictions using SFM and GMC were compared with the experimental results.

6.1 Thermal Stress Effect

During the curing process of polymeric composites, because of distinct difference of coefficient of thermal expansion (CTE) between the fiber and the matrix, the thermal residual stresses usually were generated in the fiber and matrix. Based on the thermal elasticity, the thermal residual stress in the fiber and the matrix can be calculated in terms of Young's modulus (E), coefficient of thermal expansion (α), and the area of the cross section (A) as shown in Fig. 6.1. It is noted that for the calculation of the thermal residual stress, the conventional fiber composite was simplified as the solid containing fiber and matrix phases as shown in the Fig. 6.1(a). Since during the curing process, the fiber and matrix interface are well bounded and have to satisfy the displacement continuity in the x direction as shown in Fig 6.1(b), from the thermal elasticity, the thermal residual stresses in the fiber and matrix can be expressed as

$$
\begin{cases}
\sigma_m = E_m \left(\alpha_m \Delta T - \dfrac{\delta}{l} \right) \\[2ex]
\sigma_f = -E_f \left(\dfrac{\delta}{l} - \alpha_f \Delta T \right)
\end{cases}
\tag{6.1.1}
$$

where ΔT is the temperature change in the cooling process, l is the specimen length in the fiber direction, δ is the displacement of the specimen when it attains to the equilibrium position. E and α denote the Young's modulus and coefficient of thermal expansion of the specimen. The subscripts, i.e. m and f, in eqn (6.1.1) represent matrix and fiber, respectively. In eqn (6.1.1), it was assumed that the stress is free in the heating process and the thermal stress would be produced only in the cooling process. Furthermore, during the cooling, there is no mechanical loading applied, and the global stress states should be zero. Thus,

$$\sigma_m A_m + \sigma_f A_f = 0 \qquad (6.1.2)$$

where A_f and A_m are the cross section of the fiber and the matrix. With eqn (6.1.2), the displacement δ can be expressed as

$$\delta = \frac{\left(E_f \alpha_f A_f + E_m \alpha_m A_m\right) l \Delta T}{E_f A_f + E_f A_f} \qquad (6.1.3)$$

The thermal residual stress could be estimated from eqns (6.1.1) and (6.1.3), and then employed into square fiber model (SFM) and generalized method of cells (GMC) to investigate the thermal stress effect on the mechanical behavior of off-axis fiber composites. For GMC, a four subcell RVE with $N_\beta = N_r = 2$ as shown in Fig. 4.4 was adopted to perform this study while the RVE of SFM was demonstrated in Fig. 3.2. Here, we only consider the residual stress component in the fiber extension direction, i.e. σ_{11}. Thus, the thermal stress calculated from eqn (6.1.1) was imposed as an initial stress state on all matrix regions of SFM and GMC. It was noted that in the fiber region of SFM and GMC, it was assumed to be stress free initially. All analyses were performed using the Matlab code of SFM and GMC listed in Appendix

A and B respectively, and the initial stress value was implemented by using the **sigam** and **sigb** for SFM and **substress** for GMC in the code**.** The associated matrix and fiber properties employed in the simulation were listed in Tables 1 and 2, respectively, and the fiber volume fraction used in the simulation was 60%. The numerical results of the stress-strain curves for $30°$ and $90°$ specimens with the thermal stress simulated by SFM and GMC were shown, respectively in Figs. 6.2(a)-(b) and Figs. 6.3(a)-(b). For comparison, the results without including the thermal stress were also included in the Figures. It is interesting to note that the fiber composites with thermal stress exhibit stiffer behaviors than those without thermal stress for all fiber orientations as shown in Figs. 6.2-6.3. This result seems to be different from out intuition. However, the reason is due to that the presence of thermal stress σ_{11} in the matrix phase would prevent the plastic deformation in the other directions resulting in the small uniaxial strain when the composites is subjected to off-axis loading. By taking $90°$ specimens as an example (see Fig 6.2(b) and Fig. 6.3(b)), apparently, it shows that the transverse deformation ε_{22} for the composites with thermal stress is less than that without thermal stress. Thus, it was suggested that the off-axis composites would become stiffer if the thermal residual stresses is involved in the analysis.

6.2 Discussion of Fiber Shape and Fiber Arrangement Effect

6.2.1 Fiber Shape Effect

Two fiber shapes (square fiber and round fiber) embedded in the square edge packing (SEP) of RVE were discussed using the square fiber model (SFM) and generalized method of cells (GMC). When the square shape fiber was considered, the typical SFM and GMC shown in Fig. 3.2 and Fig.4.4 were adopted to perform the simulations. On the other hand, the modified GMC [20] with 26×26 subcells as

shown in Fig. 6.4 and the modified SFM model with 50 subcells in fibrous region A

as shown in Figs. 6.5 were employed to describe the RVEs containing the round fiber.

In the study, the fiber properties are given in Table 2 with fiber volume fraction 60 %

while the plastic properties of the matrix, with 3.4 GPa Young's modulus and 0.37

Poisson's ratio, were characterized using power law (see eqn 2.2.8) with

$A = 6.42 \times 10^{-11}$ and $n = 4.11$. All simulation results were demonstrated in Figs.

6.6 (a)-(d). According to the results, it is found that, for all off-axis angles, the

round fiber and square fiber exhibit the similar results if the micromechanical models

applied are the same. Therefore, the round fiber can be replaced with the square

fiber for saving CPU cost since a large number of subcells are required for modeling

the RVE with round fiber.

6.2.2 Fiber Arrangement Effect

The stress - strain curves of the off-axis composites with two different fiber

arrangements, i.e. square edge packing (SEP) and square diagonal packing (SDP),

were generated using finite element method (FEM) together with modified square

fiber model (SFM) and generalized method of cells (GMC). It is noted that to be

consistent with the all three models, i.e., FEM, modified SFM and GMC, the RVEs

with round fiber were taken into account, although lots of computation time is

required. The approach regarding the FEM analysis was discussed in chapter 5.

For GMC and SFM, the RVEs with the square edge packing were presented early in

Figs. 6.4 and 6.5, respectively. Nevertheless, for the square diagonal packing, the

RVE used for GMC was divided into 20×20 subcells as shown in Fig. 6.7 and the

RVE used for modified SFM was divided into three regions, i.e., two A regions and

one B region, as shown in Fig. 6.8 where thirty subcells is contained in region A and

twenty subcells were included in region B. The fiber properties were given in Table

2 with 60 % volume fraction while the matrix was assumed to follow the constitutive curve shown in Fig. 5.3 which was curve-fitted by a power law (eqn 2.2.8) with the coefficients $A = 6.42 \times 10^{-14}$ and $n = 3.9$. It is noted that the above ingredient properties were the same as those used in the FEM analysis.

Figs. 6.9(a)-(d) demonstrates the stress and strain curves obtained from the RVE with SEP and SDP fiber arrangement using modified SFM and GMC, respectively. It was shown that the SEP fiber arrangement exhibits stiffer material behavior the SDP arrangement for all off-axis angles. Moreover, at SDP fiber arrangement, the constitutive behaviors calculated from GMC and modified SFM are almost the same no matter the fiber orientation. However, for the SEP fiber arrangement, when the fiber orientation is small, the results obtained from GMC and modified SFM are similar, while at large fiber orientation, the GMC model provides stiffer material properties than the modified SFM. The numerical simulations of the RVE with SEP and SDP fiber arrangements using FEM were illustrated in Figs.6.10(a)-(d). In contrast to modified SFM and GMC, there is no significant difference found in the FEM analysis between SEP and SDP fiber array when the off-axis angle is small. When the off-axis angle becomes larger, the corresponding discrepancy is getting significant. The comparisons of the predictions using modified SFM, GMC and FEM for the RVE with SEP or SDP fiber array were shown in Figs. 6.11(a)-(h). It can be seen that no matter in SEP case or in SDP case, FEM analysis always shows stiffer material properties rather than GMC and modified SFM.

6.3 Comparing with Experimental Data

In order to verify the accuracy of the constitutive behaviors of fiber composites predicted using square fiber model (SFM) and generalized method of cells (GMC), off-axis composites with fiber orientations of 15, 30, 45 and 60 degrees were

tested at strain rate ranges from 10^{-4} to 550/s. The experimental data of the PPG graphite/epoxy composites can be found in the reference [30], and the associated material properties of the HTA-12k graphite fiber and the epoxy were listed in Table 1 where the fiber was assumed to be transverse isotropic material [31]. It was noted that in the fiber phase, since only E_1 was provided from the manufacture, the other properties were evaluated by the trial-and-error method to accomplish the experimental elastic constants of the off-axis composites, if possible. Moreover, the fiber volume fraction of the PPG graphite/epoxy composites was also assumed to be 69% in order to satisfy the elastic deformation of the composites. Nevertheless, with this fiber volume fraction together with ingredient properties, it was found that the model predictions obtained either from SEP fiber array or SDP fiber array are softer than the experimental data. In order to properly characterize the experimental data, the RVE with SEP was selected in the analysis, since the RVE with SEP is stiffer than that with SDP and closer to the current experimental data. From the forgoing investigation, it was suggested that round fiber included in the RVE provide the similar results to those obtained from the RVE with the square one. Thus, to simplify the analytical process, the square fiber was selected and embedded in the RVE for the micromechanical analysis. In addition, it should be mentioned that the plastic deformation described by the FEM analysis is quite small as compared to the experimental data such that it is not suitable for modeling the current material system. In view of the forgoing, it was suggested the RVE with the square fiber in the square edge packing was adopted in the present predictions. The model predictions based on SFM and GMC were respectively shown in Figs. 6.12(a)-(d) and Figs. 6.13(a)-(d) together with the experimental data. It was found that the stress and strain curves is quite sensitive to the strain rates and moreover, as the strain rate increased, the material becomes stiff. Comparison of the model predictions with the experimental

data reveals that the micromechanical model together with the viscoplasticity model for the matrix is capable of predicting the nonlinear rate dependent behaviors of off-axis specimens at strain rate up to 550/s, although there is still discrepancy between the experimental data and model predictions.　Based on Figs 6.12 and 6.13, it seems that the GMC model provides better predictions than the SFM when compared to the experimental data of the current graphite/epoxy system.

Chapter 7   Conclusion

The thermal stress effect, fiber shape effect and fiber arrangement effect on nonlinear rate dependent behavior of fiber composites was investigated using square fiber model, generalized method of cells and finite element analysis.   It was shown that with the presence of thermal residual stress, the fiber composites become stiffer than those without thermal stress.   Regarding the fiber arrangement effects, the RVE with square edge packing (SEP) array is stiffer than that with square diagonal packing (SDP).   In addition, the RVEs containing either round fiber or square fiber result in the similar material behavior of fiber composites.

In order to validate the model predictions, the experimental results of the graphite/epoxy composites tested at various strain rates were employed for the comparison.   The model predictions were obtained from the SFM and GMC analysis on the RVE with SEP fiber array containing the transverse isotropic fiber and elastic-viscoplastic matrix.   The viscoplastic behaviors of epoxy resin were described using a three parameters viscoplasticity model written in the form of power law.   Comparing the model predictions and experimental data reveals that the GMC is better than the SFM to predict the nonlinear rate sensitivity of off-axis specimens at strain rate up to 550/s if the current material properties were applied.   Comparison of model predictions obtained from GMC and SFM analysis with the experimental results revealed that the micromechanical approaches are capable of predicting the nonlinear rate sensitivity of off-axis specimens although there are still distinctions between the model and the experimental results.

Reference

[1] Sun, C. T. and Chen, J. L. 1989 "A Simple Flow Rule for Characterizing Nonlinear Behavior of Fiber Composites," *Journal of Composite Materials*, Vol. 23, No. 10, pp. 1009-1020.

[2] Gates, T. S. and Sun, C. T. 1991 "Elastic/Viscoplastic Constitutive Model for Fiber Reinforced Thermoplastic Composites," *AIAA Journal*, Vol. 29, No. 3, pp. 457-463.

[3] Eisenberg, M. A. and Yen, C. F. 1981 "Theory of Multiaxial Anisotropic Viscoplasticity," *ASME Journal of Applied Mechanics*, Vol. 48, No.2, pp. 276-284.

[4] Yoon, K. J. and Sun, C. T. 1991 "Characterization of Elastic-Viscoplastic Properties of an AS4/PEEK Thermoplastic Composite," *Journal of Composite Materials*, Vol. 25, No. 10, pp. 1277-1296.

[5] Stouffer, D. C. and Dame, L. T. 1996 *Inelastic Deformation of Metals/Models, Mechanical Properies, and Metallurgy*, John Wiley & Sons, Inc., New York.

[6] Weeks, C. A. and Sun, C. T. 1998 "Modeling Non-Linear Rate-Dependent Behavior in Fiber-Reinforced Composites," *Composites Science and Technology*, Vol. 58, No. 3-4, pp. 603-611.

[7] Meyers, M. A. 1994 *Dynamic Behavior of Materials*, John Wiley & Sons, New York.

[8] Thiruppukuzhi, S. V. and Sun, C. T. 2001 "Models for the Strain-Rate-Dependent Behavior of Polymer Composites," *Composites Science and Technology*, Vol. 61, No. 1, pp. 1-12.

[9] Eshelby, J. D. 1957 "The Determination of the Elastic Field of an Ellipsoidal Inclusion, and Related Problems," *Proceedings of the Royal Society of London*, A241, No. 1226, pp. 376-396.

[10] Mori, T. and Tanaka, K. 1973 "Average Stress in Matrix and Average Elastic Energy of Materials with Misfitting Inclusions," *Acta Metallurgica*, Vol. 21, No. 5, pp. 571-574.

[11] Benveniste, Y. 1987 "A New Approach to the Application of Mori-Tanaka Theory in Composite Materials," *Mechanics of Materials*, Vol. 6, No. 2, pp. 147-157.

[12] Sun, C. T. and Chen, J. L. 1991 "A Micromechanical Model for Plastic Behavior of Fibrous Composites," *Composite Science and Technology*, Vol. 40, No. 2, pp. 115-129.

[13] Aboudi, J. 1982 "A Continuum Theory for Fiber-Reinforced Elastic-Viscoplastic Composites," *International Journal of Engineering Science*, Vol. 20, No. 5, pp. 605-621.

[14] Aboudi, J. 1991 *Mechanics of Composite Materials – A Unified Micromechanical Approach*, Elsevier Science Publishing Company, Inc., New York, pp. 35-53.

[15] Paley, M. and Aboudi, J. 1992 "Micromechanical Analysis of Composites by the Generalized Cells Model," *Mechanics of Materials*, Vol. 14, No. 2, pp. 127-139.

[16] Mura, T. 1987 *Micromechanics of Defects in Solids*, Kluwer Academic, Dordrecht.

[17] Pettermann, H. E. and Plankensteiner, A. F. and Bohm, H. J. and Rammerstorfer, F. G. 1999 "A Thermo-Elastic-Plastic Constitutive Law for Inhomogeneous Materials Based on an Incremental Mori-Tanaka Approach," *Computers & Structures*, Vol. 71, pp. 197-214.

[18] Goldberg, R. K. and Stouffer, D. C. 2002 "Strain Rate Dependent Analysis of a Polymer Matrix Composite Utilizing a Micromechanics Approach," *Journal of Composite Materials*, Vol. 36, No. 7, pp. 773-793.

[19] Orozco, C. E. 1997 "Computational Aspects of Modeling Complex Microstructure Composites Using GMC," *Composites Part B*, Vol. 28, No. 1-2, pp. 167-175.

[20] Pindera, M. J. and Bednarcyk, B. A. 1999 "An Efficient Implementation of the Generalized Method of Cells for Unidirectional, Multi-Phased Composites with

Complex Microstructures," *Composites: Part B*, Vol. 30, No. 1, pp. 87-105.

[21] Orozco, C. E. and Pindera, M. J. 1999 "Plastic Analysis of Complex Microstructure Composites Using the Generalized Method of Cells," *AIAA Journal*, Vol. 37, No. 4, pp. 482-488.

[22] Ogihara, S., Kobayashi, S. and Reifsnider, K. L. 2003 "Characterization of Nonlinear Behavior of Carbon/Epoxy Unidirectional and Angle-Ply Laminates," *Advanced Composite Materials*, Vol. 11, No. 3, pp. 239-254.

[23] Kawai, M., Masuko, Y., Kawase, Y. and Negishi, R. 2001 "Micromechanical Analysis of the Off Axis Rate-Dependent Inelastic Behavior of Unidirectional AS4/PEEK at High Temperature," *International Journal of Mechanical Sciences*, Vol. 43, No. 9, pp. 2069-2090.

[24] Zhu, C. and Sun, C. T. 2003 "Micromechanical Modeling of Fiber Composites under Off-Axis Loading," *Journal of Thermoplastic Composite Materials*, Vol. 16, No. 4, pp. 333-344.

[25] Tuttle, M. E. 1989 "Fundamental Strain-Gage Technology," *Manual on Experiment Methods for Mechanical Testing of Composites*, edited by Pendleton, R. L. and Tuttle, M. E., Society for Experimental Mechanics, Bethel, CT.

[26] 1987 "Measurement of Thermal Expansion Coefficient Using Strain Gages," Micro-Measurement Technical Note TN-513, Measurement Group, Inc.

[27] Scalea, F. L. D. 1998 "Measurement of Thermal Expansion Coefficient of Composites Using Strain Gages," *Experimental Mechanics*, Vol. 38, No. 4, pp. 233-241.

[28] ANSYS Element Reference. 000855. Eighth Edition. SAS IP, Inc. 1997.

[29] ANSYS Theory Reference. 000855. Eighth Edition. SAS IP, Inc. 1997.

[30] 郭濬清, "應變率對纖維複合材料側向抗壓強度影響之探討," *國立交通大學碩士論文*, 2005.

[31] Tsai, S. W. and Hahn, H. T. 1980 *Introduction to Composite Materials*, Technomic Publishing Co., Westport, CT, USA.

Appendix

A. A MATLAB Code for Square Fiber Model

Input Symbol List

Ef1, Ef2, nuf12, Gf12, volf – Young's modulus 1 (and 2), Poisson's ratio ,shear
modulus and volume fraction of the fiber.

Em, num, Gm – Young's modulus, Poisson's ratio and shear modulus of the matrix.

pn, xi, pm – denote n, χ and m in the three parameters model.

time – A matrix to store the total loading time.   The Row represents different strain
rates while the column denotes various off-axis angles.

ratetype – An index to point what strain rate was in calculation.

angle, Nstep – off-axis angle and total steps of loop.

Matrix and Scalar Symbol List

---

saf – Fiber compliance matrix.

eSm – Matrix compliance matrix.

v1, v2 – Volume fraction of region AF and AM relative to region A.

Tsig, Teps – Transformation matrix relatively for stress and strain to translate
between loading coordinates and material principle axis.

sigma, sigb – Current stress states in region AM and B, respectively.

Tstress, Tstrain – Overall stress and strain in the loading coordinate system.

depsam, depsaf – Total strain rates in region AM and AF.

dpepsam, dpepsb – Plastic strain rates in region AM and B.

dsigaf, dsigam – Stress rate in region AF and AM.

t, sigrate – Current time and associated stress rate.

dsig, dsig1 – Applied stress rate in the material principle axis and loading coordinate
system, respectively.

efsig, efeps – Effective stress and effective plastic strain rate.

pSm, sa, sb, ca, cb, c, s - $\left[S^p\right]$, $\left[S^A\right]$, $\left[S^B\right]$, $\left[C^A\right]$, $\left[C^B\right]$, $[C]$, $[S]$

deps, deps1 – Strain rate associated to applied stress rate in the material coordinate
system and loading coordinate system.

Note: Subroutine "stressrate(t,ratetype,angle/15)", which involves stress rate –
time polynomial equation from curve-fitting of experimental data, have three input
parameters to output corresponding stress rate at each time increment.   The
subroutine can be designed by users and was not demonstrated here.

Code

```
% Square Fiber Model Combined with Three Parameters Model
clear all
%----------------Material Properties-------------------
% Fiber
Ef1=235000;          % E11 of fiber
Ef2=18000;           % E22 of fier
nuf12=0.2;           % Poisson's ratio 12 of fiber
Gf12=35000;          % Shear modulus 12 of fiber
volf=0.69;           % fiber volume fraction
% Matrix
Em=3400;             % Young's modulus of the matrix
num=0.373;           % Poisson's ratio of the matrix
Gm=Em/(2*(1+num));   % Shear modulus of the matrix
pn=5.62;             % Coefficient n in the 3 parameters model
xi=1.23e-14;         % Coefficient xi in the 3 parameters model
pm=-0.168;           % Coefficient m in the 3 parameters model
%-------------------------------------------------------
% Loop & angle
time=[208 694 695 675 380;
      1.83 7.25 10.9 6.9 4.54;
      0.0323 0.0725 0.0981 0.0801 0.05;
      5.1e-5 7.07e-5 7.84e-5 8.65e-5 6.4e-5];
ratetype=3;
angle=30;                           % Off-axis angle
if angle == 90
    totime=time(ratetype,5);
else
    totime=time(ratetype,angle/15);
end
%totime=time(ratetype,2);
Nstep=450;                          % Total time steps
dtime=totime/Nstep;                 % Associated time increment
rad=angle/180*pi;


%-------------------------------------------------------
saf=[1/Ef1 -nuf12/Ef1 0; -nuf12/Ef1 1/Ef2 0; 0 0 1/Gf12]; % fiber compliance matrix
eSm=[1/Em -num/Em 0; -num/Em 1/Em 0; 0 0 1/Gm]; % matrix compliance matrix (elastic)
```

```matlab
v1=sqrt(volf);    % volume fraction of AF with respective to region A
v2=1-v1;          % volume fraction of AM with respective to region A


% Transformation matrix to translate stress
Tsig=[cos(rad)^2 sin(rad)^2 2*cos(rad)*sin(rad);...
      sin(rad)^2 cos(rad)^2 -2*cos(rad)*sin(rad);...
      -cos(rad)*sin(rad) cos(rad)*sin(rad) cos(rad)^2-sin(rad)^2];


% Transformation matrix to translate strain
Teps=[cos(rad)^2 sin(rad)^2 -cos(rad)*sin(rad);...
      sin(rad)^2 cos(rad)^2 cos(rad)*sin(rad);...
      2*cos(rad)*sin(rad) -2*cos(rad)*sin(rad) cos(rad)^2-sin(rad)^2];


% -------------------matrix pre-setup-----------------
sigam=zeros(3,1);
sigb=zeros(3,1);
Tstress=zeros(Nstep+1,1);
Tstrain=zeros(Nstep+1,1);
depsam=zeros(3,1);
depsaf=zeros(3,1);
dpepsam=zeros(3,1);
dpepsb=zeros(3,1);
depsb=zeros(3,1);
dsigaf=zeros(3,1);
dsigam=zeros(3,1);
%-----------------------Main Loop---------------------
for n=1:Nstep;
   t=n*dtime;                          % current time
   sigrate=strainrate(t,ratetype,angle/15);
   dsig1=[sigrate; 0; 0];              % x-y stress rate
   Tstress(n+1,1)=Tstress(n,1)+dsig1(1,1)*dtime; % Overall stress
   dsig=Tsig*dsig1;                    % 1-2 stress rate
   efeps=2/3*sqrt(3*(dpepsam(1)^2+dpepsam(2)^2+dpepsam(1)*dpepsam(2)+dpepsam(3)^2/
   4));
   if n = = 1
      A=0;
   else
      A=xi*(efeps)^pm;
```

```
end


s1=1/3*(2*sigam(1,1)-sigam(2,1));
s2=1/3*(-sigam(1,1)+2*sigam(2,1));
s3=2*sigam(3,1);
efsig=sqrt((sigam(1,1)+sigam(2,1))^2-3*(sigam(1,1)*sigam(2,1)-sigam(3,1)^2));
st=[2*(sigam(1,1)+sigam(2,1))-3*sigam(2,1)
    2*(sigam(1,1)+sigam(2,1))-3*sigam(1,1)
    6*sigam(3,1)];
pSm=3/4*A*pn*efsig^(pn-3)*[s1*st; s2*st; s3*st];
sam=eSm+pSm;


% sm matrix
b1=(v1*Ef1*sam(1,1)+v2)^-1;
b2=-v1*(Ef1*sam(1,2)+nuf12)*(v1*Ef1*sam(1,1)+v2)^-1;
b3=-v1*Ef1*sam(1,3)*(v1*Ef1*sam(1,1)+v2)^-1;
a1=(1-v2*b1)/v1;
a2=-v2*b2/v1;
a3=-v2*b3/v1;
sa(1,1)=a1/Ef1;
sa(1,2)=a2/Ef1-nuf12/Ef1;
sa(1,3)=a3/Ef1;
sa(2,1)=sa(1,2);
sa(2,2)=v1*(1/Ef2-nuf12*a2/Ef1)+v2*(b2*sam(2,1)+sam(2,2));
sa(2,3)=-v1*a3*nuf12/Ef1+v2*(b3*sam(2,1)+sam(2,3));
sa(3,1)=sa(1,3);
sa(3,2)=sa(2,3);
sa(3,3)=v1/Gf12+v2*(b3*sam(3,1)+sam(3,3));
ca=inv(sa);


% CB matrix
efeps=2/3*sqrt(3*(dpepsb(1)^2+dpepsb(2)^2+dpepsb(1)*dpepsb(2)+dpepsb(3)^2/4));
if n = = 1
    A=0;
else
    A=xi*(efeps)^pm;
end
```

```
s1=1/3*(2*sigb(1,1)-sigb(2,1));
s2=1/3*(-sigb(1,1)+2*sigb(2,1));
s3=2*sigb(3,1);
efsig=sqrt((sigb(1,1)+sigb(2,1))^2-3*(sigb(1,1)*sigb(2,1)-sigb(3,1)^2));
st=[2*(sigb(1,1)+sigb(2,1))-3*sigb(2,1)
    2*(sigb(1,1)+sigb(2,1))-3*sigb(1,1)
    6*sigb(3,1)];
pSm=3/4*A*pn*efsig^(pn-3)*[s1*st; s2*st; s3*st];
sb=eSm+pSm;
cb=inv(sb);
c=v1*ca+v2*cb;
s=inv(c);


deps=s*dsig;     % total strain rate
depsa=deps;      % total strain rate of region A
depsb=deps;      % total strain rate of region B
dsiga=ca*depsa; % stress rate of region A
dsigb=cb*depsb; % stress rate of region B
dsigaf(2:3,1)=dsiga(2:3,1);
dsigam(2:3,1)=dsiga(2:3,1);
depsaf(1,1)=depsa(1,1);
dsigaf(1,1)=depsaf(1,1)*Ef1+nuf12*dsigaf(2,1);
depsaf(2,1)=saf(2,:)*dsigaf;
depsaf(3,1)=saf(3,:)*dsigaf;
depsam(1,1)=depsa(1,1);
depsam(2,1)=(depsa(2,1)-v1*depsaf(2,1))/v2;
depsam(3,1)=(depsa(3,1)-v1*depsaf(3,1))/v2;
dsigam(1,1)=(dsiga(1,1)-v1*dsigaf(1,1))/v2;


dpepsam=depsam-Sm*dsigam;
dpepsb=depsb-Sm*dsigb;
deps1=Teps*deps;
Tstrain(n+1,1)=Tstrain(n,1)+deps1(1,1)*dtime;
sigam=sigam+dsigam*dtime;
sigb=sigb+dsigb*dtime;
end
```
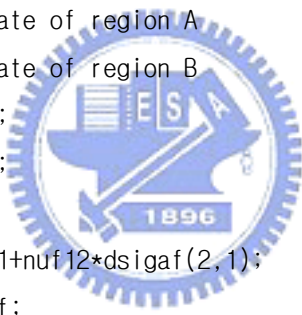
B. A MATLAB Code for Generalized Method of Cells

Since some symbols in the GMC code are a repetition of those appearing in the SFM code, only differences are listed. This code is addressed on four regions RVE with fiber phase at $\beta = \gamma = 1$.

Input Symbol List

---

h, l – The height and the width of the RVE.

Nb, Nr - N_β, N_γ

Nfiber – Denote how many subcells are occupied by the fiber phase.

regionf – A matrix to store what cells are occupied by fibers.   The fibrous subcell $(\beta\gamma)$ must be translated to a re-defined fiber number by using the equation

$N = (\beta - 1)N_\gamma + \gamma$ and N was arranged in the regionf matrix.

Matrix and Scalar Symbol List

---

bb, hh – The length of subcell $\begin{matrix} \beta = 1 \\ \gamma = 1 \end{matrix}$ and $\begin{matrix} \beta = 1 \\ \gamma = 2 \end{matrix}$ in the x_2 direction.

hb, hr – Two matrix to store the geometry information bb and hh.

Sm – Compliance matrix including plastic part.

AG, J, AVPM, AVP, K, AtVP, Bvp - $[A_G]$, $[J]$, $[A_M^{VP}]$, $[A^{VP}]$, $[K]$, $[\tilde{A}^{VP}]$, B^{*VP}

substress – A matrix to store current stress state of all subcells.

sigma – A transition matrix to get current stress state for specified subcell from substress matrix.

Cs – Stiffness matrix of all subcells.

Sf, Cf – Compliance matrix and stiffness matrix of the fiber.

eSm, eCm – Elastic compliance matrix and elastic stiffness matrix of the matrix.

index, index2 – Indexes to point out which subcell should be under calculation.

betahat, gamahat - $\hat{\beta}$ and $\hat{\gamma}$.

subteps, subsigrate – Strain rate and stress rate of specified subcell.

subeeps, subeps – Elastic strain rate and plastic strain rate of specified subcell.

Code

```
clear all
% Material Properties (transverse isotropic fiber + isotropic matrix)
Ef1=235000;                % Young's modulus 11 of the fiber
Ef2=18000;                 % Young's modulus 22 of the fiber
Ef3=Ef2;                   % Young's modulus 33 of the fiber
nuf12=0.2;                 % Poisson's ratio 12 of the fiber
nuf13=0.2;                 % Poisson's ratio 13 of the fiber
nuf23=0.25;                % Poisson's ratio 23 of the fiber
Gf12=35000;                % Shear modulus 12 of the fiber
Gf13=Gf12;                 % Shear modulus 13 of the fiber
Gf23=Ef2/(2*(1+nuf23));    % Shear modulus 23 of the fiber
Em=3400;                   % Young's modulus of the matrix
num=0.373;                 % Poisson's ratio of the matrix
Gm=Em/(2*(1+num));         % Shear modulus of the matrix


% Coefficients of 3 parameter model
pn=5.62;                   % Coefficient n in the 3 parameters model
xi=1.23e-14;               % Coefficient xi in the 3 parameters model
pm=-0.168;                 % Coefficient m in the 3 parameters model


% region dimension & cell situation
h=1;                       % the length of the RVE
l=1;                       % the width of the RVE
volf=0.69;                 % fiber volume fraction
Nb=2;
Nr=2;
bb=sqrt(volf);
hh=1-bb;
hb=[bb hh];
hr=hb;
Nfiber=1;
regionf=[1];


% Loop & angle
time=[208 694 695 675 380;
    1.83 7.25 10.9 6.9 4.54;
    0.0323 0.0725 0.0981 0.0801 0.05;
```

```matlab
    5.1e-5 7.07e-5 7.84e-5 8.65e-5 6.4e-5];
ratetype=3;
angle=60;                                   % Off-axis angle
if angle == 90
    totime=time(ratetype,5);
else
    totime=time(ratetype,angle/15);
end
Nstep=500;                                  % Total time steps
dtime=totime/Nstep;                         % Time increment
rad=angle/180*pi;


% matrix pre-setup
Sm=zeros(6,6);
AG=zeros(2*(Nb+Nr)+Nb*Nr+1,6*Nb*Nr);
J=zeros(2*(Nb+Nr)+Nb*Nr+1,6);
substress=zeros(6*Nb*Nr,1);
deps=zeros(6,1);
AVPM=zeros(5*Nb*Nr-2*(Nb+Nr)-1,6*Nb*Nr);
sigam=zeros(6,1);
Cs=zeros(6*Nb*Nr,6);
Tstrain=zeros(Nstep+1,1);
Tstress=zeros(Nstep+1,1);
AVP=zeros(6*Nb*Nr,6);


% compliance matrix of the fiber and the matrix
nuf21=Ef2*nuf12/Ef1;
nuf31=Ef3*nuf13/Ef1;
nuf32=Ef3*nuf23/Ef2;
Sf=[1/Ef1 -nuf21/Ef2 -nuf31/Ef3 0 0 0; -nuf12/Ef1 1/Ef2 -nuf32/Ef3 0 0 0;...
    -nuf13/Ef1 -nuf23/Ef2 1/Ef3 0 0 0; 0 0 0 1/Gf23 0 0; 0 0 0 0 1/Gf13 0; 0 0 0 0 0
    1/Gf12];
Cf=inv(Sf);


eSm=[1/Em -num/Em -num/Em 0 0 0; -num/Em 1/Em -num/Em 0 0 0;
     -num/Em -num/Em 1/Em 0 0 0; ...
     0 0 0 1/Gm 0 0; 0 0 0 0 1/Gm 0; 0 0 0 0 0 1/Gm];
eCm=inv(eSm);
```

```
% initial Cs
for beta=1:Nb
    for gama=1:Nr
        index=(beta-1)*Nr+gama;
        p1=6*(index-1)+1;
        p2=6*(index-1)+6;
        multi=1;
        region=regionf-index;
        for j=1:Nfiber
            multi=multi*region(1,j);
        end
        if multi ~= 0
            Cs(p1:p2,:)=eCm;
        else
            Cs(p1:p2,:)=Cf;
        end
    end
end

% AG matrix
index=-5;
for i=1:Nb*Nr                    % 11 displ. continuity
    index=index+6;
    AG(i,index)=1;
    J(i,1)=1;
end

for gama=1:Nr
    for beta=1:Nb
        index=(beta-1)*Nr+gama;
        AG(Nb*Nr+gama,(index-1)*6+2)=hb(1,beta);
        J(Nb*Nr+gama,2)=h;
        AG(Nb*Nr+Nr+beta,(index-1)*6+3)=hr(1,gama);
        J(Nb*Nr+Nr+beta,3)=l;
        AG(Nb*Nr+Nr+Nb+1,(index-1)*6+4)=hb(1,beta)*hr(1,gama)/2;
        J(Nb*Nr+Nr+Nb+1,4)=h*l/2;
        AG(Nb*Nr+Nr+Nb+1+beta,(index-1)*6+5)=hr(1,gama)/2;
        J(Nb*Nr+Nr+Nb+1+beta,5)=l/2;
```

```matlab
        AG(Nb*Nr+Nr+2*Nb+1+gama,(index-1)*6+6)=hb(1,beta)/2;
        J(Nb*Nr+Nr+2*Nb+1+gama,6)=h/2;
    end
end


% Tsig & Teps (Transformation Matrix)
Tsig=[cos(rad)^2 sin(rad)^2 0 0 0 2*cos(rad)*sin(rad);...
      sin(rad)^2 cos(rad)^2 0 0 0 -2*cos(rad)*sin(rad);...
      0 0 1 0 0 0;...
      0 0 0 cos(rad) -sin(rad) 0;...
      0 0 0 sin(rad) cos(rad) 0;...
      -cos(rad)*sin(rad) cos(rad)*sin(rad) 0 0 0 cos(rad)^2-sin(rad)^2];


Teps=[cos(rad)^2 sin(rad)^2 0 0 0 -cos(rad)*sin(rad);...
      sin(rad)^2 cos(rad)^2 0 0 0 cos(rad)*sin(rad);...
      0 0 1 0 0 0;...
      0 0 0 cos(rad) sin(rad) 0;...
      0 0 0 -sin(rad) cos(rad) 0;...
      2*cos(rad)*sin(rad) -2*cos(rad)*sin(rad) 0 0 0 cos(rad)^2-sin(rad)^2];


% K matrix
K=[zeros(5*Nb*Nr-2*(Nb+Nr)-1,6); J];


% Main Loop
for i=1:Nstep
    t=i*dtime;
    sigrate=strainrate(t,ratetype,angle/15);
    dsig1=[sigrate; 0; 0; 0; 0; 0];
    dsig=Tsig*dsig1;
    Tstress(i+1,1)=Tstress(i,1)+dsig1(1,1)*dtime;
    count=0;
    for beta=1:Nb-1 % construct AVPM matrix
        for gama=1:Nr
            betahat=beta+1;
            index=(beta-1)*Nr+gama-1;
            index2=(betahat-1)*Nr+gama-1;
            count=count+1;
            for j=1:6
```

```
            AVPM(count,6*index+j)=Cs(6*index+2,j);

            AVPM(count,6*index2+j)=-Cs(6*index2+2,j);

        end

        count=count+1;

        for j=1:6

            AVPM(count,6*index+j)=Cs(6*index+6,j);

            AVPM(count,6*index2+j)=-Cs(6*index2+6,j);

        end

        count=count+1;

        for j=1:6

            AVPM(count,6*index+j)=Cs(6*index+4,j);

            AVPM(count,6*index2+j)=-Cs(6*index2+4,j);

        end

    end

end


for gama=1:Nr-1

    for beta=1:Nb

        gamahat=gama+1;

        index=(beta-1)*Nr+gama-1;

        index2=(beta-1)*Nr+gamahat-1;

        count=count+1;

        for j=1:6

            AVPM(count,6*index+j)=Cs(6*index+3,j);

            AVPM(count,6*index2+j)=-Cs(6*index2+3,j);

        end

        count=count+1;

        for j=1:6

            AVPM(count,6*index+j)=Cs(6*index+5,j);

            AVPM(count,6*index2+j)=-Cs(6*index2+5,j);

        end

    end

end


for gama=1:Nr-1

    count=count+1;

    beta=Nb;

    gamahat=gama+1;
```

```
        index=(beta-1)*Nr+gama-1;

        index2=(beta-1)*Nr+gamahat-1;

        for j=1:6

            AVPM(count,6*index+j)=Cs(6*index+4,j);

            AVPM(count,6*index2+j)=-Cs(6*index2+4,j);

        end

end


AtVP=[AVPM; AG];

AVP=inv(AtVP)*K;

Bvp=zeros(6,6);


for beta=1:Nb

    for gama=1:Nr

        index=(beta-1)*Nr+gama;

        p1=6*(index-1)+1;

        p2=6*(index-1)+6;

        Bvp=Bvp+hb(1,beta)*hr(1,gama)*Cs(p1:p2,:)*AVP(p1:p2,:);

    end

end

Bvp=Bvp/h/l;

deps=inv(Bvp)*dsig;

deps1=Teps*deps;

Tstrain(i+1,1)=Tstrain(i,1)+deps1(1,1)*dtime;

for beta=1:Nb

    for gama=1:Nr

        index=(beta-1)*Nr+gama;

        p1=6*(index-1)+1;

        p2=6*(index-1)+6;

        multi=1;

        region=regionf-index;

        for j=1:Nfiber

            multi=multi*region(1,j);

        end


        if multi ~= 0

            subteps=AVP(p1:p2,:)*deps;

            subsigrate=Cs(p1:p2,:)*subteps;
```
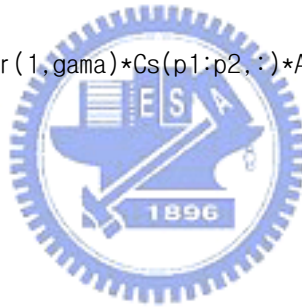
```matlab
        subeeps=eSm*subsigrate;
        subeps=subteps-subeeps;

        efeps=2/3*sqrt(1/2*((subeps(1,1)-subeps(2,1))^2+(subeps(2,1)-subeps(3,1
        ))^2+(subeps(3,1)-subeps(1,1))^2)+3/4*(subeps(4,1)^2+subeps(5,1)^2+sube
        ps(6,1)^2));

        substress(p1:p2,1)=substress(p1:p2,1)+subsigrate*dtime;
        sigam=substress(p1:p2,1);
        s1=1/3*(2*sigam(1,1)-sigam(2,1)-sigam(3,1));
        s2=1/3*(-sigam(1,1)+2*sigam(2,1)-sigam(3,1));
        s3=1/3*(-sigam(1,1)-sigam(2,1)+2*sigam(3,1));
        s4=2*sigam(4,1);
        s5=2*sigam(5,1);
        s6=2*sigam(6,1);
        efsig=sqrt((sigam(1,1)+sigam(2,1)+sigam(3,1))^2-3*(sigam(2,1)*sigam(3,1
        )-sigam(4,1)^2+sigam(1,1)*sigam(3,1)-sigam(5,1)^2+sigam(1,1)*sigam(2,1)
        -sigam(6,1)^2));
        A=xi*(efeps)^pm;
        pSm=9/4*A*pn*efsig^(pn-3)*[s1; s2; s3; s4; s5; s6]*[s1; s2; s3; s4; s5;
            s6]';
        Sm=eSm+pSm;
        Cs(p1:p2,:)=inv(Sm);
    else
        Cs(p1:p2,:)=Cf;
    end
  end
 end
end
```
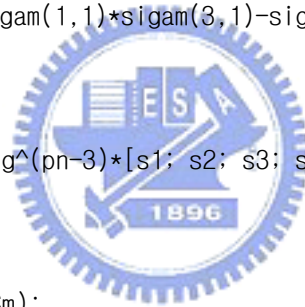
Table 1. Material properties used in the micromechanical analysis where the matrix properties were obtained from experiments and the fiber properties were determined to fit the linear elastic of experimental data at all off-axis angles.

	Fiber	Matrix
E_1 (GPa)	235	3.4
E_2 (GPa)	18	
G_{12} (GPa)	35	
G_{23} (GPa)	7.2	
ν_{12}	0.2	0.37
ν_{23}	0.25	
V_f (%)	69	
α (1/°C)		5.9×10^{-5}
n		5.62
χ (MPa)$^{-n}$		1.23×10^{-14}
m		-0.168

Table 2. Material properties employed in the finite element analysis.

	E_1 (GPa)	E_2 (GPa)	G_{12} (GPa)	G_{23} (GPa)	ν_{12}	ν_{23}	k (MPa)	R_0	R_∞	b
Fiber	234	14	27.6	5.5	0.2	0.25				
Matrix	3.4				0.3		35	2900	61.64	600
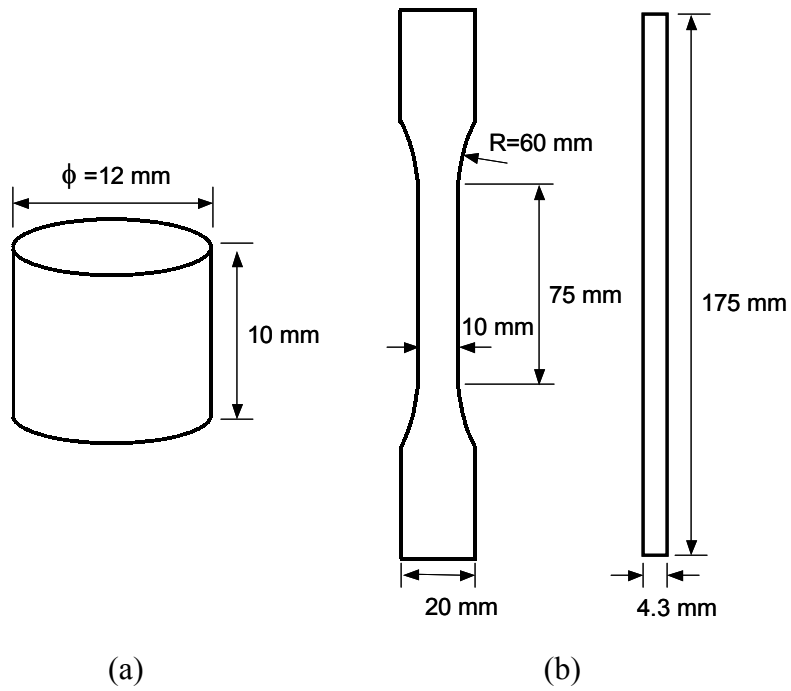
Fig. 2.1 Dimensions of tensile and compression specimens. (a) Cylindrical

compression specimen. (b) Coupon tensile specimen.
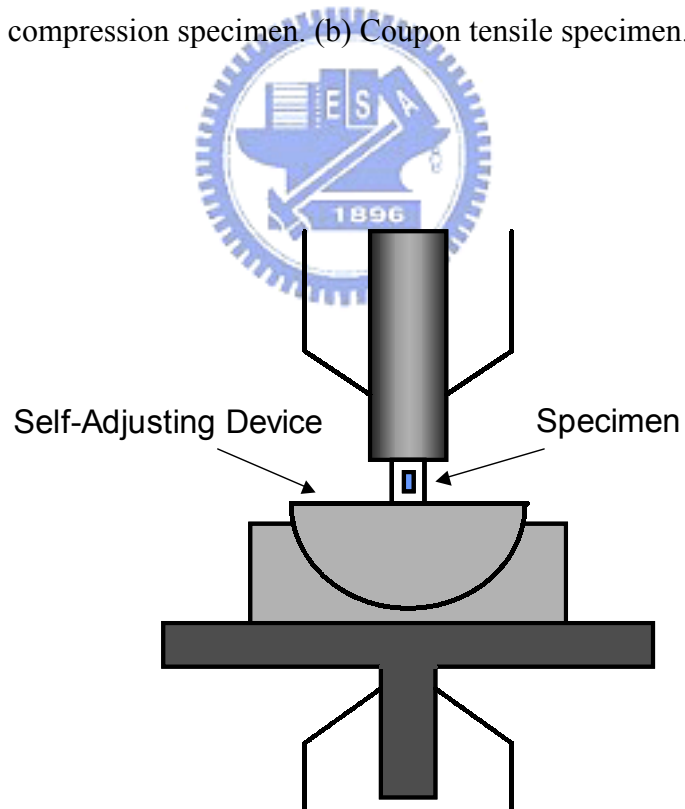
Fig. 2.2 Experimental setup for compression tests.
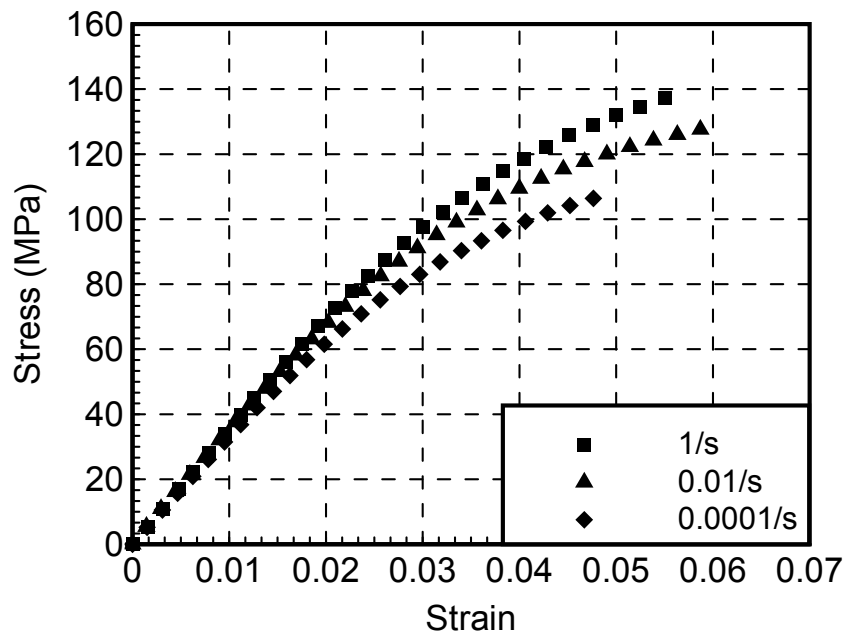
Fig. 2.3 Compression test results of polymer at 10^{-4}, 10^{-2} and 1/s strain rates.
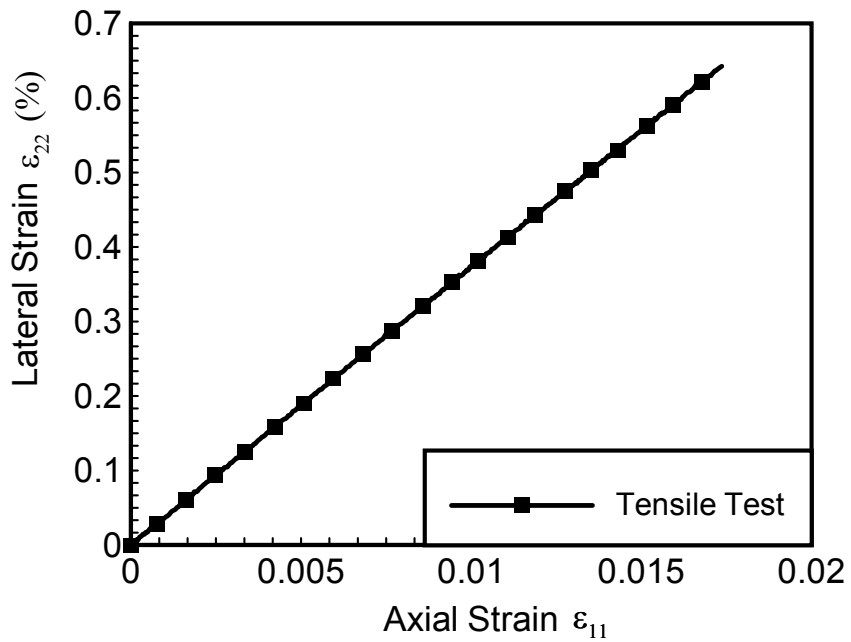
Fig. 2.4 Tensile test result to determine Poisson's ratio of the polymer.
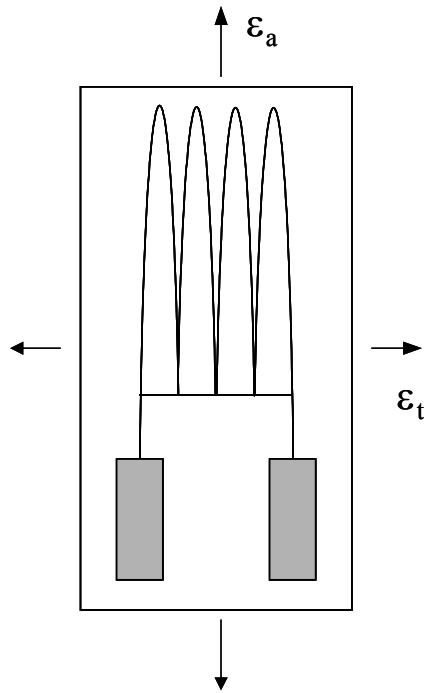
Fig. 2.5 Schematic for a strain gage subjected to a biaxial strain field.
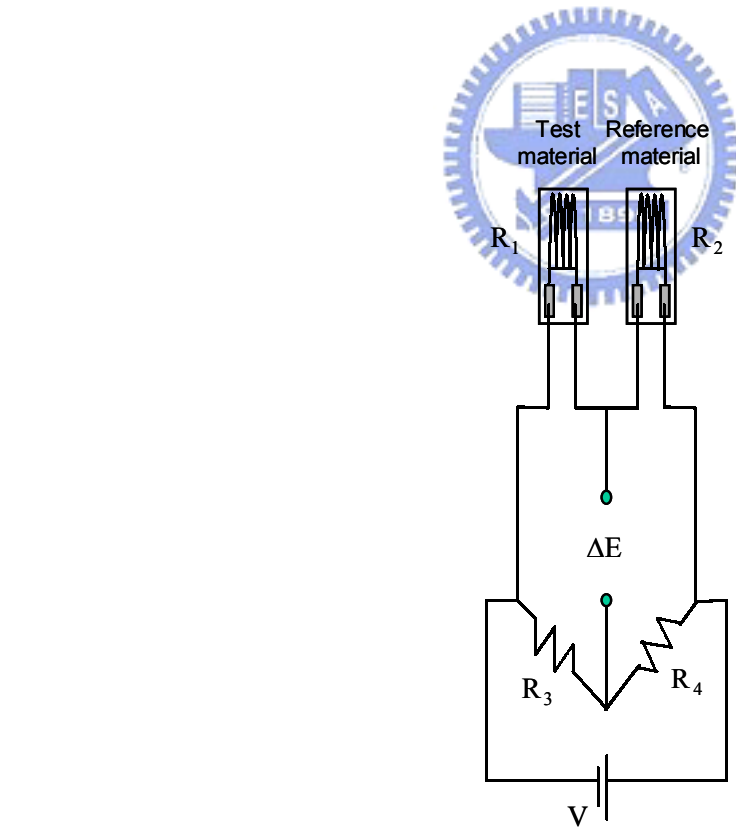
Fig. 2.6 A half-bridge circuit for measuring the coefficient of thermal expansion.
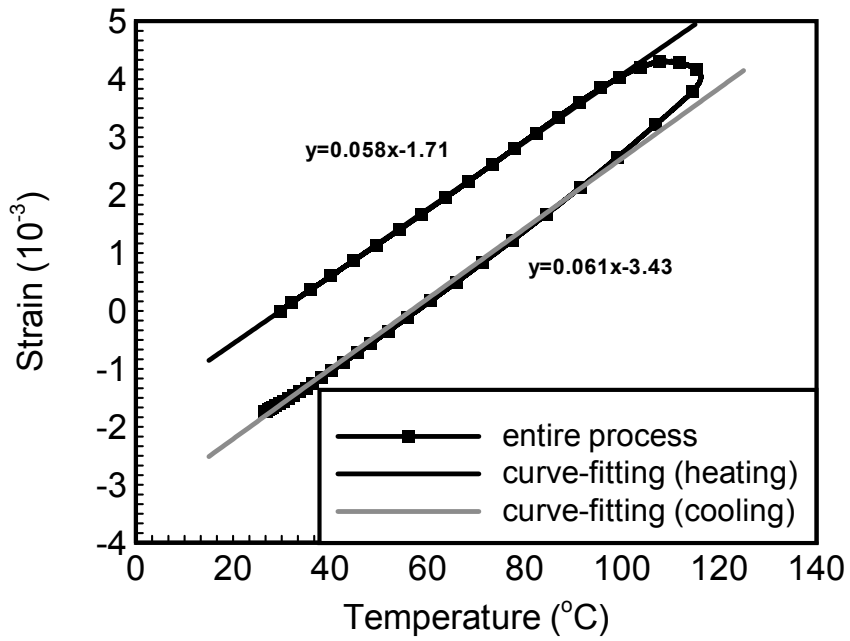
Fig. 2.7 Thermal response for the polymer.
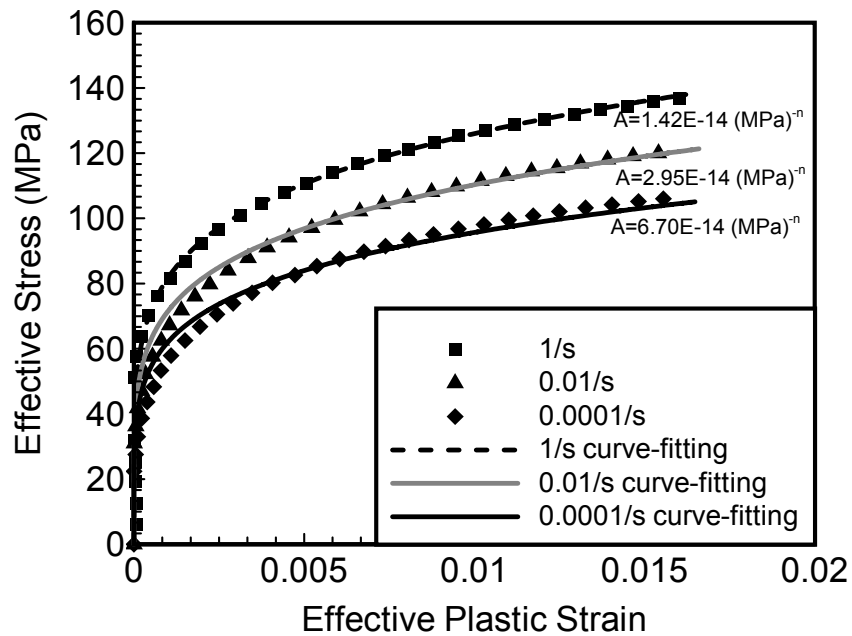
Fig. 2.8 Effective stress – effective plastic strain curves for polymer at three different
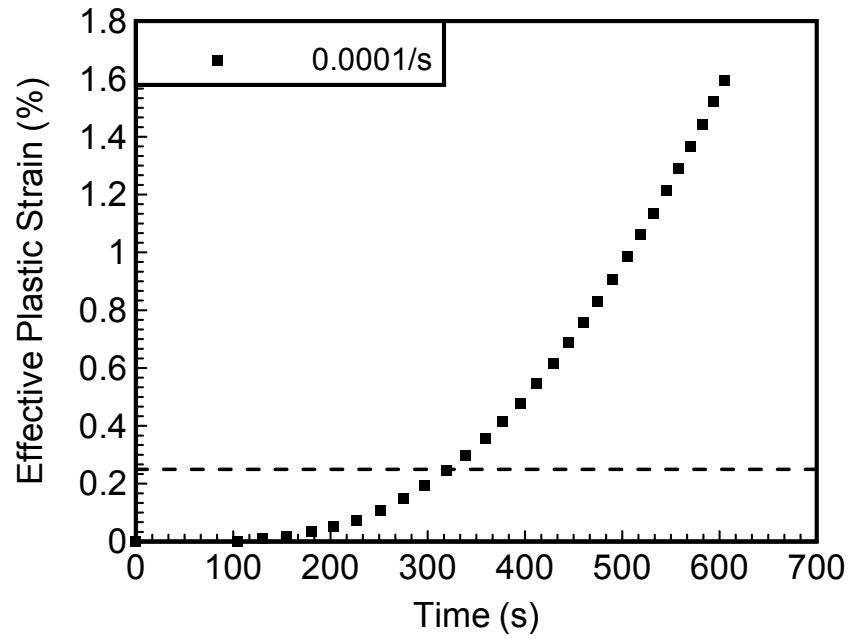
strain rates.

Fig. 2.9 Effective plastic strain versus time curve for epoxy at strain rate of 10^{-4}/s.
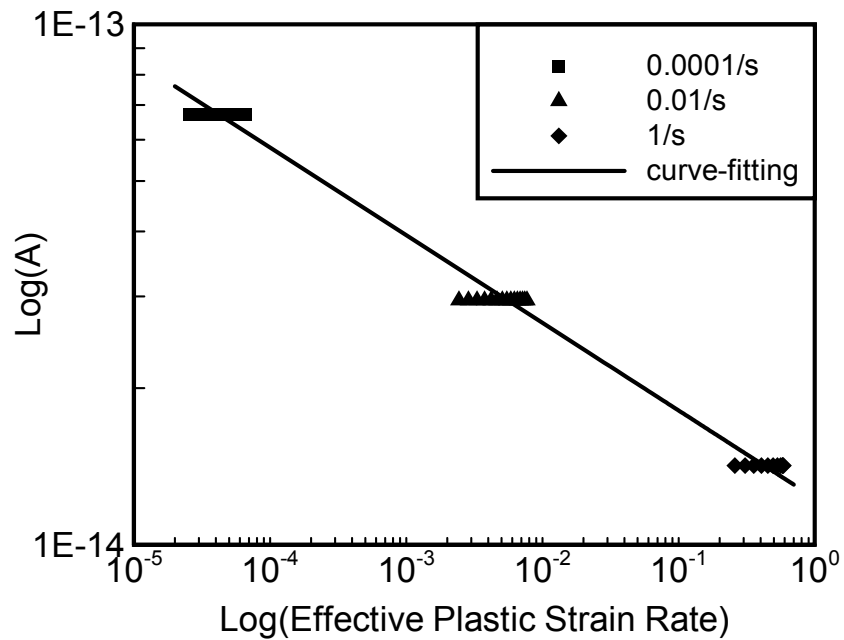
Fig. 2.10 Log-log plot for determining the parameters in the viscoplasticity model.
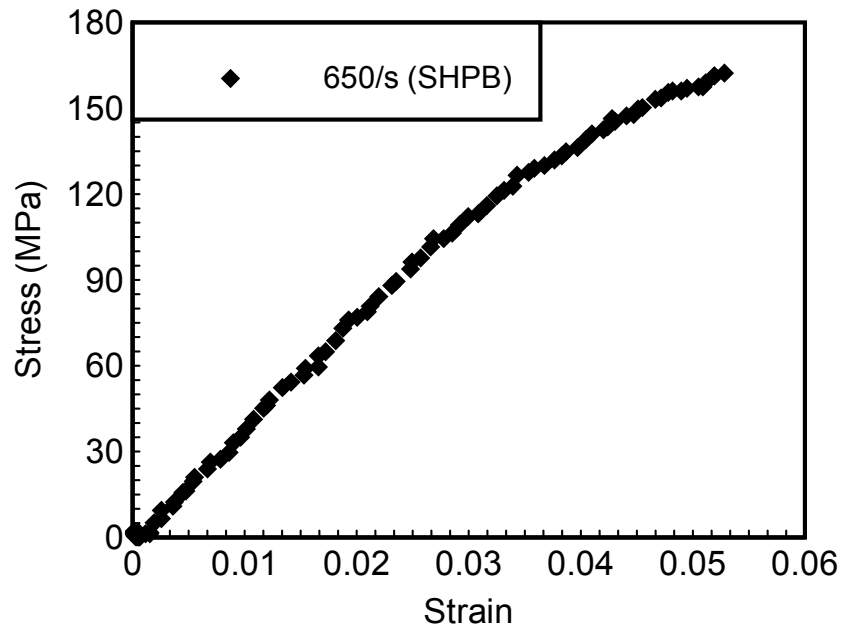
Fig. 2.11 The stress – strain curve of the polymer from SHPB results.
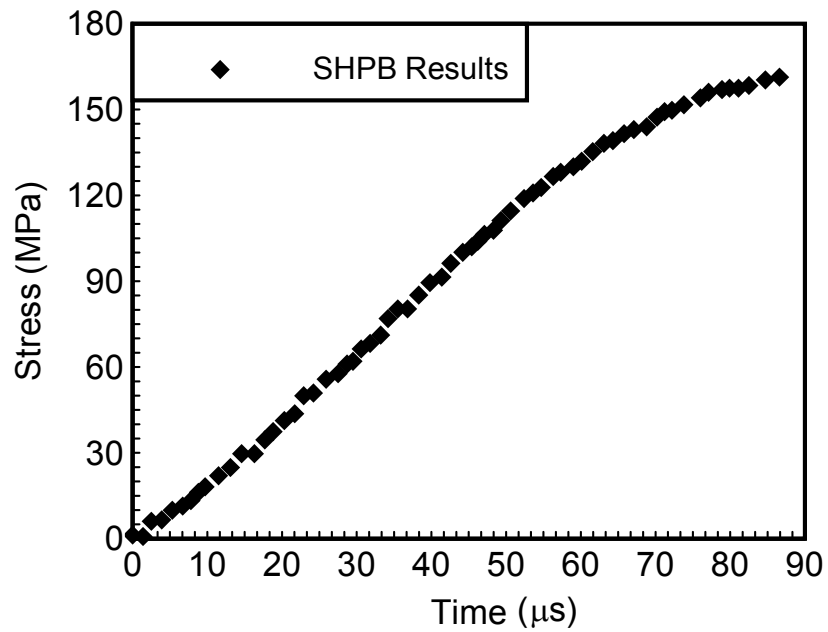
Fig. 2.12 The stress – time curve from SHPB test.
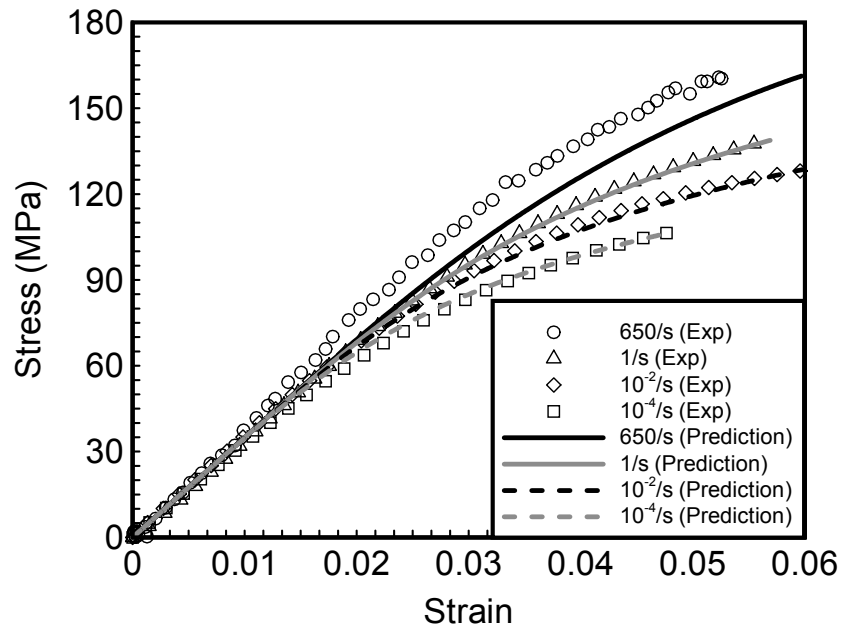
Fig. 2.13 Prediction results of polymer at different strain rates by using three

parameters model.

(a)   (b)
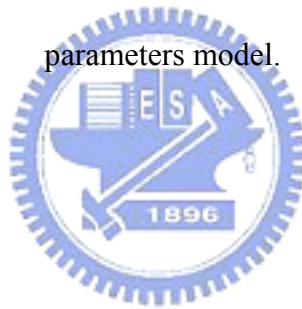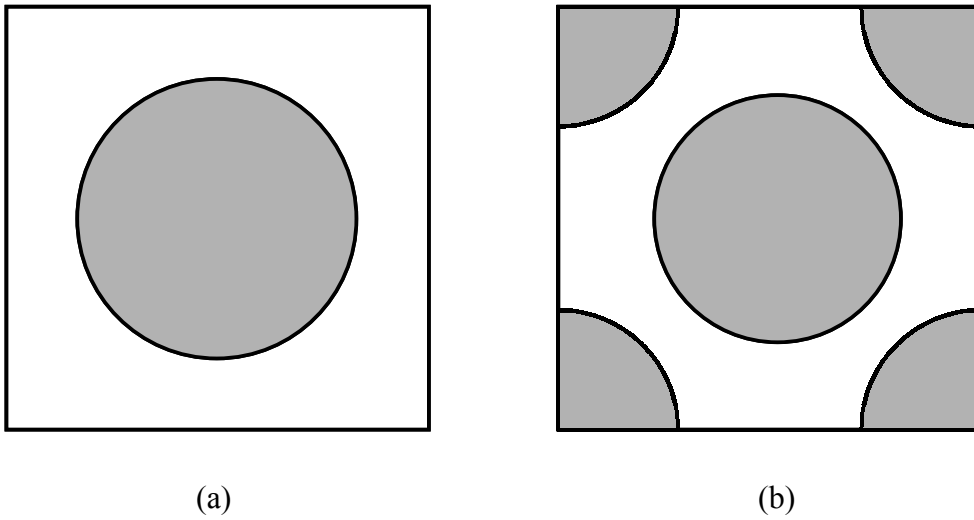
Fig. 3.1 Demonstration of RVEs with various fiber arrangements. (a) Square edge

packing array. (b) Square diagonal packing array.
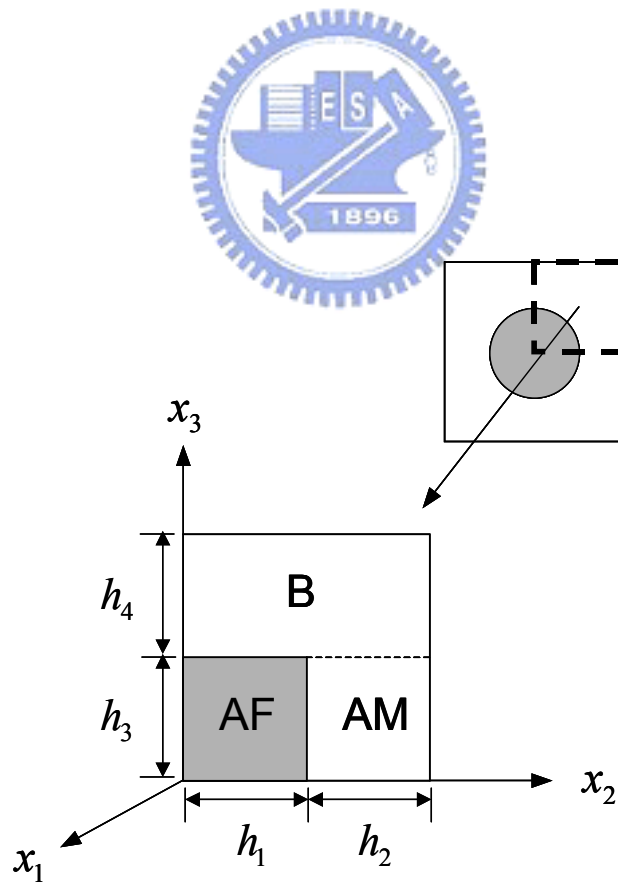
Fig. 3.2 Geometry of square fiber model [12].
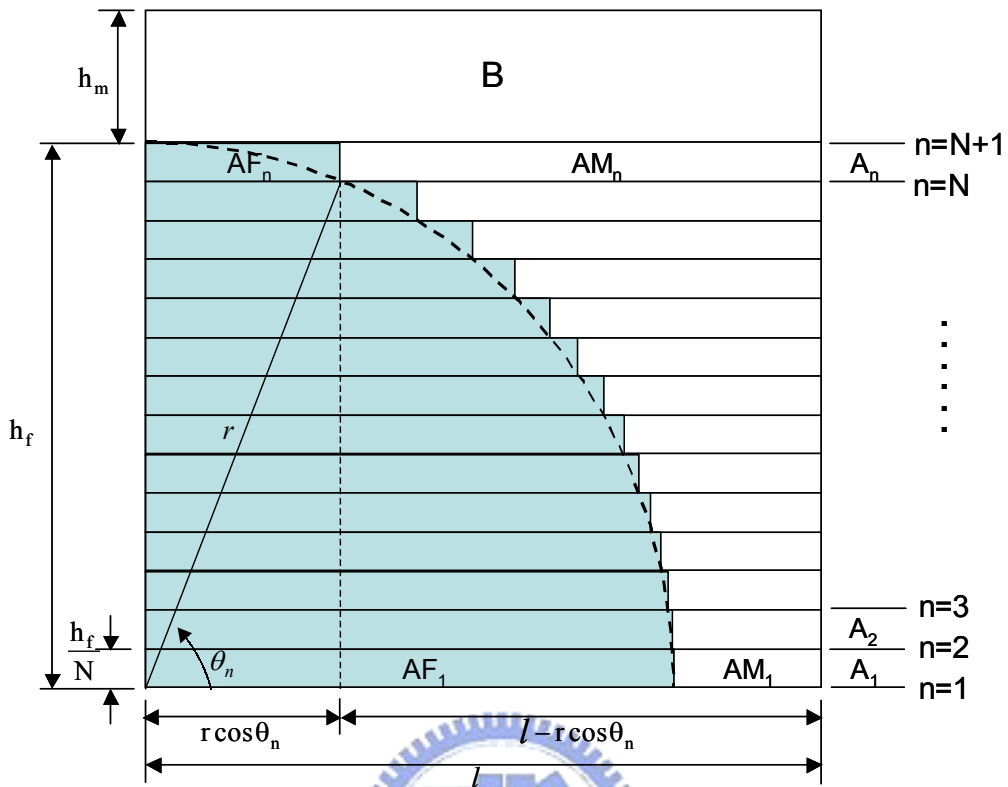
Fig. 3.3 Square edge packing array for modified square fiber model.
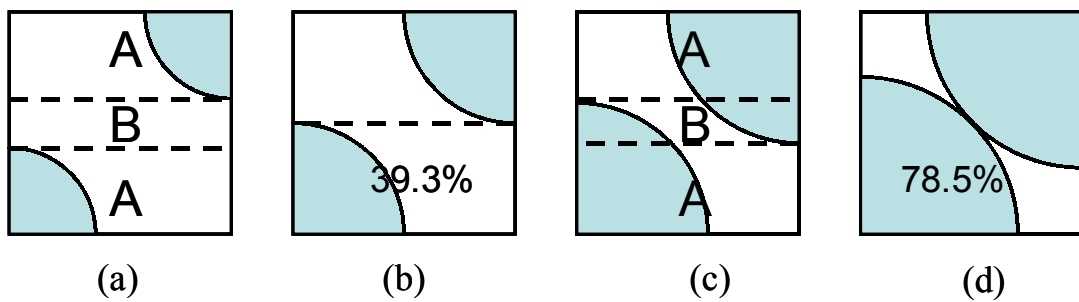
Fig. 3.4 Fiber distribution of square diagonal packing array (SDP) based on the fiber

volume fraction. (a) Less than 39.3 %. (b) Equal to 39.3 %. (c) Greater than 39.3

%. (d) Attain to maximum fiber volume fraction 78.5 %.
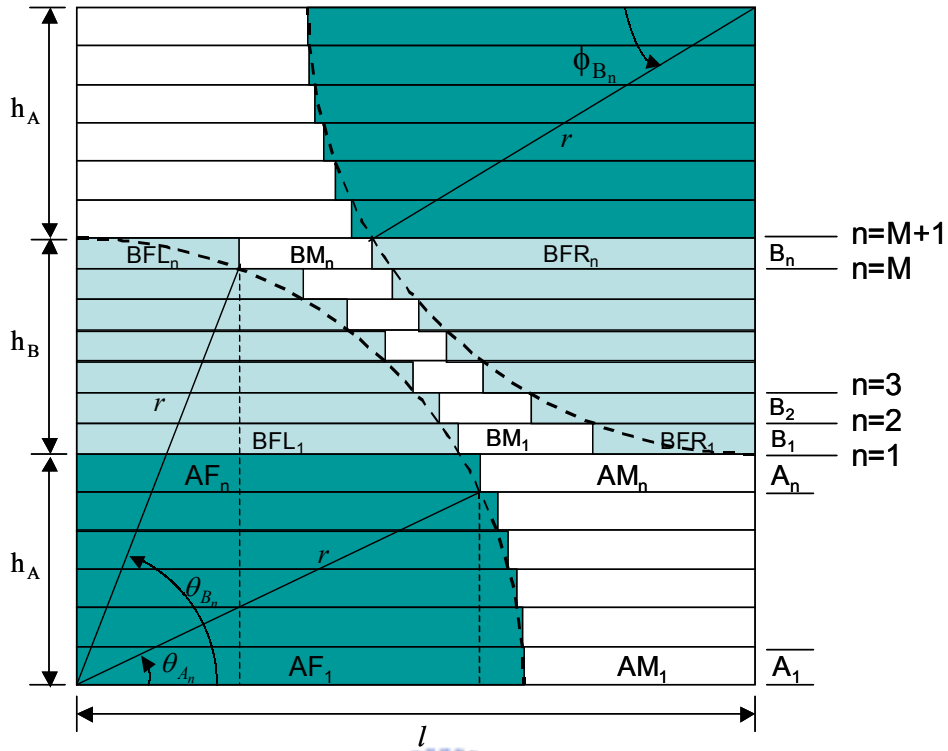
Fig. 3.5 Square diagonal packing array for modified square fiber model.
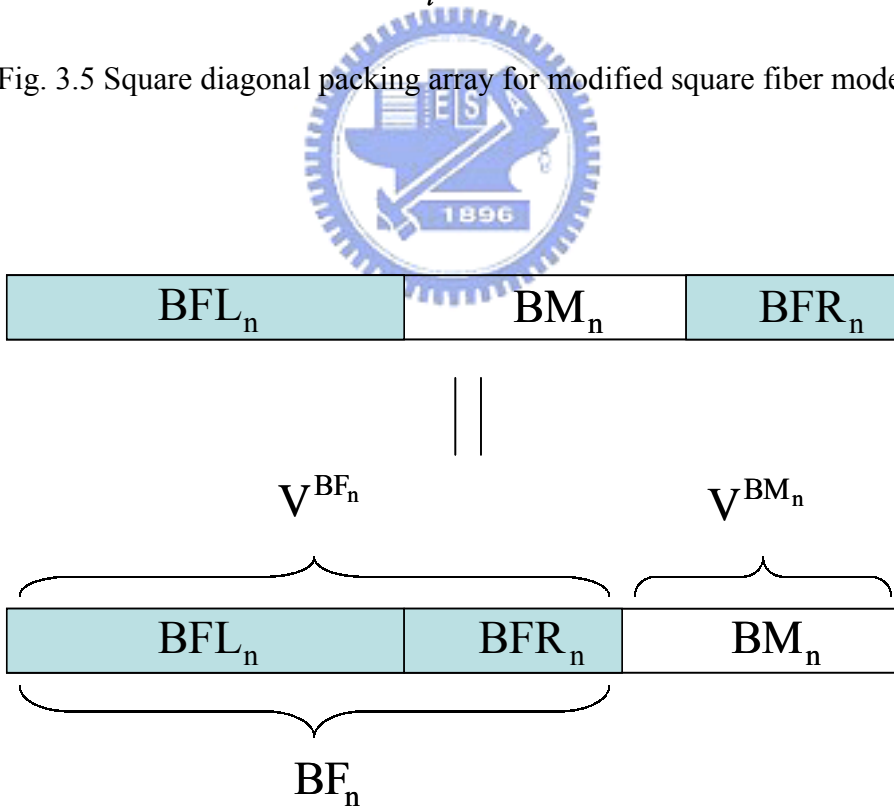
Fig. 3.6 Two fiber phases can be treated as a whole one if the constant stress or strain

assumptions in eqn (3.2.21) were applied.
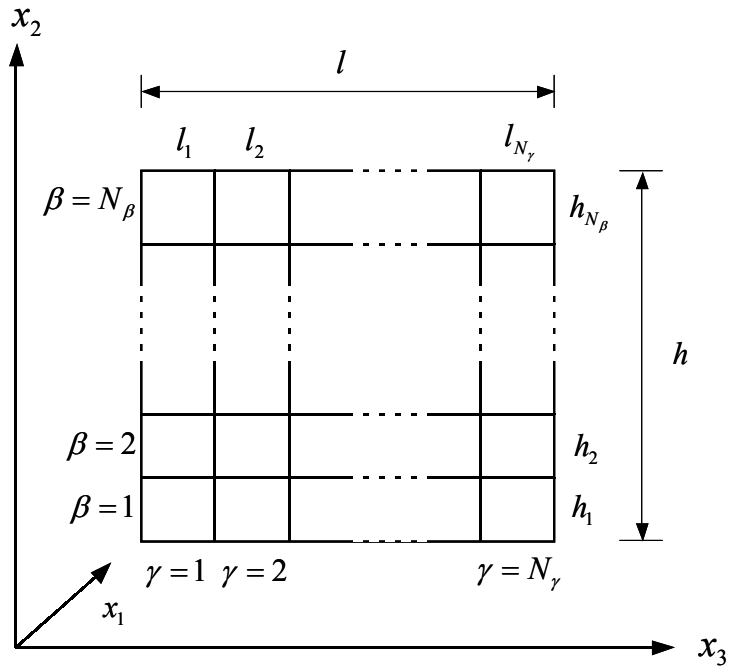
Fig. 4.1 The coordinate system and geometry information of the generalized method of cells [15].
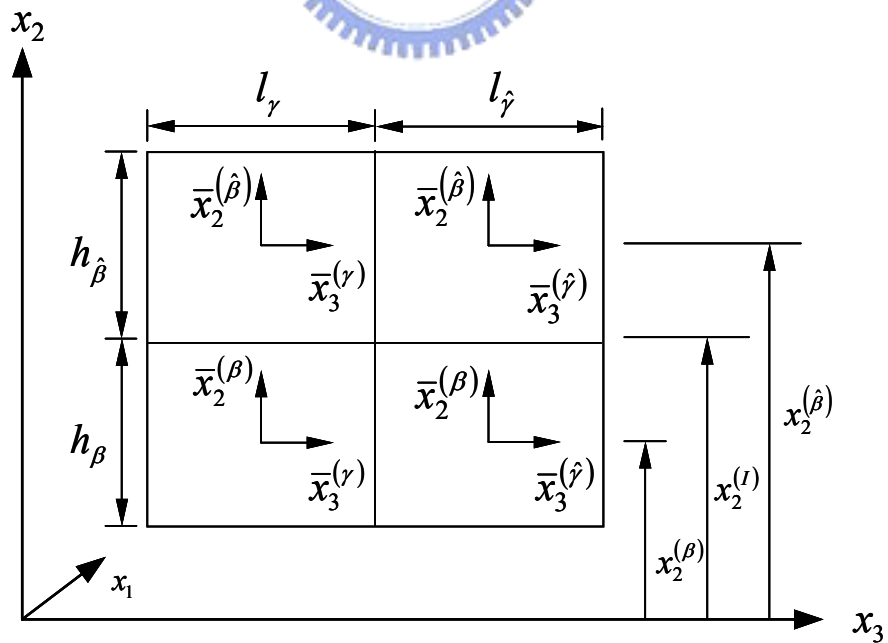
Fig. 4.2 Local coordinate systems of the generalized method of cells [15].
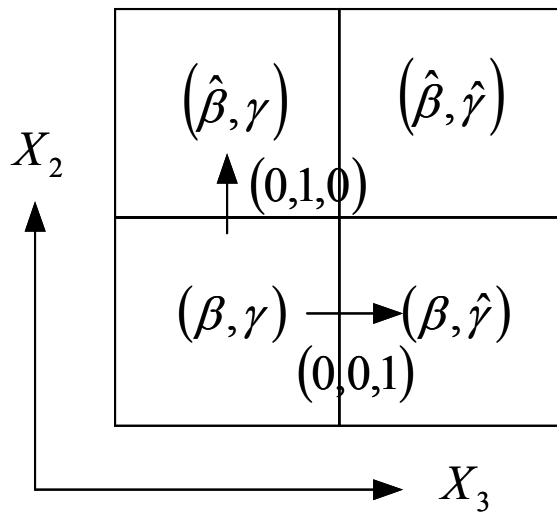
Fig. 4.3 Normal vectors at the interfaces of subcells.
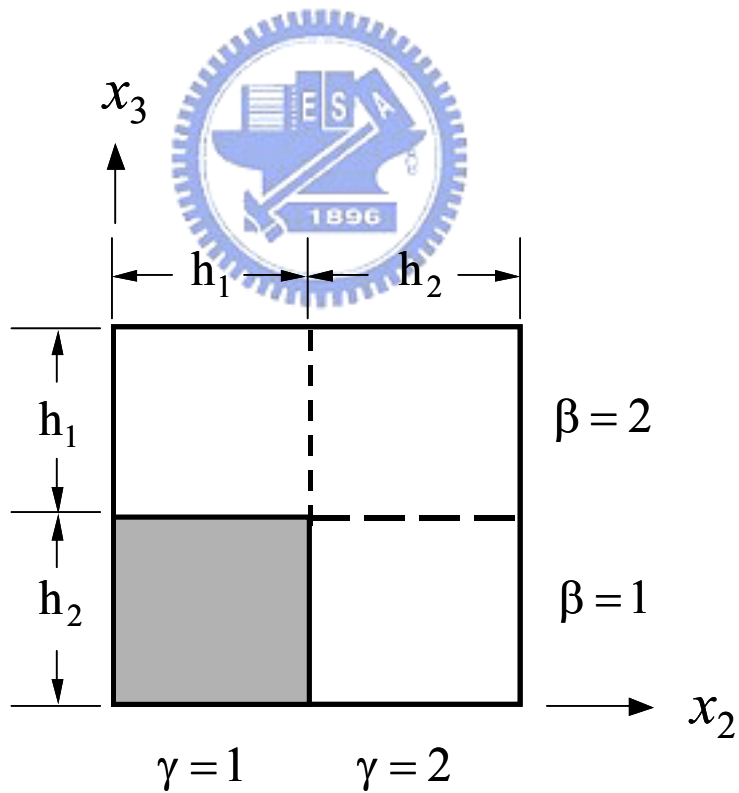
Fig. 4.4 A four regions RVE employed in the GMC, in which $\beta = \gamma = 1$ represents

the fiber phase.
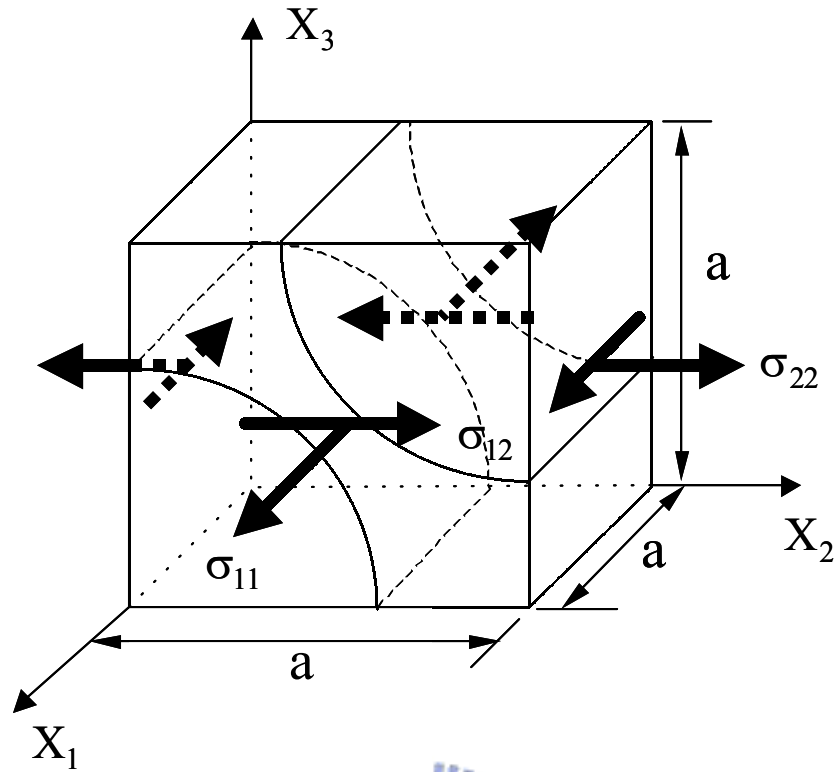
Fig. 5.1 3-D square diagonal packing array employed in ANSYS.
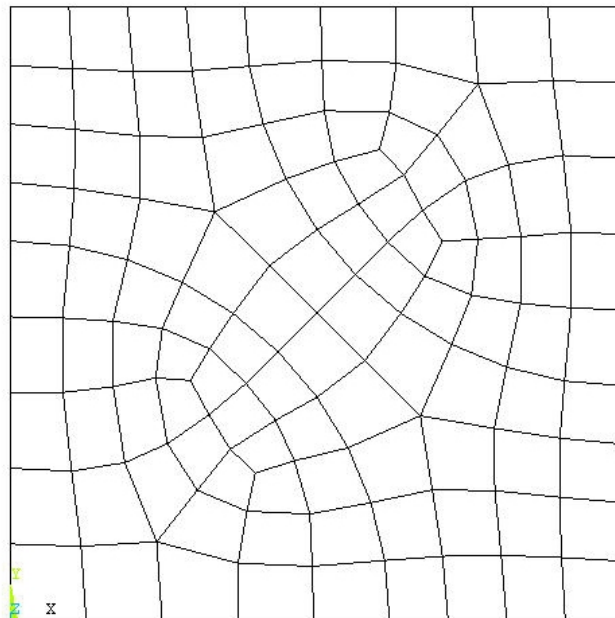
Fig. 5.2 (a) A finite element mesh generated by ANSYS.
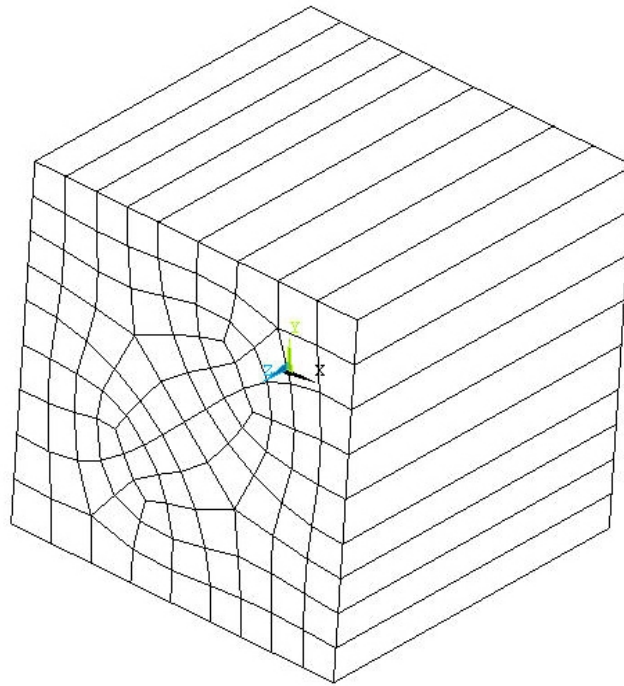
Fig. 5.2 (b) A full view of finite element mesh.
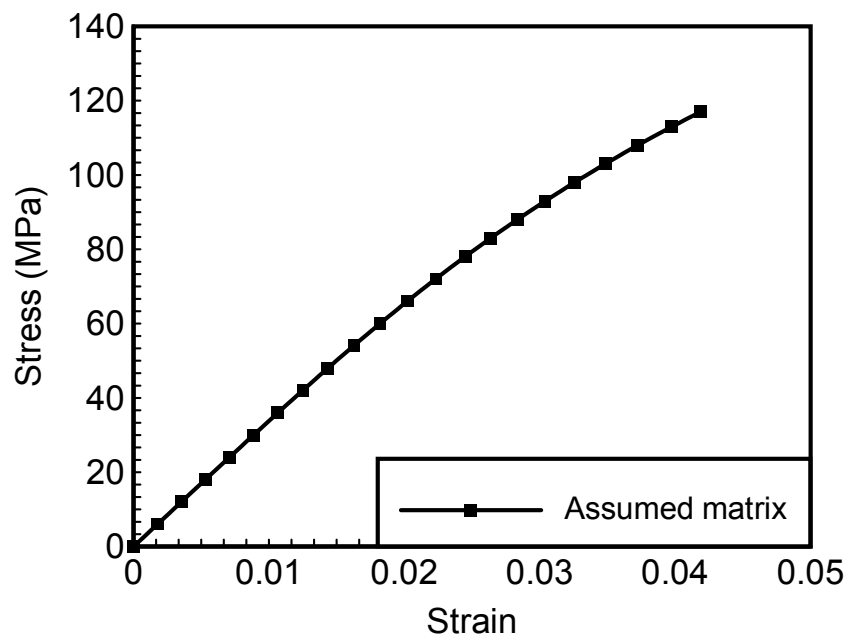
Fig. 5.3 An assumed stress–strain curve of the matrix.
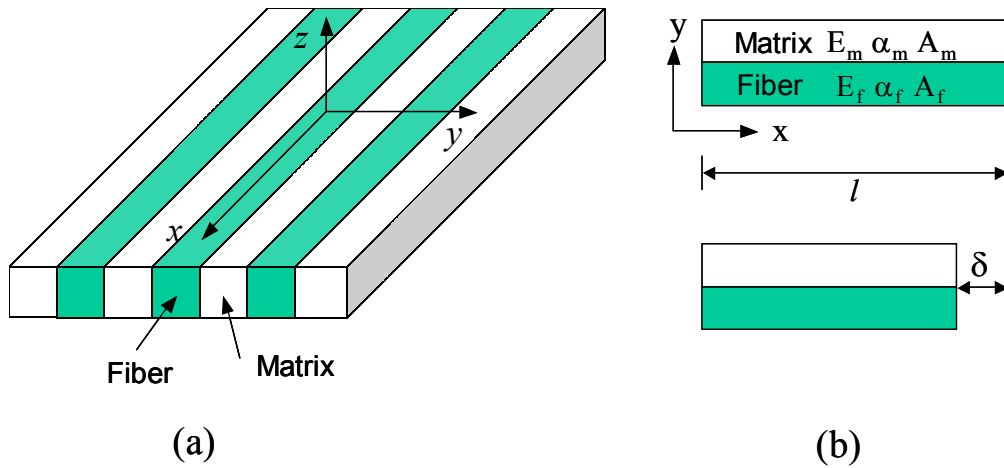
Fig. 6.1 (a) Simplified model for unidirectional fiber composites. (b) Evaluation of thermal residual stress based on the displacement continuity in the x direction.
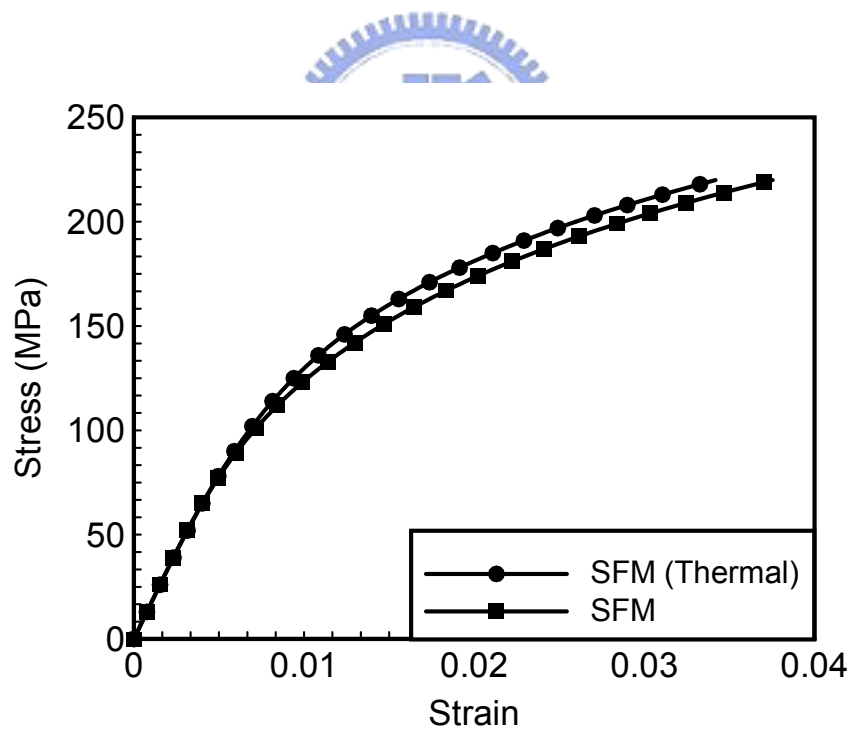
Fig. 6.2(a) Thermal stress effect on the stress and strain curve of 30^0 fiber composite obtained from the square fiber model.
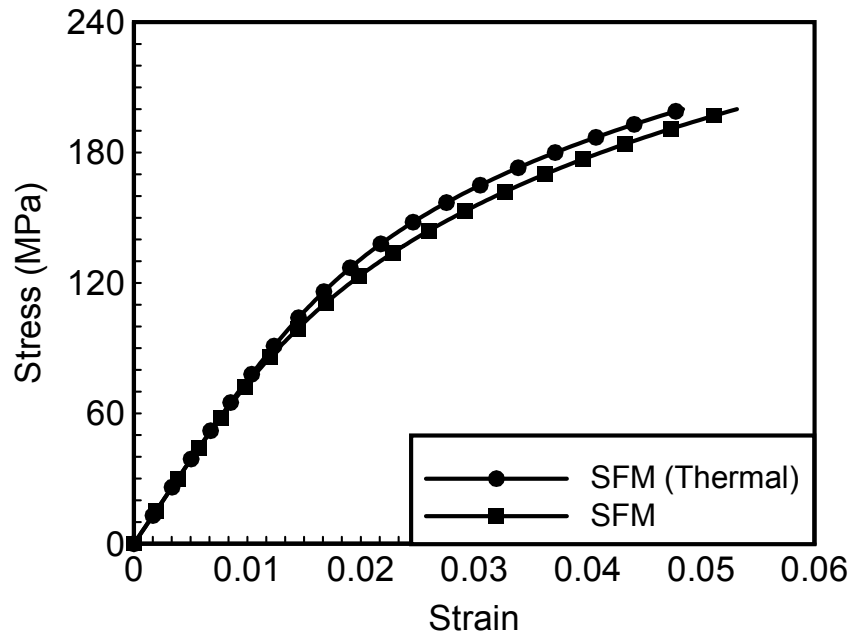
Fig. 6.2(b) Thermal stress effect on the stress and strain curve of 90^0 fiber composite obtained from the square fiber model.
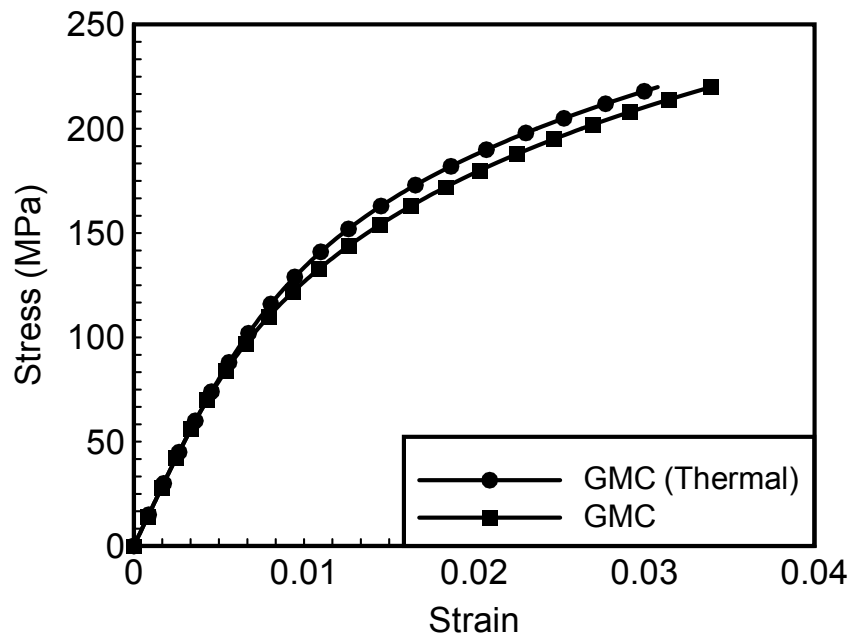
Fig. 6.3(a) Thermal stress effect on the stress and strain curve of 30^0 fiber composite obtained from the generalized method of cells.
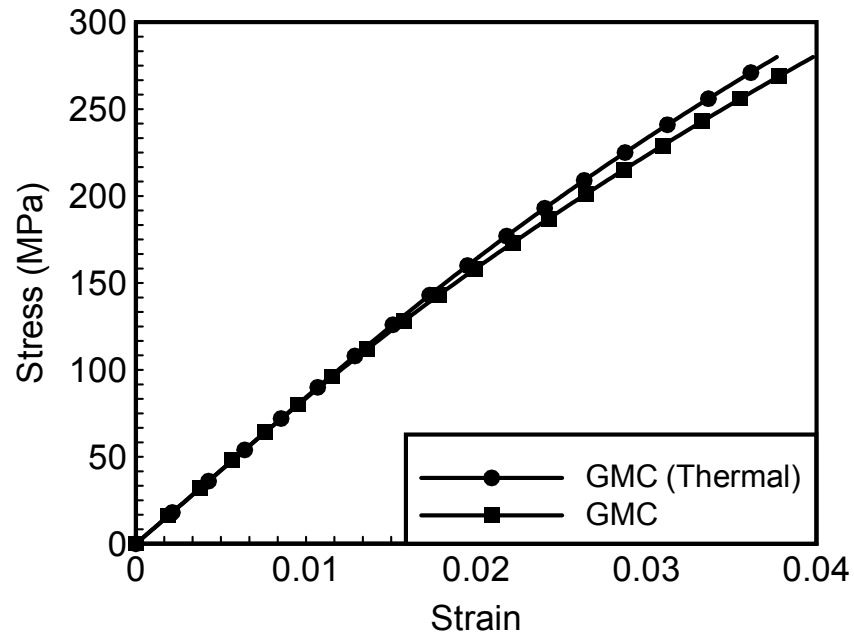
Fig. 6.3(b) Thermal stress effect on the stress and strain curve of 90^0 fiber composite obtained from the generalized method of cells.
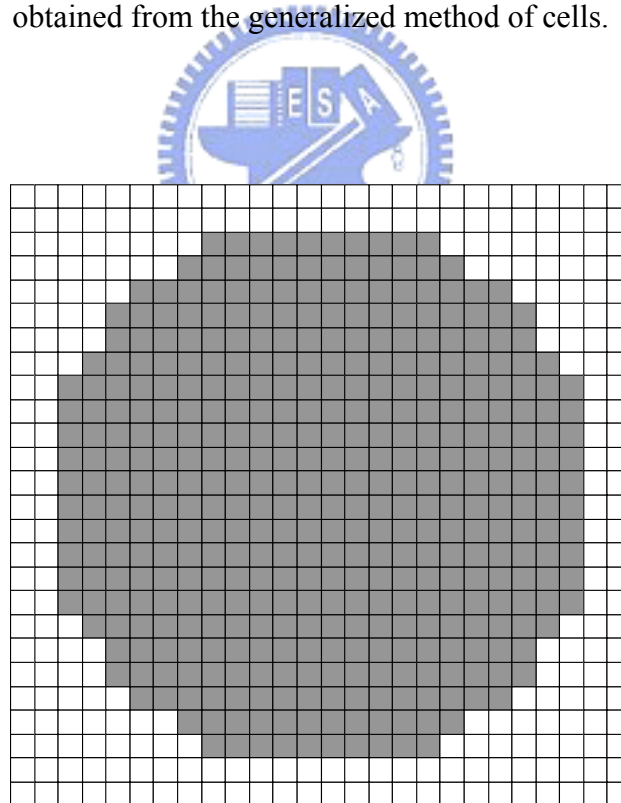
Fig. 6.4 The RVE with 26×26 subcells employed in the calculation of generalized method of cells (square edge packing).
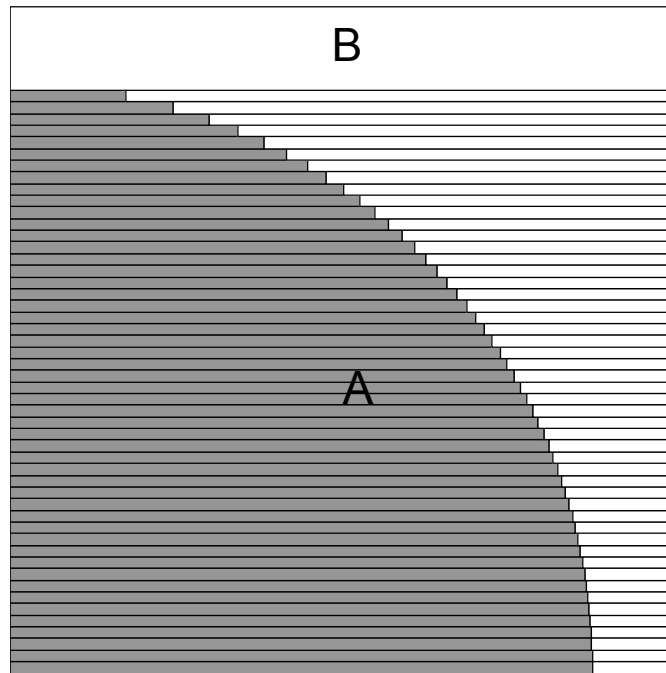
Fig. 6.5 The RVE with 50 subcells in fibrous region employed in the modified square fiber model (square edge packing).
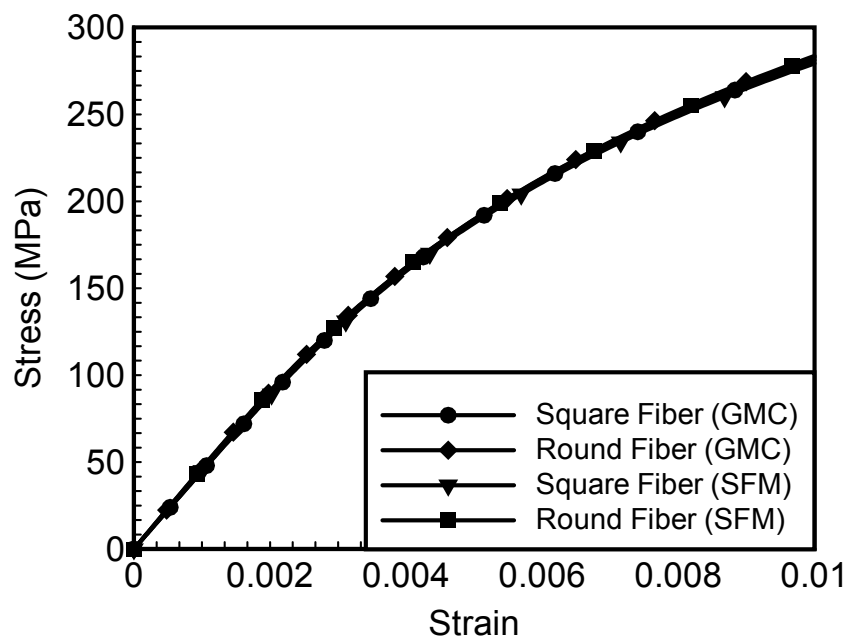
Fig. 6.6(a) Fiber shape effects on the stress and strain curves of 15^0 fiber composites using the generalized method of cells (GMC) and the square fiber model (SFM).
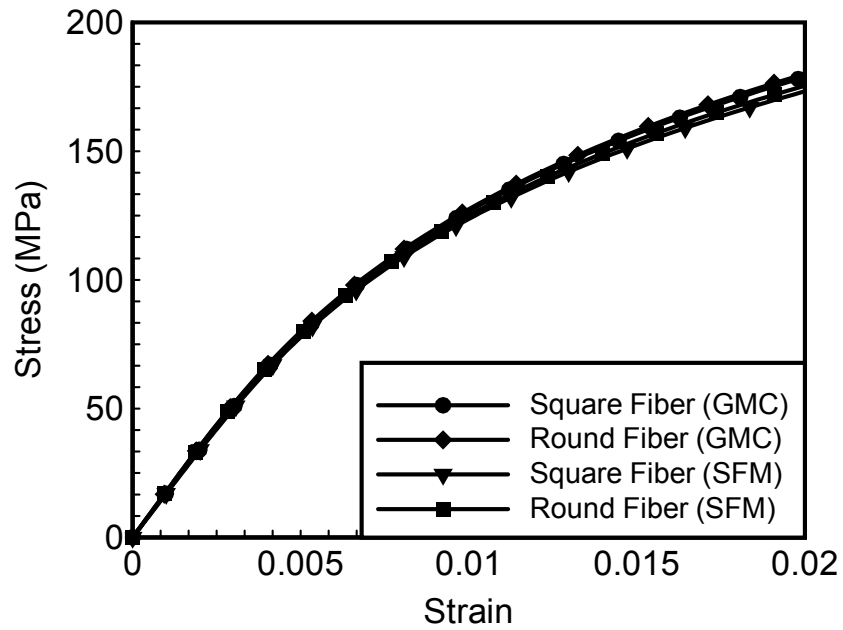
Fig. 6.6(b) Fiber shape effects on the stress and strain curves of 30^0 fiber composites using the generalized method of cells (GMC) and the square fiber model (SFM).
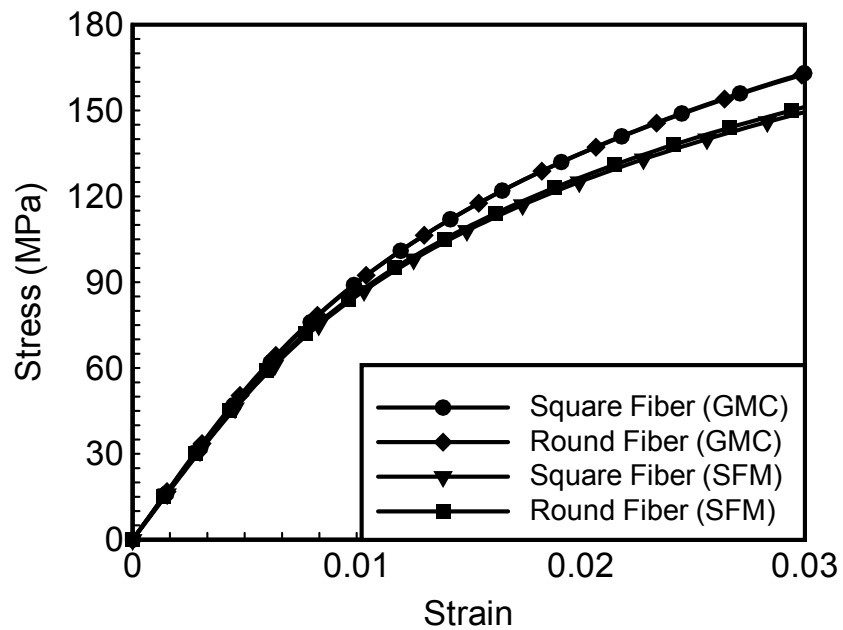
Fig. 6.6(c) Fiber shape effects on the stress and strain curves of 45^0 fiber composites using the generalized method of cells (GMC) and the square fiber model (SFM).
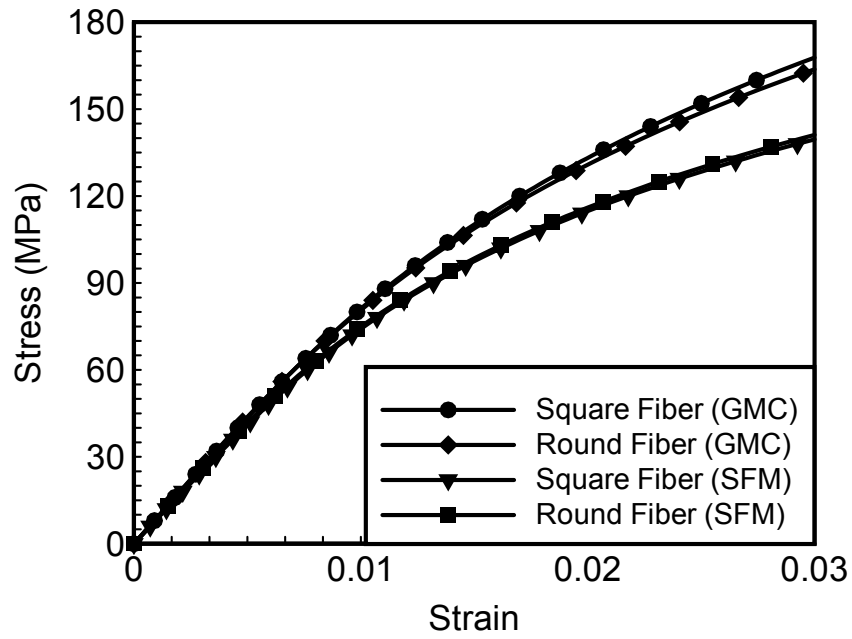
Fig. 6.6(d) Fiber shape effects on the stress and strain curves of 60^0 fiber composites using the generalized method of cells (GMC) and the square fiber model (SFM).
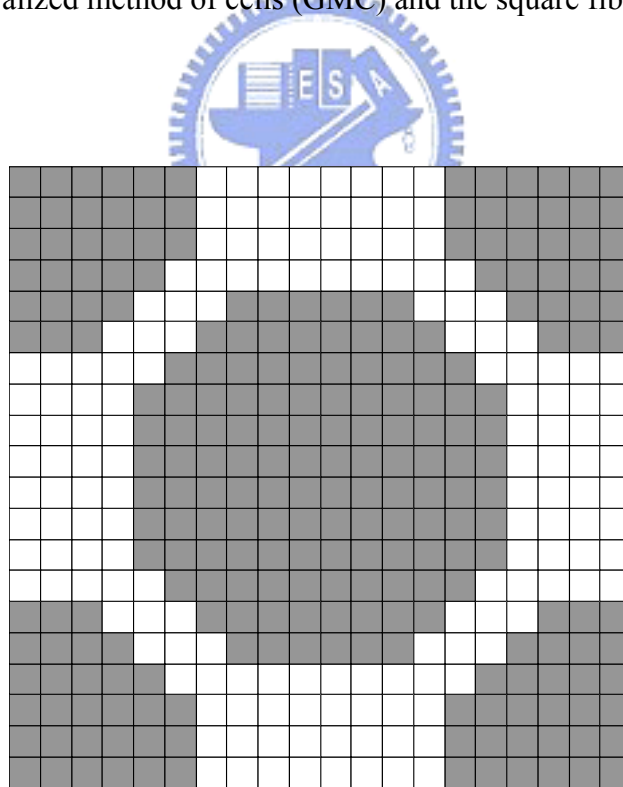
Fig. 6.7 The RVE with 20×20 subcells employed in the calculation of generalized method of cells (square diagonal packing).
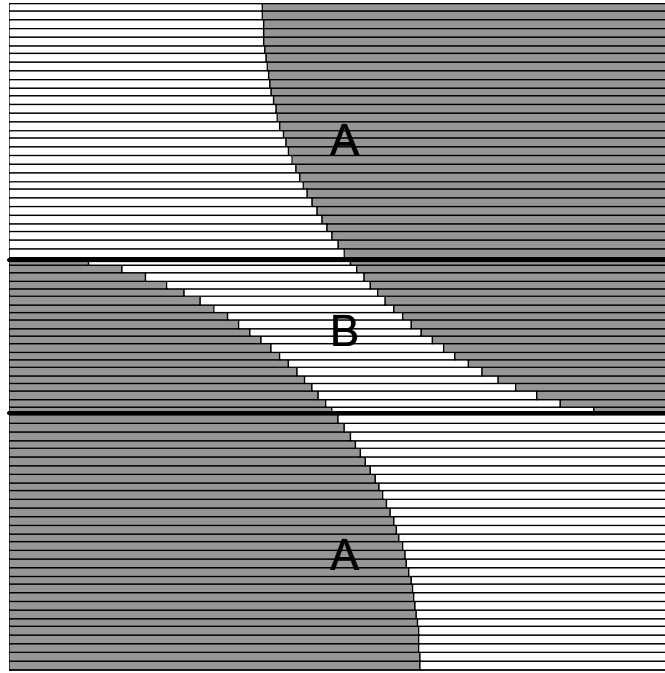
Fig. 6.8 The RVE employed in the modified square fiber model (square diagonal packing).
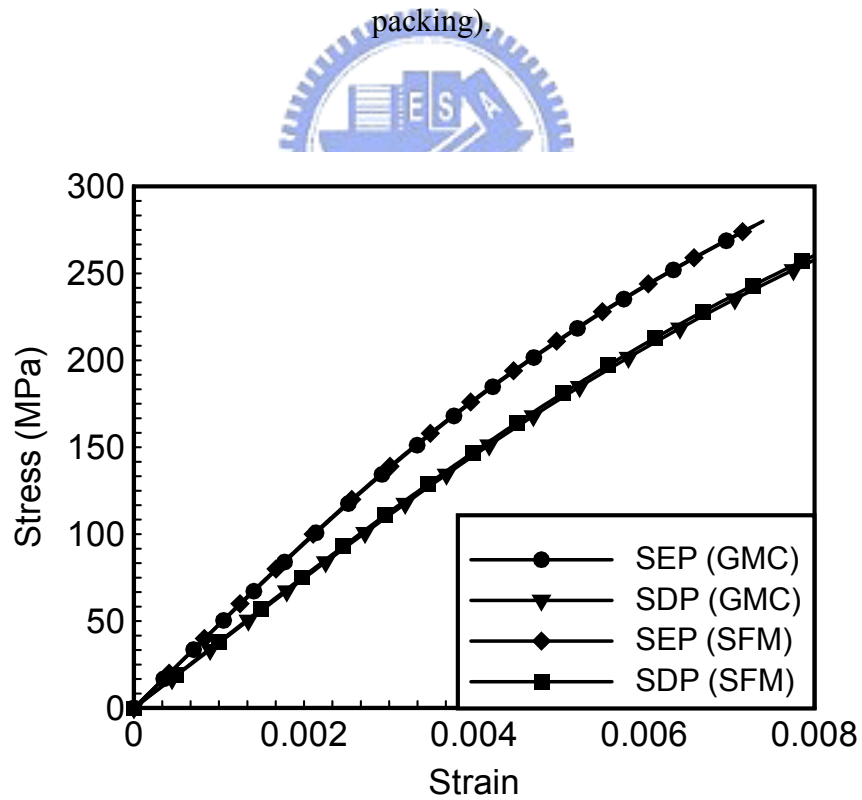
Fig. 6.9(a) The effect of fiber arrangements on the stress and strain curves of 15^0 fiber composites obtained from the SFM and GMC.
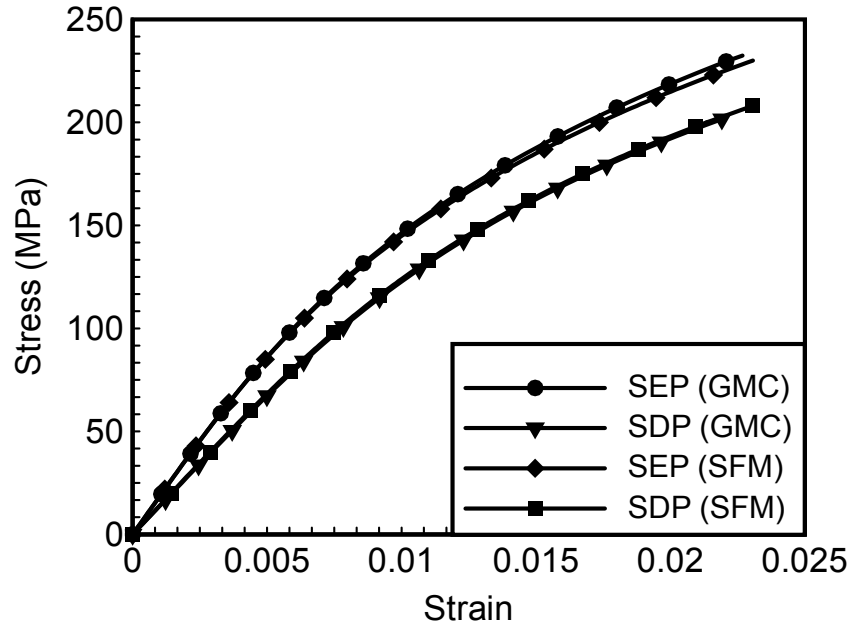
Fig. 6.9(b) The effect of fiber arrangements on the stress and strain curves of 30^0 fiber composites obtained from the SFM and GMC.
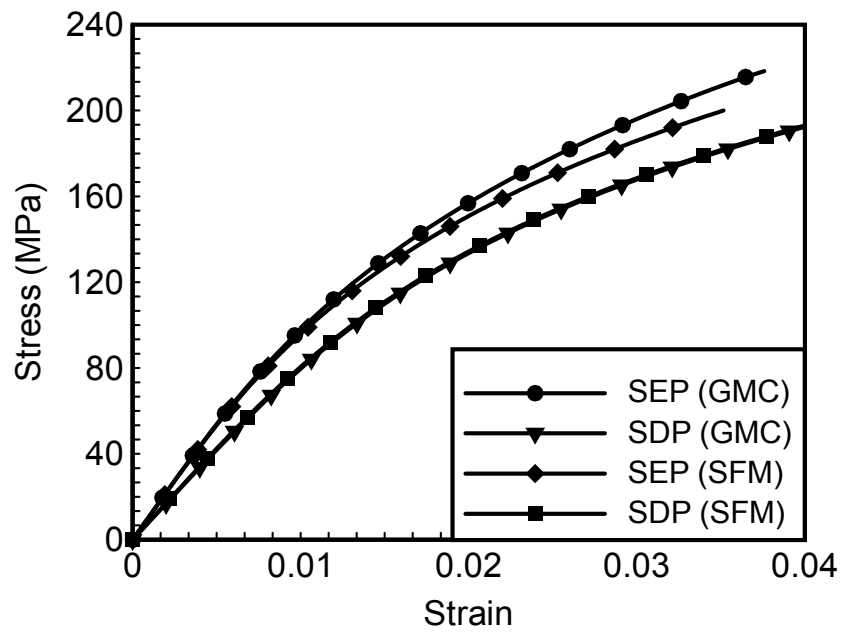
Fig. 6.9(c) The effect of fiber arrangements on the stress and strain curves of 45^0 fiber composites obtained from the SFM and GMC.
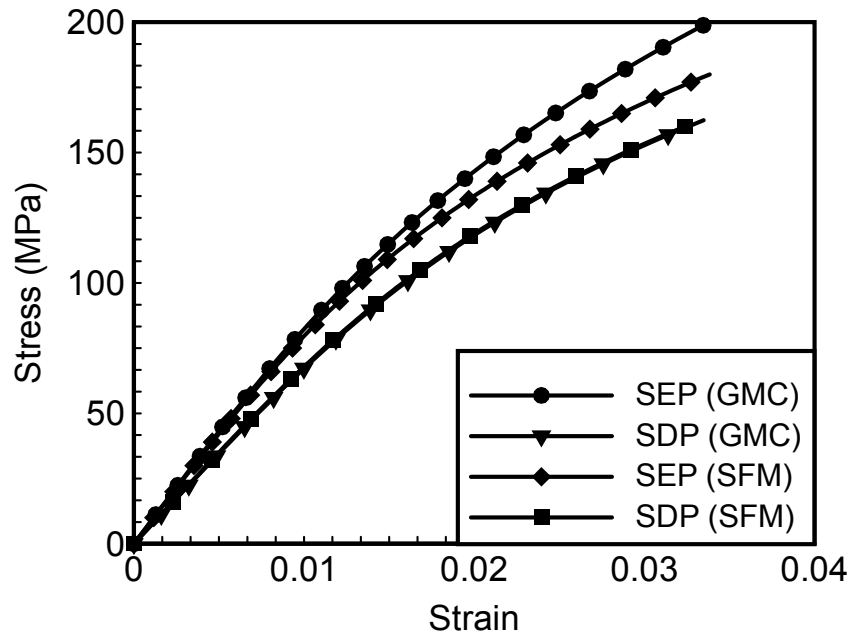
Fig. 6.9(d) The effect of fiber arrangements on the stress and strain curves of 60^0 fiber composites obtained from the SFM and GMC.
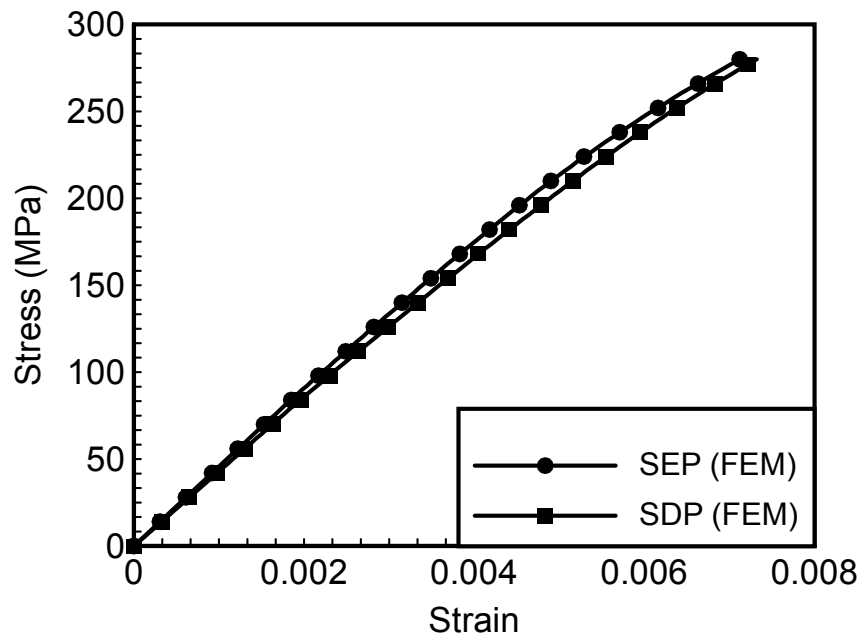
Fig. 6.10(a) The effect of fiber arrangements on the stress and strain curves of 15^0 fiber composites obtained from the FEM.
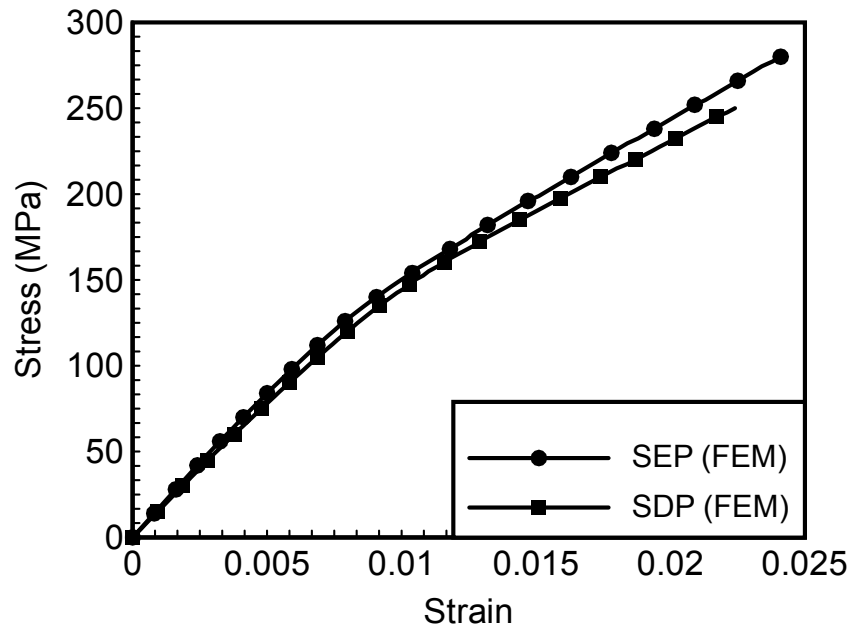
Fig. 6.10(b) The effect of fiber arrangements on the stress and strain curves of 30^0 fiber composites obtained from the FEM.
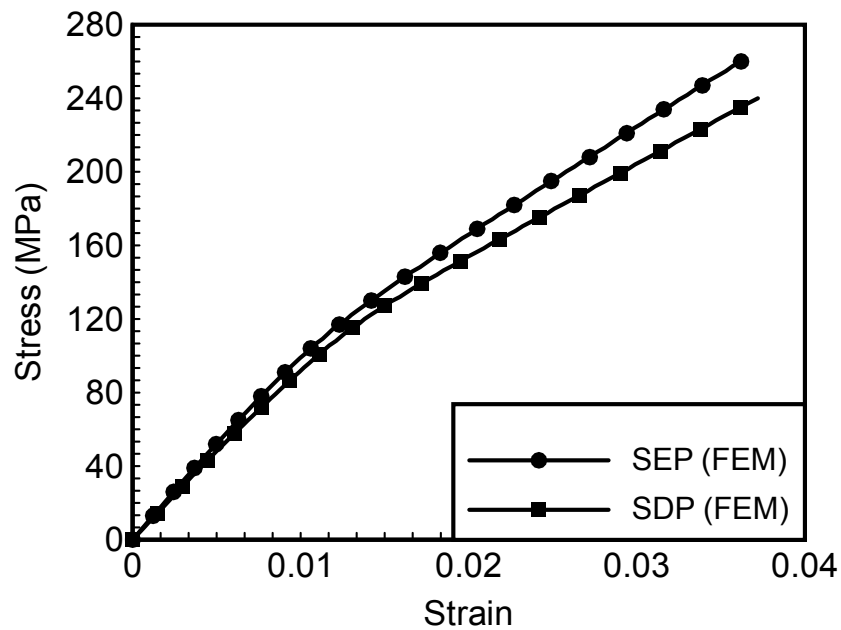
Fig. 6.10(c) The effect of fiber arrangements on the stress and strain curves of 45^0 fiber composites obtained from the FEM.
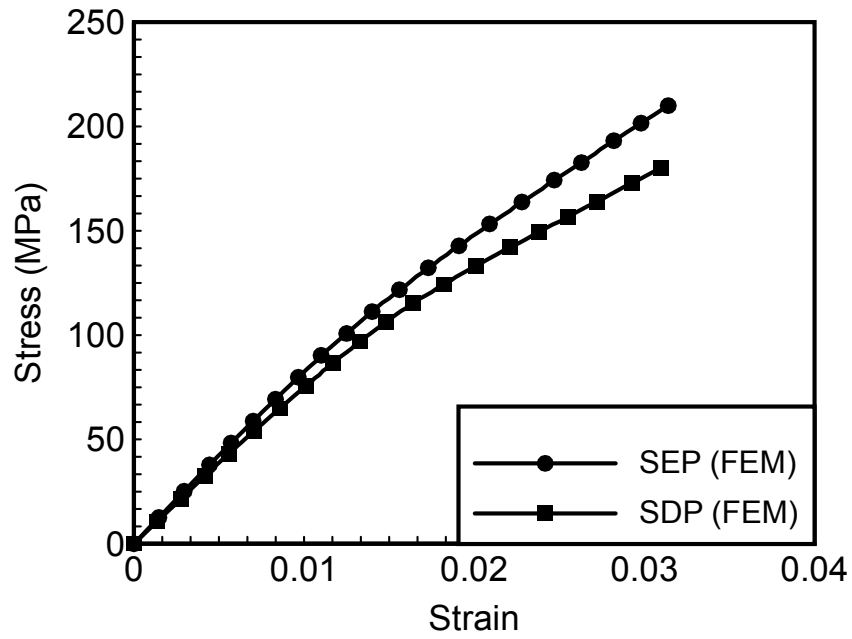
Fig. 6.10(d) The effect of fiber arrangements on the stress and strain curves of 60^0 fiber composites obtained from the FEM.
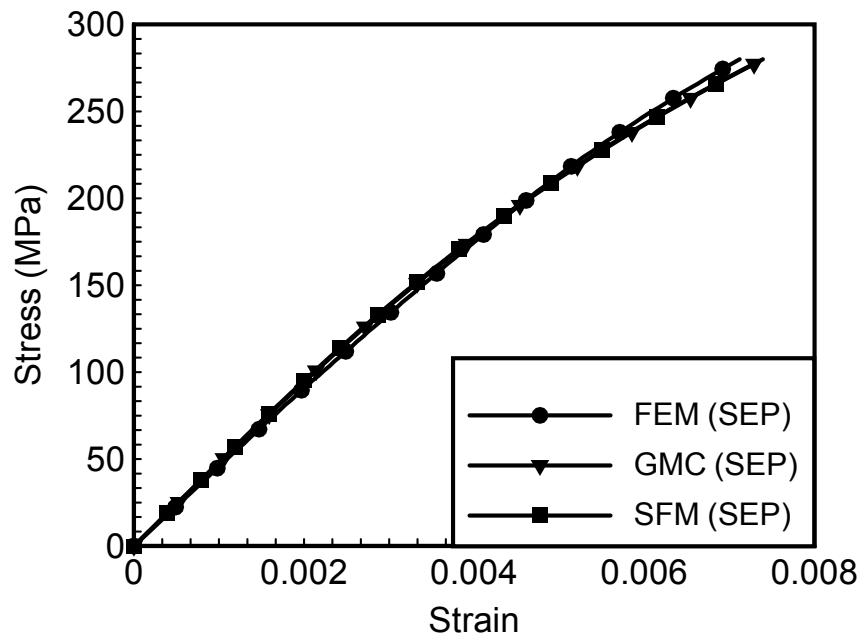
Fig. 6.11(a) Comparison of the stress and strain curves of 15^0 fiber composites with square edge packing array obtained from FEM, SFM and GMC.
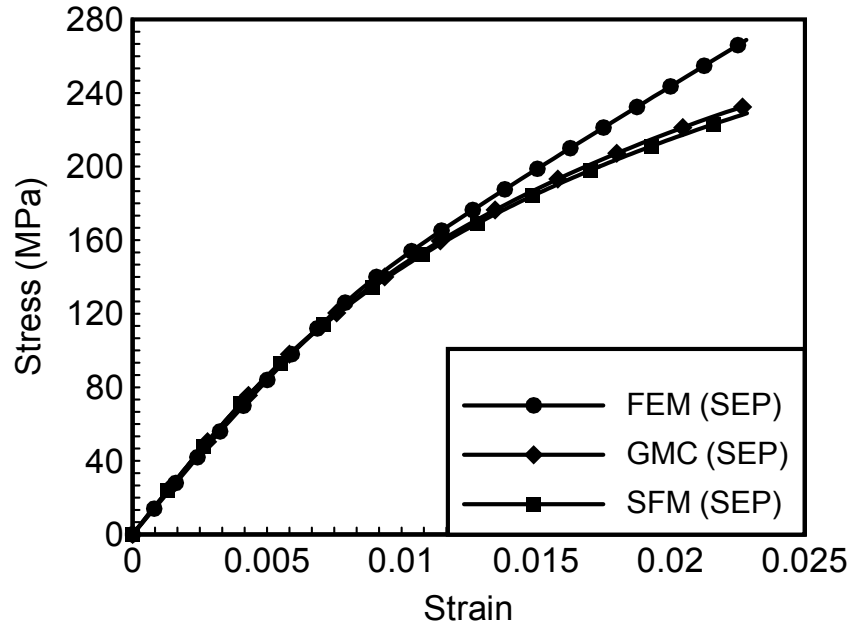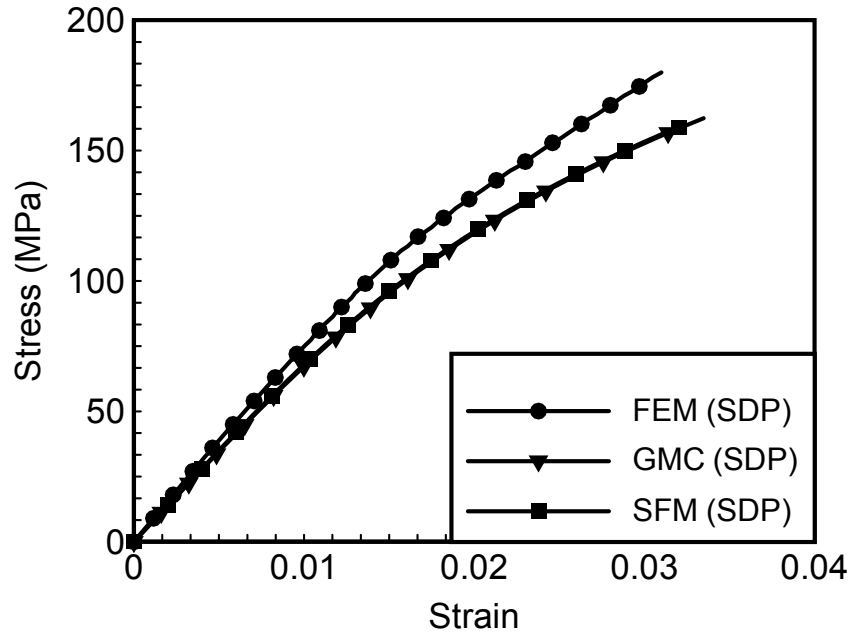
Fig. 6.11(b) Comparison of the stress and strain curves of 30^0 fiber composites with square edge packing array obtained from FEM, SFM and GMC.
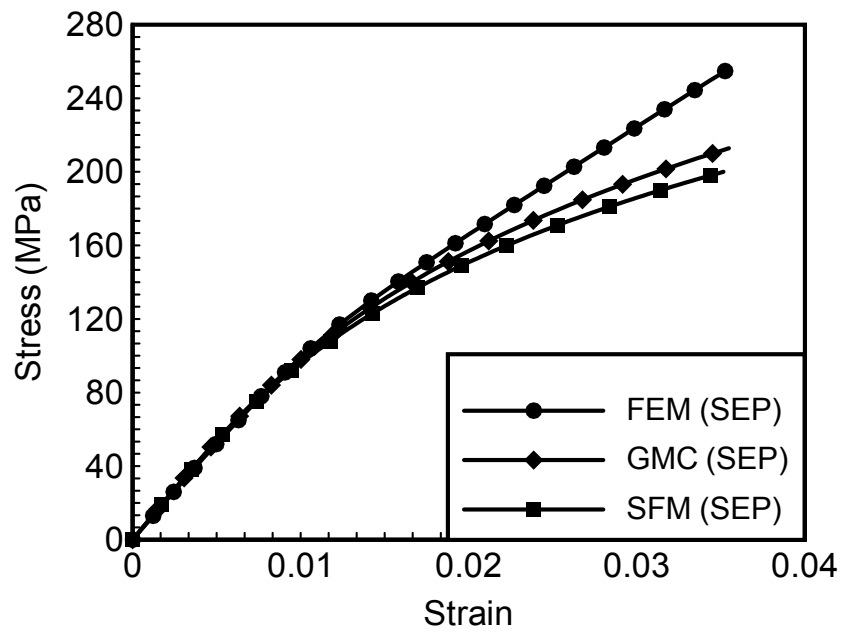

Fig. 6.11(c) Comparison of the stress and strain curves of 45^0 fiber composites with square edge packing array obtained from FEM, SFM and GMC.
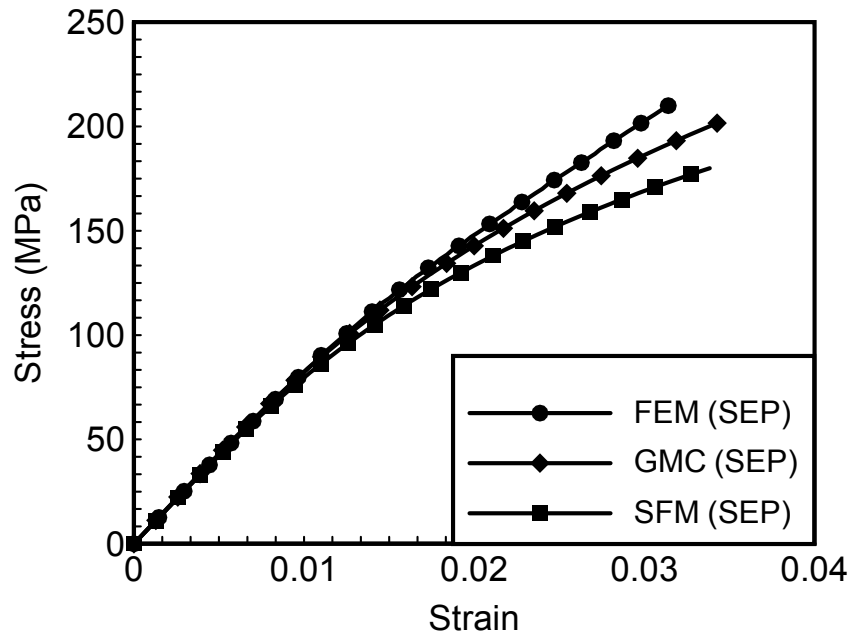
Fig. 6.11(d) Comparison of the stress and strain curves of 60^0 fiber composites with square edge packing array obtained from FEM, SFM and GMC.
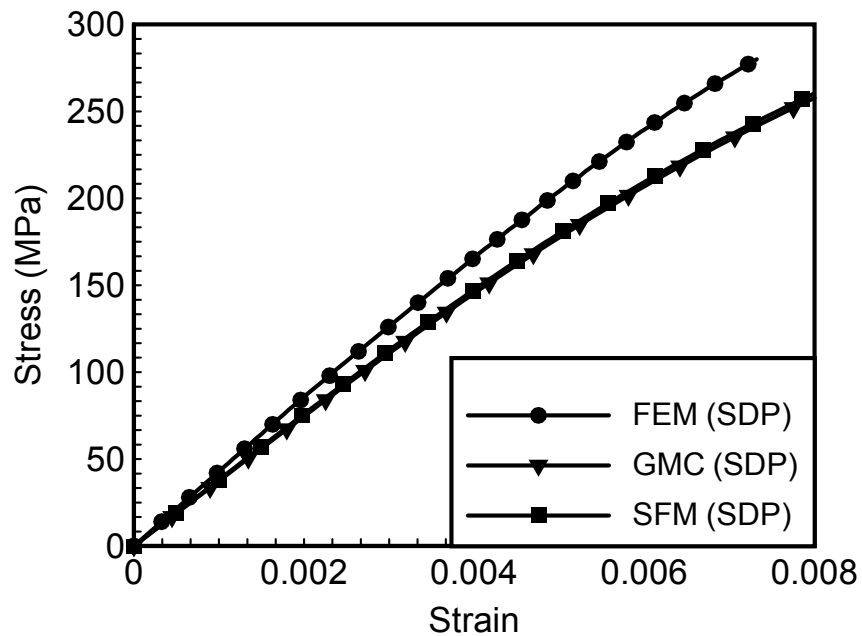
Fig. 6.11(e) Comparison of the stress and strain curves of 15^0 fiber composites with square diagonal packing array obtained from FEM, SFM and GMC.
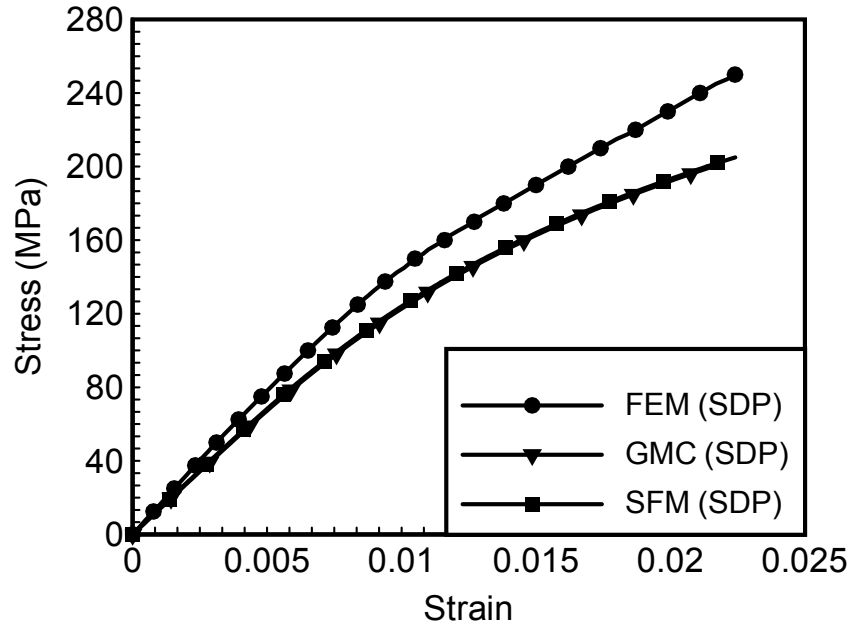
Fig. 6.11(f) Comparison of the stress and strain curves of 30^0 fiber composites with square diagonal packing array obtained from FEM, SFM and GMC.
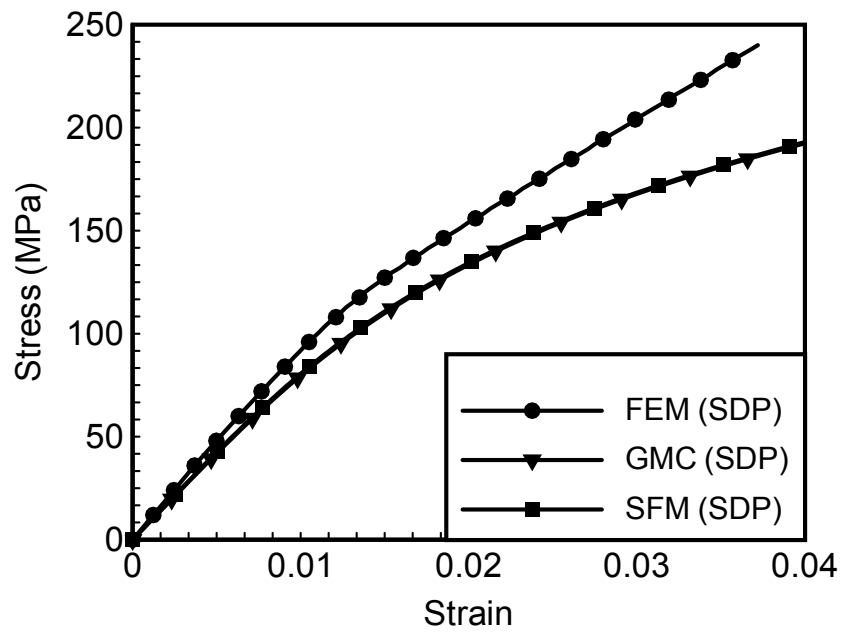
Fig. 6.11(g) Comparison of the stress and strain curves of 45^0 fiber composites with square diagonal packing array obtained from FEM, SFM and GMC.

Fig. 6.11(h) Comparison of the stress and strain curves of 60^0 fiber composites with square diagonal packing array obtained from FEM, SFM and GMC.
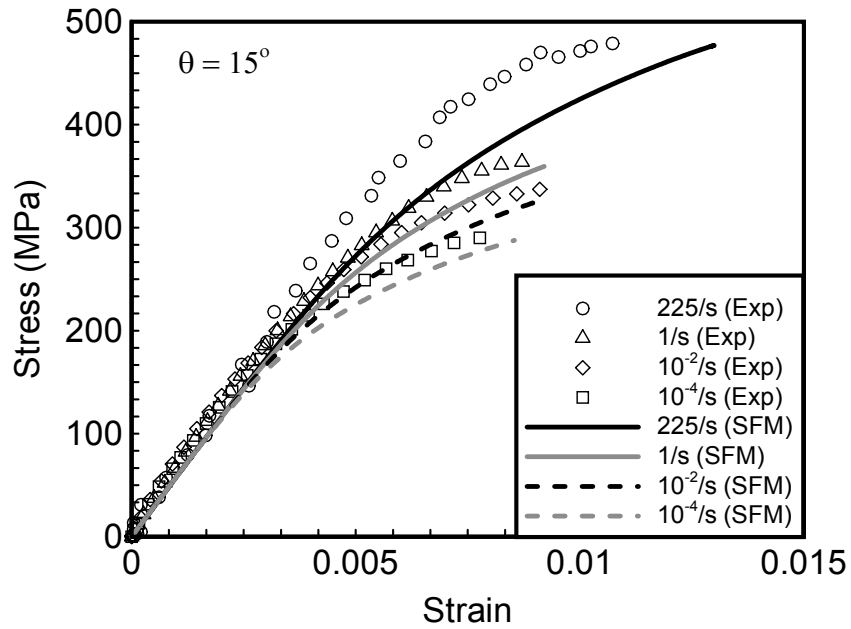
Fig. 6.12(a) Comparison of the experimental data with the model prediction obtained from SFM for 15^0 fiber composites.
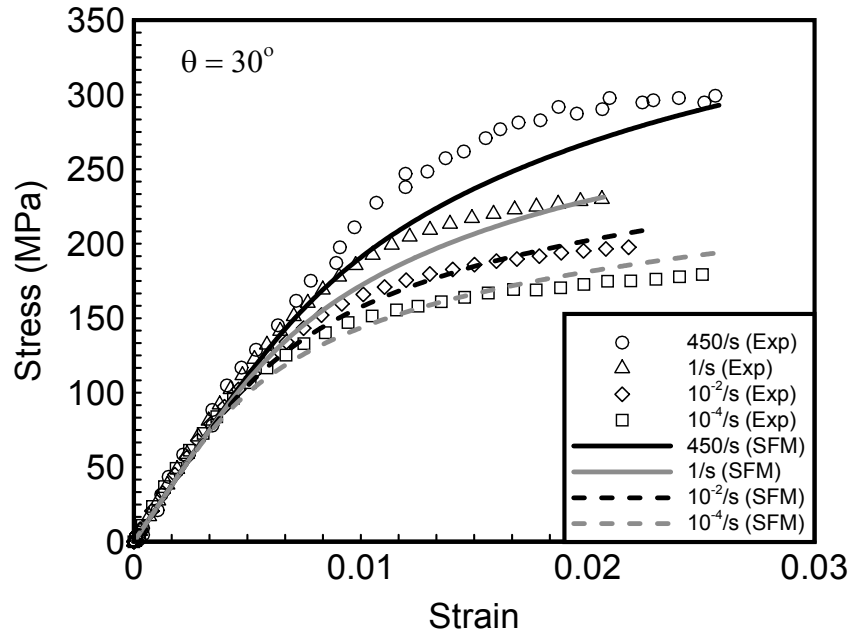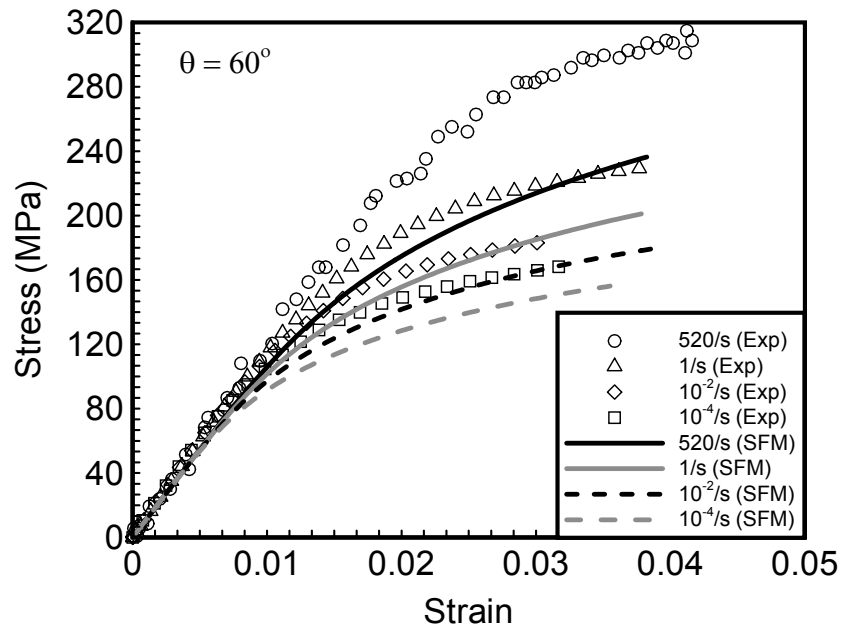
Fig. 6.12(b) Comparison of the experimental data with the model prediction obtained from SFM for 30^0 fiber composites.
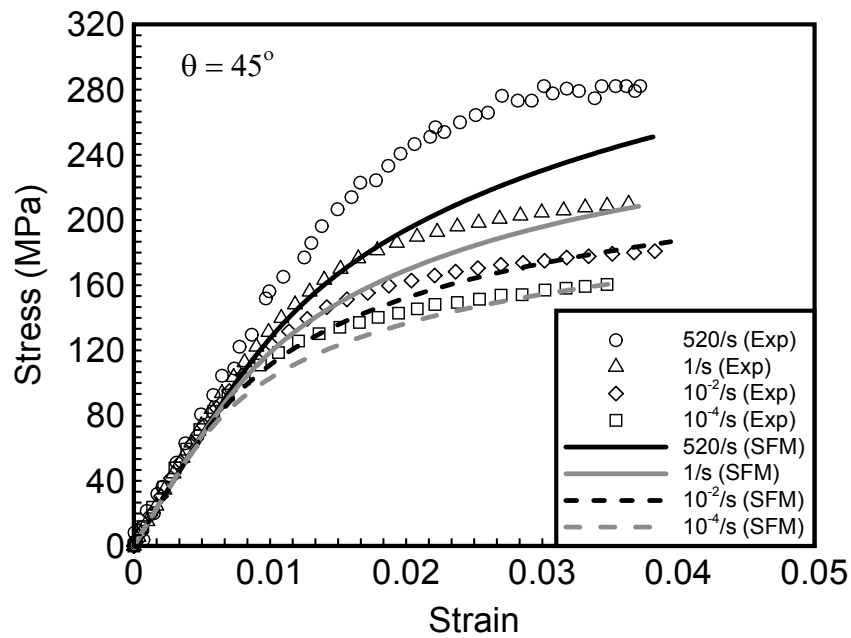
Fig. 6.12(c) Comparison of the experimental data with the model prediction obtained from SFM for 45^0 fiber composites.

Fig. 6.12(d) Comparison of the experimental data with the model prediction obtained from SFM for 60^0 fiber composites.
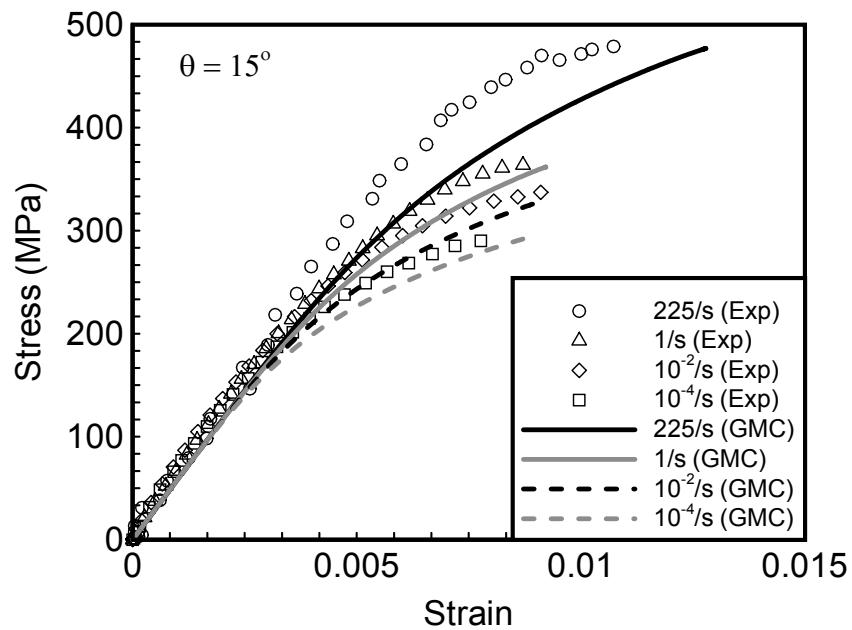

Fig. 6.13(a) Comparison of the experimental data with the model prediction obtained from GMC for 15^0 fiber composites.

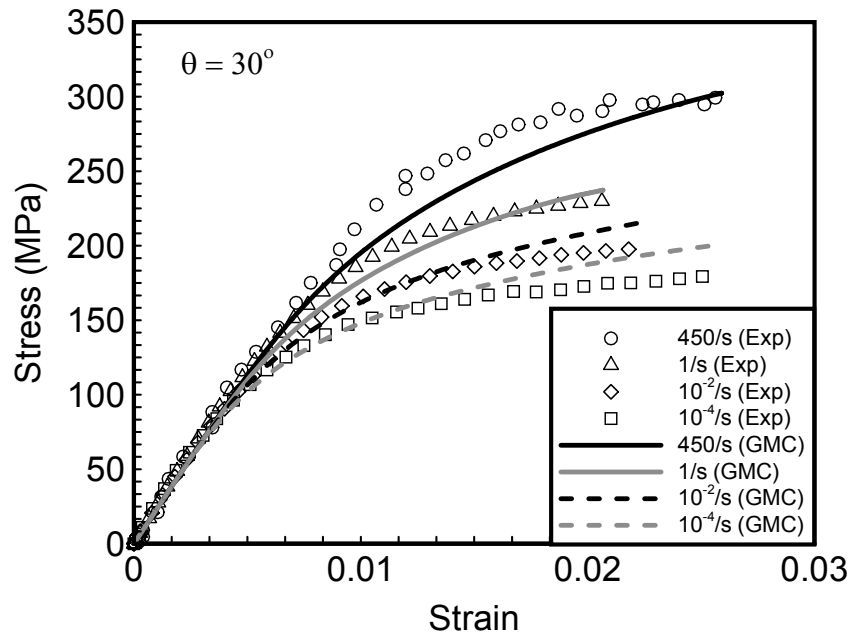Fig. 6.13(b) Comparison of the experimental data with the model prediction obtained from GMC for 30^0 fiber composites.

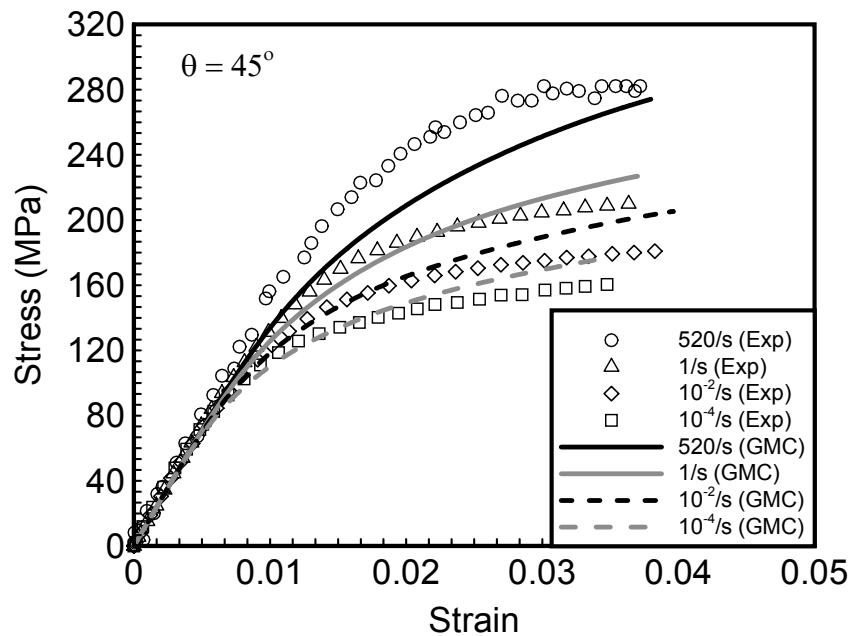Fig. 6.13(c) Comparison of the experimental data with the model prediction obtained from GMC for 45^0 fiber composites.
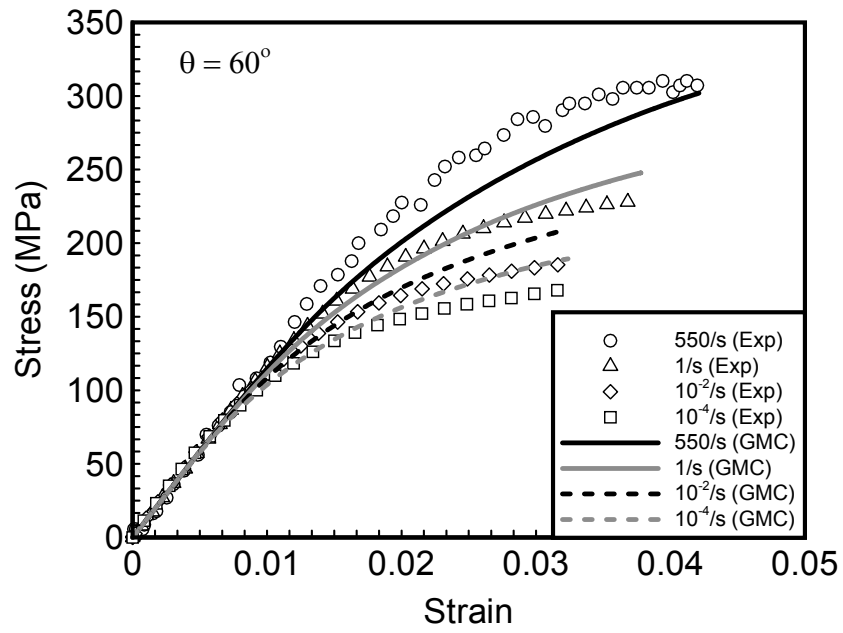
Fig. 6.13(d) Comparison of the experimental data with the model prediction obtained from GMC for 60^0 fiber composites.